The Influence of Secondary Processing Conditions on the Mechanical Properties and Microstructure of a Particle Reinforced Aluminium Metal Matrix Composite

Presented for examination for Ph.D. of the University of London 2008

by

Jonathan Richard Silk

BIBL. LONDON UNIV.

Abstract

The influence of secondary processing conditions on an aluminium metal matrix composite, comprising of an AA2124 matrix and 3 μm particulate SiC reinforcement at 25 volume percent was investigated. The metal matrix composite (MMC) was extruded at three different temperatures, 350°C, 450°C and 550°C, at a ratio of 20:1 and at three different ratios, 5:1, 10:1 and 20:1, at a temperature of 450°C. It was subsequently solution heat treated and naturally aged.

A mechanical property assessment was carried out using standard tensile and rotating bend fatigue test methods to determine the properties of the material extruded under each condition. A novel technique using a Focussed Ion Beam (FIB) Microscope was developed to prepare polished specimens and microtextural analysis was performed by FIB imaging. Additionally, techniques were successfully established, through the use of FIB milling and polishing, to provide site-specific electron transparent films, permitting detailed examination of the microstructure with a transmission electron microscope.

Material extruded at 550°C exhibited a lower yield strength than material extruded at 350°C and 450°C, which was attributed to grain coarsening and recrystallisation. Evidence of recrystallisation was found during texture analysis by X-Ray diffraction, where there was a reduction in the intensity of the <111> fibre texture in the extrusion direction. The phenomenon was also observed during microstructural analysis work, where recrystallised grains at grain boundaries were observed. Higher extrusion ratios offered a small improvement in tensile properties, due to an enhanced fibre texture within the microstructure. Microtextural examination gave evidence of the existence of both high angle grain and low angle grain boundaries for the material extruded at 350°C. It is believed that a subgrain structure was partially transformed during extrusion, through subgrain rotation, leading to the formation of high angle grain boundaries. This microstructure was found to offer the optimum mechanical properties.

Table of Contents

Abstract **2**

Acknowledgements **5**

1 Introduction **6**

2 Literature Review **11**

2.1 Strengthening Mechanisms 11

2.2 Microstructural Characterisation of Metal Matrix Composites 25

3 Experimental Methods **33**

3.1 Materials Studied 33

3.2 Extrusion 33

3.3 Heat Treatment 34

3.4 Tensile Testing 34

3.5 Rotating Bend Fatigue Testing 35

3.6 Specimen Preparation for Optical Microscopy 35

3.7 Grain Size Determination 35

3.8 Transmission Electron Microscopy – Conventional Sample Preparation 36

3.9 Focussed Ion Beam – Specimen Preparation and Imaging 38

3.10 Elevated Temperature Compression Testing 39

3.11 X-Ray Diffraction 40

4 Results and Discussion **41**

4.1 The Influence of Extrusion Temperature on Tensile Properties 41

4.2 The Influence of Extrusion Ratio on Tensile Properties 48

4.3 Fatigue Testing 51

4.4 Thermomechanical Compression Testing 54

4.5 The Influence of Thermomechanical Deformation on Strengthening Mechanisms 63

4.6 Microstructural Analysis of Aluminium MMC by FIB Imaging 81

4.7 Microtexture Analysis by Focussed Ion Beam Microscopy 89

4.8 Focussed Ion Beam Milling as a TEM Specimen Preparation Technique for an Aluminium Metal Matrix Composite 107

5 Conclusions 119

6 Further Work 122

7 References 124

Acknowledgements

The EPSRC for their financial support.

Lana, for your continued love and devotion and for supporting me in everything that I do. Judah, for the welcome distractions over the last six months and for putting everything into perspective.

Dad, Mum and Tim, for being a wonderful family and consistently encouraging me to do my best.

Lazarus, Maggie, Tanya, Katia and Yvette for being so much more than my "In-Laws."

Dr. Richard Dashwood, for encouraging me to start this work and helping me along the way with your enthusiasm and technical input. Prof. Harvey Flower for also setting me on this path and for all of those Friday afternoon sessions on the Transmission Electron Microscope! Mr. Richard Chater, for introducing me to the Focussed Ion Beam Microscope, which proved to be the most exciting area of this project. Also, for you enthusiasm for the research and your technical expertise.

Andrew, for not getting bored with me after one summer, for giving me this opportunity and for all of those "wacky ideas!" David, thank you for your support and continuous encouragement to get this finished. And to all of my colleagues at AMC, thank you for all of your help and input along the way.

Stavros and my fellow postgraduate students, was I the last to finish?!

Finally, to the Maker: thank you for the opportunity to take a closer look at your handiwork. Colossians 3:23-24.

1 Introduction

A Metal matrix composite (MMC) consists of a metal or alloy matrix combined with a ceramic reinforcement phase in fibre, whisker or particulate form. An MMC offers improved specific stiffness, strength, and fatigue performance across a wide temperature range compared to its monolithic counterpart. Typical matrix materials include aluminium, titanium, magnesium and steel. Reinforcements include silicon carbide, alumina, boron carbide and titanium diboride. Each combination offers its own unique blend of properties and by altering reinforcement content, performance can be further tailored to meet the requirements of a specific application.

MMCs can be manufactured by casting, powder metallurgy, in-situ development of the reinforcement phase and foil/fibre processing techniques. Each process offers a specific balance of cost versus performance. In general, cast MMCs can be manufactured in large quantities at relatively low prices. The main disadvantage of this route is a lack of consistent properties due to the propensity of the reinforcement phase to form clusters during solidification. Molten metal cannot infiltrate such regions, giving rise to microporosity and premature failure under an applied stress. For this reason, cast metal composites are not widely used in high performance automotive applications, where ductility and fracture toughness are often key requirements. Conversely, MMCs produced via a powder metallurgy route are comparatively expensive but offer superior mechanical properties and are often used in performance-driven applications. Through solid state processing it is possible to achieve a homogeneous dispersion of a reinforcement phase in a metal matrix. Such materials offer enhanced and consistent mechanical performance compared to cast MMCs.

Over the past thirty years a significant focus has been placed on the development of aluminium-based metal matrix composites. Aluminium alloys are an ideal candidate matrix material for MMCs as their low densities and strengths are suitably complemented by a high strength and high stiffness reinforcement phase. For example, through careful materials selection it is possible to produce an aluminium MMC with a fatigue performance comparable to that of a titanium alloy, resulting in a 35% density saving.

Aerospace Metal Composites Limited (AMC), based in Farnborough, UK, is a leading manufacturer of aluminium metal matrix composites. AMC manufacture in excess of thirty tonnes of aluminium MMCs annually through a powder metallurgy process route. The route comprises five principle steps, as illustrated in Figure 1.1, below.

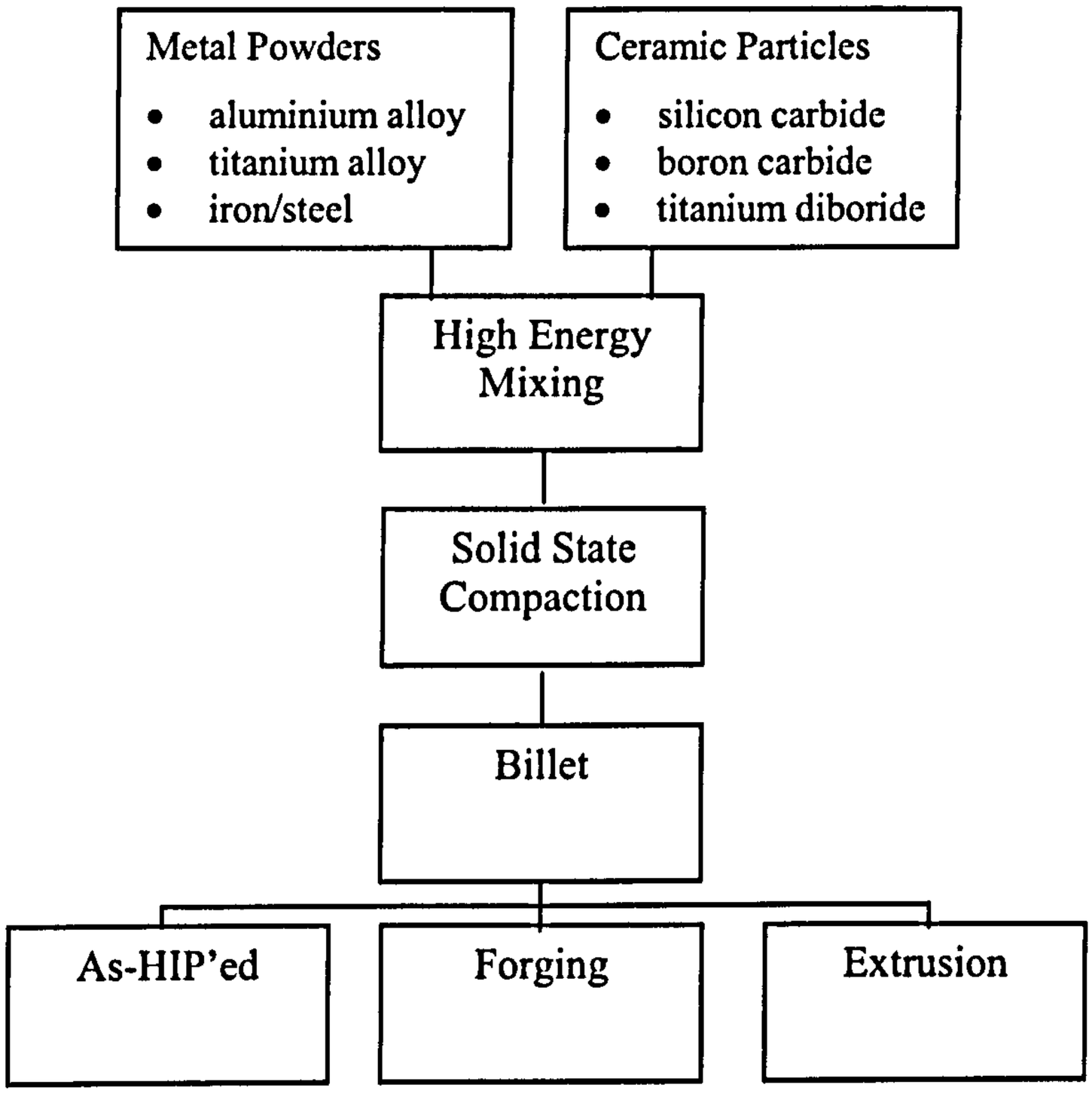


Figure 1.1 - AMC manufacturing process for MMCs

AMC's primary material is known as AMC225xe. This composite consists of an aerospace grade aluminium alloy matrix, AA2124, combined with 3 μm particulate silicon carbide at 25 volume percent. The gas atomised aluminium alloy powder is blended with the ultrafine SiC reinforcement in a proprietary high energy process known as mechanical alloying, which ensures a homogenous distribution of the reinforcement phase in the matrix. This process also imparts a significant amount of cold work to the material through cold welding and cold fracturing processes. The resultant powder is degassed and then consolidated by Hot Isostatic Pressing (HIP) into a one hundred percent theoretical density billet. This billet may then be fabricated in much the same way as a typical aluminium alloy by forging or extrusion processes. The composite can also be used in the as-HIP'ed condition.

The composite achieves typical proof stress levels of 450 MPa in the as-HIP'ed condition and up to 500 MPa in an extrusion product form. Elongation to failure ranges between 2% and 6% depending on product form and heat treatment. The composite is 50% stiffer than AA2124 and has double the fatigue performance from room temperature up to 350°C.

A fine grained and thermally stable microstructure gives rise to high ductility at secondary processing temperatures so the composite can be forged and extruded into complex shapes using conventional techniques at temperatures around 500°C (1) (2) (3) (4). Standard extrusion limit diagrams detailing extrusion temperatures and speeds are also available in the literature (1). It has also been reported that aluminium MMCs exhibit superplastic behaviour at elevated temperatures. Thermal soaking under an applied external load was found suitable for achieving composite superplasticity (5) (6) (7) (8) (9).

In recent years, aluminium MMCs have been developed for a wide variety of applications in a range of industries including aerospace, automotive, electronics, high speed machinery and sports equipment. Enhanced specific stiffness, tensile strength and high temperature fatigue strength make aluminium MMCs the material of choice over conventional aluminium and titanium alloys.

Aluminium MMCs are increasingly being used in applications where high performance and reliability are a key driving force, particularly in the aerospace industry. The importance of increasing the technical understanding of their behaviour and performance should not be underestimated. The application of traditional theories in order to predict the mechanical behaviour of MMCs is currently limited due to the increased complexity of the microstructure in these materials. A new approach to the understanding of such established topics as grain/sub-grain evolution during processing and microstructural evolution during heat treatment is essential in order to further refine and better control the mechanical properties of these materials.

The current work involves an investigation into the influence of secondary processing conditions on the microstructure and mechanical properties of AMC225xe. Five extrusion conditions were applied: three different extrusion temperatures (350°C, 450°C, 550°C) at a constant extrusion ratio (20:1) and three different extrusion ratios (5:1, 10:1,

20:1) at a constant extrusion temperature (450°C). This material was solution heat treated and cold water quenched to enable the precipitation of a metastable strengthening phase.

A series of mechanical tests was carried out on the material to study the influence of processing conditions on mechanical properties. These tests included tensile and compression testing, fatigue testing and hardness testing.

Microstructural characterisation was performed by applying a variety of techniques, both conventional and novel. In the first instance, macrostructures were analysed through optical microscopy, using conventional specimen preparation techniques. More detailed analysis was conducted through the development of contemporary techniques including focussed ion beam (FIB) microscopy and transmission electron microscopy (TEM).

Imaging the microstructural evolution in a metal matrix composite using conventional techniques is difficult due to artefacts arising from traditional metallographic sample preparation techniques (10). Additionally, the refined nature of the grain structure of a particulate reinforced MMC means that high resolutions are necessary in order to observe even basic metallographic features, such as grain structures. Optical microscopy permits the observation of the reinforcement phase but does not allow for grain structure analysis. Scanning electron microscopy (SEM) reveals details such as the presence of intermetallic particles but likewise, cannot provide grain structure information, even through electron backscattered detection (EBSD) techniques due to resolution limitations. TEM does provide the opportunity for detailed microstructural characterisation but with the usual limitations of specimen preparation difficulties and minimal area selection.

Over the past five years FIB analysis has been demonstrated as a useful tool in the specimen preparation of MMCs but extensive microstructural characterisation using this technique has not previously been conducted. Traditionally, the most common usage for FIB microscopy has been in the semiconductor industry. Defect analysis and circuit modification as well as site-specific TEM specimen preparation have become standard procedures (11) (12) (13). Recently, FIB techniques have been applied to metallic materials, in particular for site-specific TEM sample preparation (14). The current study

aims to develop the FIB technique for sample preparation and imaging into a routine procedure for the characterisation of MMCs.

The focussed ion beam microscope works by directing a beam of positively charged gallium ions at a sample surface, causing a sputtering effect. At high primary ion beam currents, high sputtering rates mean that material can be quickly removed allowing precision milling of surfaces down to a sub-micrometer scale. At low ion beam currents, very little material is sputtered and imaging can be achieved by collecting secondary electrons or secondary ions, to a resolution of 4 nm. By utilising a range of contrast techniques it is possible to study the fine microstructural detail of an MMC that cannot normally be observed by optical microscopy or in a conventional SEM.

During the course of this study, the process of FIB milling, polishing and imaging has been developed and has been shown to provide a fresh insight into the microstructure of an aluminium metal matrix composite.

The thesis will include a section describing much of the previous work that has been undertaken on AMC225xe and similar materials, relating to processing conditions, heat treatment, mechanical properties and microstructural characterisation. The experimental methods go on to describe in detail the wide range of experimental techniques that were involved during the work. Additionally, an in-depth account of the development of the FIB process for the preparation and imaging of aluminium MMCs is outlined. The experimental data is presented, followed by a detailed analysis and interpretation of the results, including the correlation of mechanical property data to the microstructural appearance of the material. The main findings of the work are summarised and their relevance and application to the current manufacturing process for PM MMCs are highlighted.

2 Literature Review

2.1 Strengthening Mechanisms

In order to investigate the influence of secondary processing conditions on the mechanical properties of a metal matrix composite, it is first necessary to gain an understanding of the various strengthening mechanisms that are involved in composite systems and their relative contribution to the overall properties of the material. Also, a knowledge of which strengthening mechanisms are modified during processing is required to enable a refinement of the processing conditions, thus enhancing the mechanical properties of the material.

Primary particulate composite strengthening mechanisms include (15):

- Load transfer to reinforcement
- Grain/subgrain structure and texture
- Dislocation density
- Strengthening precipitates in matrix

Load Transfer to Reinforcement

Interfacial bonding between the matrix and reinforcement is critical for substantial strengthening through load transfer. If the bond is weak, the interface will fail and no effective stress transfer to the particle can occur.

A strong matrix/reinforcement interface is also essential to encourage dislocation generation (16). Reaction products at the interface can weaken age-hardened matrices by removing alloying elements from solid solution, thus reducing the amount available for precipitation reactions (17).

If an external load is applied to a composite, the proportion of the load carried by each constituent phase can be predicted by volume-averaging the load within them. Hence, the condition governing the volume-averaged matrix and reinforcement stresses can be expressed as follows:

$$(1-f)\bar{\sigma}_M + f\bar{\sigma}_I = \sigma_A$$

Equation 2.1

where: $\bar{\sigma}_M$ – volume-averaged matrix stress

$\bar{\sigma}_I$ – volume-averaged reinforcement stress

σ_A – applied external stress

f – volume fraction of reinforcement

During the reduction of the cross-section of a composite billet in the extrusion die, the metal matrix is deformed in a plastic manner. In contrast, the hard and brittle ceramic particles, because they are rigid and non-deformable, tend to fragment with the softer matrix being forced into the voids created by the fracture event (18) (19). A particle fractures when the local stress acting on it exceeds its fracture strength (20) (21). Evans and Boyd postulated that the cracking of SiC particles in an aluminium matrix was not only due to the applied stress during deformation of the matrix, but also occurred as a result of the residual microstresses present in the SiC particles (10). They suggested that the difference in the coefficient of thermal expansion (CTE) between the reinforcement and matrix induces significant stresses in the SiC particles, which, when combined with the applied stress, is likely sufficient to permit the formation of pure dislocations in the SiC. This was confirmed by the fact that prior to deformation, stacking faults were visible in the SiC particles, but they were no longer present after a plastic strain of 0.7% had been applied. Following the formation of perfect dislocations, microcracks are likely to form at points of high localised stresses within the particles, such as angular sections, leading to premature failure and hence, low ductility.

Evans and Boyd conducted a detailed study on the evolution of the near-interface microstructure in a SiC/Al composite during tensile deformation, following extrusion at 500°C and solution heat treatment (10). The material investigated was AA2080, reinforced with 20 vol% SiC_p. The mean diameter of the SiC was 3.3 ±0.5 μm. Billet was produced through a powder metallurgy (PM) route, involving mixing, cold compaction, and hot extrusion. The material was subsequently heat treated at 510°C for two hours and cold water quenched. The process is similar to that which is employed in the production of AMC225xe; hence this study is of particular relevance to the current work. The main difference between process routes is the omission of a mechanical alloying stage in the Evans study, which could have a negative impact on the coherence of the matrix/reinforcement interface and lead to clustering of SiC particles, as compared to the AMC225xe manufacturing route.

Following heat treatment, samples were deformed using a tensile testing machine, to various strains, up to fracture. After deformation, samples were artificially aged at 177°C for 24 hours to decorate the matrix dislocations with precipitates. A combination of TEM and focussed ion beam (FIB) microscopy was used to monitor the evolution of the near-interface region.

The microstructure revealed the presence of an interface layer, which was 20 nm - 40 nm thick. This type of interface layer is not seen in cast composites as the natural layer of SiO_2 on SiC particles is normally consumed by a reaction with molten aluminium. The layer on the PM composite was found to be amorphous and rich in Si, Mg, Al and O. In specimens that had undergone a greater degree of strain there was evidence of particle-matrix decohesion. In all cases decohesion occurred through fracture of the interfacial layer. It was suggested that the thickness of the interfacial layer increased during extrusion by interdiffusion with the Al_2O_3 surface layer on the aluminium powder (10). Beyond a critical strain level of approximately 0.7%, some of the SiC particles were found to contain microcracks. This behaviour had not been previously reported for AMC225xe, but it will provide the basis for further investigation.

An additional consideration for the strengthening of composites during processing is the control of porosity and other defects. The elastic modulus of an MMC has been found to decrease with the presence of microcracks and porosity (22).

Low ductility in a highly reinforced composite is unavoidable due to high porosity content and early void formation at low strains. However, processing techniques, such as forging and extrusion, improve the ductility of the composite by decreasing the porosity content, improving the particle-matrix bond and refining the matrix structure.

Grain/Subgrain Structure and Texture

Recrystallisation and grain growth have a significant influence on microstructural evolution of conventional alloys and composites during processing. In general, recrystallisation occurs at a lower temperature in a composite than in an unreinforced alloy and gives a finer recrystallised grain structure. The main nucleation sites for recrystallisation are grain boundaries and constituent particles, including the reinforcement phase (23). The fine grain structure in particulate composites is characterised by grains ranging in size from 500 nm – 2000 nm (17) (24) (25). The

presence of a reinforcement phase and oxides from the initial powder surfaces restrains the migration of grain boundaries and therefore restricts significant grain growth under normal processing and heat treatment conditions, so a fine-grained structure is retained (26) (27). This is also an advantage for elevated temperature applications where, again, the fine subgrain structure is generally retained, as recrystallisation is suppressed by the presence of pinning phases (28). Therefore, the propensity towards lower temperature recrystallisation due to the significant levels of cold work in the matrix is offset by the inhibiting effect of the pinning phases.

It is considered that Hall-Petch strengthening and forest hardening are two of the most important interactions with regards to composite strengthening. The Hall-Petch equation predicts (29):

$$\sigma_y = \sigma_0 + kD^{-\frac{1}{2}}$$

Equation 2.2

where:

σ_y – tensile yield stress

σ_0 – yield stress of singles crystal of similar composition and dislocation density

k – locking parameter (material constant)

D – slip distance

The slip distance, D, is not necessarily defined as grain/subgrain size and if the reinforcement/inter-particle separation is smaller, this is the slip distance used in the Hall-Petch relationship. The advantage of an MMC is that in general, the grain diameter, D, does not increase significantly, even at elevated temperatures, meaning the yield strength is not compromised during processing and heat treatment operations.

During deformation of a composite, the degree to which grain rotation occurs is hindered by neighbouring grains exerting a mutual constraint on each other (30). This gives rise to the formation of crystal textures, which may have implications on the mechanical properties of the material. The presence of reinforcement particles permits the relaxation of surrounding dislocations that were generated during deformation. This gives rise to local rotations, which are not necessarily related to the general orientation

within the matrix (31) (32). The net effect is a reduction in the 'deformative texture' due to the presence of a particulate reinforcement phase (30).

A study was carried out to determine the influence of extrusion temperature on the microstructure and texture of AA6061-15vol% SiC_w (33). It showed that although the two main texture components, <111> and <100>, were present for all extrusion conditions, the relative volume fraction of crystallites, F_v, for each, increased with increasing processing temperature. This was associated with a more 'banded' structure observed using optical microscopy of longitudinal specimens. It was suggested that particle stimulated nucleation of recrystallisation (PSN), at the matrix/reinforcement interface, was responsible for the randomisation of texture in the matrix grains. The PSN phenomenon was more evident in material extruded at lower temperatures and hence, F_v <111> and F_v <100> were reduced under such conditions.

Due to the highly refined grain structure found in particulate reinforced MMCs at volume fractions exceeding 17%, the hot deformation characteristics of such materials are equivalent, if not superior to those of their monolithic counterparts. It is believed that the grain structure of particulate reinforced MMCs is highly stable, even during exposure to temperatures close to the melting point (30). At similar temperatures, conventional alloys would show rapid grain coarsening, reducing the total grain boundary area within the material. For aluminium alloys, hot deformation is dependent on grain boundary sliding. Due to the stability of the grain structure in the MMC, the total grain boundary area is greater than that of the monolithic alloy so the hot deformation mechanism will proceed more readily at lower stresses.

It has been shown experimentally that for an MMC consisting of an AA2124 matrix reinforced with 25 volume percent silicon carbide particulate, the compressive flow stress becomes lower than that of the unreinforced alloy at temperatures exceeding approximately 400°C (34).

Additionally, MMCs may even show signs of superplastic behaviour at elevated temperatures. Thermal cycling carried out under an applied external load has been shown to cause an MMC to exhibit superplasticity (35) (36). In such processes, deformation is controlled by grain boundary sliding and it has been suggested that melting at grain boundaries may play a part (26) (37). High strain-rate sensitivity is

also a characteristic of superplastic materials (19). The equation below shows the relationship between stress and strain rate, with reference to the work hardening exponent and strain rate sensitivity.

$$\sigma = k\dot{\varepsilon}^n \varepsilon^m$$

Equation 2.3

σ – applied stress

$\dot{\varepsilon}$ – strain rate

n – work hardening exponent

m – strain rate sensitivity index

For the majority of metals: - at low homologous temperatures, $m \sim 0.1$ to 0.3
- at high homologous temperatures, m tends to zero

However, for some alloys and composites, a very refined (i.e. 1 μm to 10 μm) and stable grain structure means that the value of m can rise to between 0.5 and 0.8 at high homologous temperatures. This permits very large elongations (100% to 1000%) under a tensile load at typical strain rates of 10^{-3} s^{-1} to 10^{-4} s^{-1}, under very low stress. It is believed that this phenomenon could occur in an AA2124/SiC_p composite due to its fine-grained (<2 μm) and stable microstructure.

The process of hot extrusion applied to MMCs is commonly used by manufacturers to fabricate bars or more complex shapes. For aluminium MMCs, this process is typically carried out at temperatures around 500°C (1). Extrusion limit diagrams are available in the literature (33).

With respect to hot forging, the process can be more problematic. In open die forging where unconstrained edges experience high tensile strains, surface tearing can occur through reinforcement particle fracture or limited plastic ductility, if the processing temperatures are not carefully controlled.

In studies of the open die forging of an aluminium MMC reinforced with 26 volume % silicon carbide, it was concluded that the hot deformation of MMCs frequently causes microstructural defects, including voids and cracks, which contribute to an overall

reduction in ductility (38). Additionally, it has been theoretically established that ceramic particle fracture and resultant void formation became the predominant failure mechanism at higher strain rates and lower processing temperatures (39). As for conventional aluminium alloys, as strain rate increases and processing temperature decreases, the flow stress required during the forging process increases. Aluminium matrices designed for plastic deformation show superior forgability compared to Al-Si matrices (40).

Particle reinforcement size, volume fraction of reinforcement and strength of particle/matrix bond have also been shown to influence the forgability of MMCs (9).

Dislocation Density

Studies using a Transmission Electron Microscope (TEM) have shown that significant dislocation generation occurs around reinforcement particles during quenching (41) (42). In SiC reinforced aluminium matrix composites, the coefficient of thermal expansion of the aluminium alloy matrix is approximately ten times larger than that of SiC, so on quenching, large plastic strains are developed in the matrix, around the particles, and a tensile residual stress is left in the matrix after it yields (43). This is accompanied by a compressive stress in the reinforcement (44). Dislocation punching occurs as the matrix yields, so reducing the tensile residual stress (45). The Eshelby model predicts that for particulate reinforcements (with aspect ratio ~ 1), the whole matrix will be covered with dislocation punches, leading to a large increase in strength (46). Thomas and King demonstrated that the overall density of dislocations generated during quenching is dependent on the temperature change during quenching (ΔT), up to a maximum limit (27).

During quenching, dislocations are punched outwards from the reinforcement/matrix interface, but during subsequent heat treatment, they return to the interface (47). Dislocations tend to initiate from sharp corners of the reinforcement particles, which act as stress-raisers (42). It has been demonstrated that during hot deformation, dislocation sinks at subgrain boundaries offer a reduction in the overall dislocation density and provide an increase in the ductility of the composite.

Strengthening Precipitates in Matrix

As for conventional 2xxx series aluminium alloys, the secondary processing stage for AMC225xe MMC is usually followed by a heat treatment step, during which the copper and magnesium alloying elements dissolve into the aluminium in the form of a solid solution. Following quenching, precipitation occurs during a subsequent ageing process to form fine metastable strengthening phases. In Al-Cu alloys the thermodynamically stable product of the ageing sequence is the θ-phase ($CuAl_2$). However, in Al-Cu alloys, which also contain Mg (such as AA2124), large S-phase ($CuMgAl_2$) intermetallics also form within grains and at grain boundaries (17). AA2124 also contains Mn, which acts as a grain refiner by forming small intermetallic particles with the composition $Al_{20}Cu_2Mn_3$. These particles are not removed during homogenisation (48).

It has also been show that the rate of quenching during heat treatment has a significant impact on the overall strength of an aluminium MMC. Thomas and King reported that SiC reinforced AA2124 showed an increase in quench sensitivity over the monolithic alloy at high cooling rates. Under low cooling rates, the reverse was true (49).

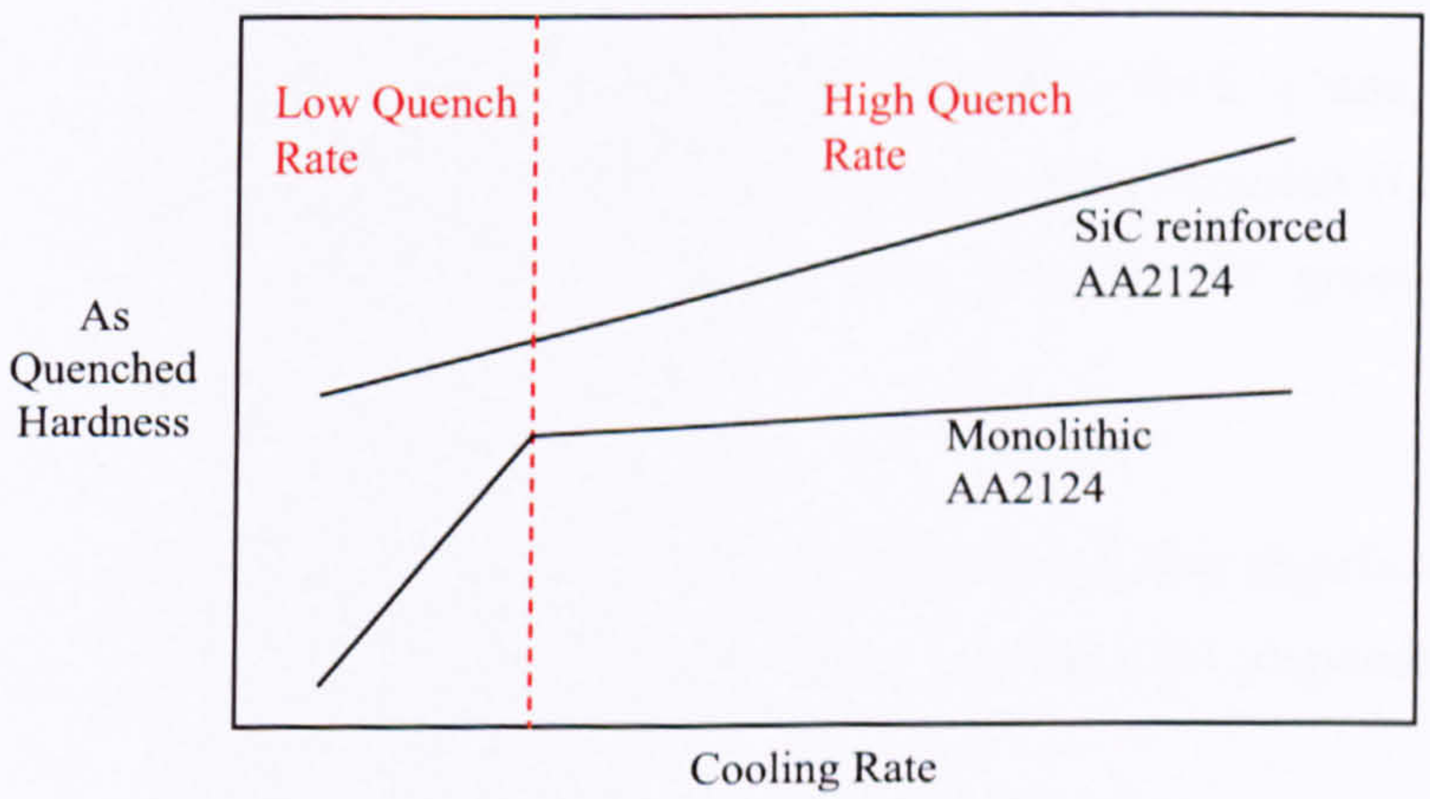


Figure 2.1 - Quench sensitivity of AA2124/SiC_p, adapted from Thomas et al. (49)

For several aluminium matrix composites, the enthalpy of formation of Guinier-Preston (GP) zones detected by Differential Scanning Calorimetry (DSC) analysis is affected by altering the quench rate. A study of AA2124 showed that a powder production route and the inclusion of SiC reinforcement particles led to a large reduction in GP zone formation when the quench rate was reduced (50). This decrease was far less severe in conventionally produced, reinforced material. Under air-cooling, the composite showed no signs of GP zone precipitation or dissolution. Another study showed that GP zone

precipitation and dissolution peaks were lost on slow cooling (29). This was attributed to a low concentration of quenched in vacancies, which are important for GP zone formation. Rapid quenching gave a GP zone precipitation peak because a larger number of vacancies were retained, thus facilitating GP zone formation. In composite materials, the vacancy concentration is reduced because the increased numbers of dislocations act as sites for annihilation of vacancies (49).

The generally accepted precipitation sequence in age-hardened aluminium alloys is as follows:

GP zone formation → GP zone dissolution → metastable precipitate formation → partial transformation to thermodynamically stable form → dissolution of metastable and stable precipitates

The specific precipitation sequence for an Al-Cu alloy is:

GP I zones → GP II zones (or θ'') → θ' → θ (51)

In Al-Cu-Mg alloys, the main age-hardening precipitate is the S' phase, which forms as rods or laths. The morphology is affected by the net solute content (i.e. Cu + Mg). A high net concentration of solute (i.e. >4%), such as for AA2124, gives laths parallel to {210} planes (52).

The ratio of copper to magnesium in an Al-Cu-Mg alloy is also significant. The ratio of copper to magnesium in AA2124 can range from 4.1:1 to 2.1:1, depending on the exact composition, as shown in Figure 2.2.

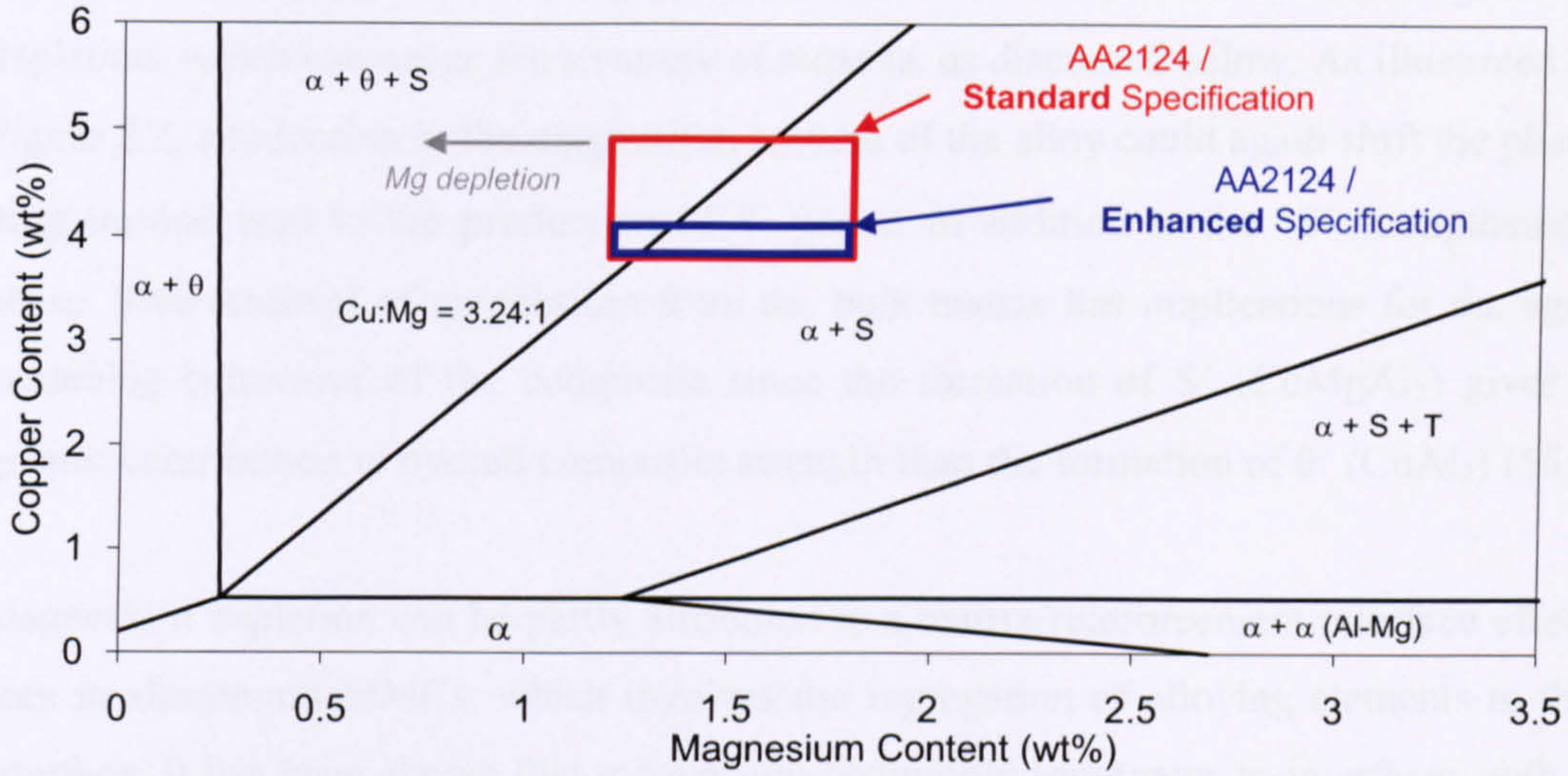


Figure 2.2 - Al-Cu-Mg Phase diagram at 190°C, adapted from Dyos (53)

At a ratio of 7:1, the alloy ages like a mixture of Al-Cu and pseudo-binary Al-S, i.e. forms both θ' and S'. At 2.2:1, the alloy is pseudo-binary Al-S (54). Differential Scanning Calorimetry (DSC) analysis of the precipitation reactions in 2014 (Cu:Mg = 7:1), showed three exotherms corresponding to the formation of GP zones, S' and θ' (55). Analysis of a range of Al-Cu-Mg alloys showed the two formation reactions, S' and θ', as a doublet exotherm between 200°C and 300°C. Increasing the relative amount of Mg in the alloy, to ensure the formation of only S', removed the first peak of the exotherm, indicating that the first peak can be attributed to θ', whilst the second is likely to be due to S' formation (38). For AA2124, DSC showed peaks corresponding to GP zone formation and dissolution and S' precipitation and dissolution; no θ' precipitation was observed for this alloy (50).

In order to increase the likelihood of forming only S' phase strengthening precipitates the tolerance on the copper content of the aluminium powder used in the production of AMC225xe is tighter than that of conventional AA2124. This is illustrated in Figure 2.2. Limiting the copper content to a maximum of 4.2 wt% (rather than 4.9 wt%) reduces the chances of forming θ' precipitates and therefore offers a noticeable strength advantage to the MMC. It also increases the likelihood of dissolving all of the copper into solution during heat treatment and thus reduces the occurrence of coarse intermetallics, which could have a detrimental effect on the ductility of the material.

Another consideration for the composition of the matrix alloy is the issue of magnesium depletion, which can occur for a variety of reasons, as discussed below. As illustrated in Figure 2.2, a reduction in the magnesium content of the alloy could again shift the phase diagram and lead to the production of θ' phase, in addition to the S' strengthening phase. This removal of magnesium from the bulk matrix has implications for the age-hardening behaviour of the composite since the formation of S' ($CuMgAl_2$) gives a greater contribution to overall composite strength than the formation of θ' ($CuAl_2$) (56).

Magnesium depletion can be partly attributed to a matrix/reinforcement interface effect seen in aluminium MMCs, which involves the segregation of alloying elements to the interface. It has been shown that magnesium commonly segregates to interfaces with a variety of reinforcements (17) (57) (58).

Additionally, Vermaut found that in spray formed Al-Cu-Mn-Mg composites, reinforced with SiC, no ageing precipitate containing magnesium was formed, even though S' was predicted to be the main ageing precipitate (59). It has been suggested that Si from reinforcement particles reacts with Mg in the matrix to form Mg_2Si, thus reducing the amount of Mg available for S' precipitation (60), contributing to the Mg depletion effect mentioned previously.

Vacancies and dislocations control the ageing behaviour when either S' or θ' are formed, since they alter the rates of diffusion and nucleation within the microstructure (61). The addition of other alloying elements can affect the age hardening response by changing vacancy concentration and providing alternative nucleation sites for precipitates (62). Quenched in dislocations in composite materials can act as vacancy sinks (63). The matrix/reinforcement interface has also been cited as a possible location for vacancy annihilation (64) (65). GP zone formation is very sensitive to vacancy formation, so a lack of vacancies can be a hindrance or entirely eliminate GP zone formation.

Frequently, there is a reduction in the enthalpy of formation of precipitation reactions in aluminium composites and GP zone precipitation is particularly affected. It has been suggested that this could be attributed to the high dislocation density in such materials, following quenching (50).

During quenching, the SiC cools more slowly than the matrix so the matrix at the interface is warmer than the bulk. This means that it has a raised concentration of both copper atoms and vacancies (higher solid solubility), in addition to a residual stress, which encourages vacancy formation. The net effect is enhanced GP zone precipitation, thus giving a lower peak temperature for the reaction. In addition, vacancy annihilation in the bulk gives a reduction in the total precipitation throughout the matrix, hence a lower enthalpy (49).

Two main effects have been noted when investigating the age hardening behaviour of MMCs. Firstly, the magnitude of the hardness increase during ageing is often less pronounced than that of the unreinforced alloy. Secondly, the kinetics (and hence, the time taken to reach peak hardness) of age hardening are altered.

The age hardening effect may be reduced by:

(i) Chemical effects including segregation of solute giving an inhomogeneous distribution of secondary phase particles, such as oxides, spinels and intermetallics at the matrix/reinforcement interface
(ii) Reactions at the matrix/reinforcement interface (66)

Hunt observed that AA2124 reinforced with SiC underwent an unconventional ageing curve under both natural and artificial conditions. Rather than climbing to a plateau and then slowly decreasing, the hardness started at a maximum value and then decreased steadily with ageing time (67). This decrease in hardness was attributed to the effect of the lattice strain developed during the quench. It was suggested that this increased the effect of solute strengthening from copper. During ageing, this strain was relaxed, causing a continuous decrease in hardness. Thomas attributed a similar drop in hardness to dissolution of GP zones formed during quenching (49).

The ageing sequence for an Al-Cu-Mg alloy is more complex than that of an Al-Cu alloy. Although GP zone formation is followed by an intermediate precursor to the stable S phase, they are not generally thought to have an equivalent stage to GP II zones, or θ''. Also, S' does not transform directly from GP zones, but rather nucleates on dislocations within the microstructure (64) (67). It then transforms to the incoherent

S phase at approximately 450°C, having a similar crystal structure with a slightly different lattice parameter (54).

Due to the heterogeneous nature of S' nucleation on dislocations, the formation of the strengthening phase is highly dependent upon the dislocation density of a material. Some studies have suggested that when an AA2124/SiC_p composite is air cooled, it shows a 30% reduction in S' formation compared to faster quench rates, but the dissolution peak is unchanged. This supports the theory that S' precipitates were formed during quenching and nucleate heterogeneously on the dislocations formed around the reinforcement particles, rather than at GP zones (49) (68).

Other researchers have also suggested that S' nucleates on thermally generated dislocations (69) (70), giving a fine, dense distribution of S'. Nutt found that S' was not homogeneously distributed within the matrix. Some grains contained fine, dense precipitation, whilst others had far fewer, coarse precipitates. This was attributed to both localised depletion of necessary species and to manganese-containing intermetallics having an effect on the nucleation of S' (17). Dyos hypothesised that coring during solidification of the alloy powder could be a likely explanation for compositional variation between grains (53), but this effect is unlikely, given the rapid solidification nature of the powder production route, followed by mechanical alloying, which acts as a homogeniser.

The enthalpy of formation of metastable precipitates, such as S', is reduced in many composite systems. As these precipitates are often the major age hardening component, a reduction in enthalpy of formation of such magnitude is a possible explanation for the reduced age hardening effect observed in many composites (53). The reduction is often attributed to a lack of GP zones which is believed to inhibit nucleation of subsequent phases, however most phases are thought to nucleate heterogeneously on dislocations, so should be unaffected by the relative abundance of GP zones. The formation of insoluble phases may lead to reduced solute availability, again causing reduced precipitation. Examples of such insoluble phases are:

1. Intermetallics such as, Mg_2Si, AlSiMn (α) and $Al_{20}Cu_2Mn_3$ (known to be insoluble at the solution heat treatment temperature, 505°C)

2. Oxides, produced by solute phases reacting with oxide layers from original powder particle surfaces
3. Products of matrix/reinforcement interface reactions

Thomas and King attribute the reduction in enthalpy of S' precipitation in AA2124/SiC_p to incomplete solutionisation at the standard heat treatment temperature, 505°C. This would leave less solute available to contribute towards age hardening, while the nucleation of precipitates is aided by the high dislocation density (49).

Acceleration of ageing kinetics in Al-alloys produced through powder metallurgy has been frequently observed, with a reduction in the peak temperatures of formation for GP zones, S' and θ' (50) (38) (63) (71). Furthermore, the addition of a reinforcement phase leads to a further acceleration (50) (63). This is accompanied by a reduction in the time taken to reach peak hardness; with no incubation time before precipitation hardening begins.

The high dislocation density is known to have a marked effect on the kinetics of ageing. Pipe diffusion along dislocations is very important for the precipitation of θ' in unreinforced alloys (72). As well as providing nucleation sites for certain precipitates, the increased dislocation density greatly enhances diffusivity (16) (55).

Dislocation loops formed by the condensation of quenched in vacancies are frequently found in composites and can add to the number of nucleation sites available (55). In AA2024, dislocation formation has been seen around manganese intermetallics. These dislocations, together with dislocation loops and helices formed from quenched in vacancies provide nucleation sites, on which S' can form (67). On the addition of a reinforcement phase, dislocations are punched out of the matrix, again contributing to a high overall dislocation density. The net effect is a reduction in the temperature of formation of S'.

It has been observed in an AA2014/Al_2O_{3p} composite there is less S' formation and more θ' formation than for the monolithic alloy (55). Badini also observed that the S' peak was comparatively smaller in a SiC reinforced composite with an AA2024 matrix (38). Both of these findings support the theory that S' tends to nucleate heterogeneously on dislocations, rather than homogeneously at GP zones.

However, it should be noted that there is another school of thought with regards to the precipitation sequence followed by Al-Cu-Mg alloys and specifically the nature of S' nucleation. Certain studies have suggested that the metastable S' phase actually nucleates homogeneously around GP zones. Papazian, having observed that the amount of S' formed was unaffected by the inclusion of SiC reinforcement (50), proposed an alternative theory. He suggested that this was a clear indication that the nucleation of the S' phase was entirely independent of dislocation density. This led him to the conclusion that S' nucleation was not a heterogeneous process, but rather the phase nucleated homogeneously around GP zones.

2.2 Microstructural Characterisation of Metal Matrix Composites

Optical Microscopy

For the purposes of microstructural characterisation, a significant amount of research was carried out to investigate the most commonly applied techniques for the analysis of MMCs. The predominant approach centred around optical metallography and associated specimen preparation techniques (73). In general, such techniques have proven successful on MMCs with a relatively coarse reinforcement particle size (>20 μm) and low volume fraction reinforcement levels (<17%). In these cases, grain structures are relatively coarse and etching provides a simple technique for quantitative analysis of the grain structure.

One specific technique that has been recently developed for aluminium alloys is gallium etching, which involves depositing liquid gallium on a specimen surface (73). The gallium proceeds to attack the grain boundaries and the effect is visible under an optical microscope. The solubility of aluminium in gallium is approximately 2% at the eutectic temperature. In order to minimise the aggressiveness of molten gallium on aluminium MMC specimens, liquid gallium is first saturated with commercially pure aluminium (99.5%) before applying it to a specimen surface. An additional benefit of this technique is that the gallium becomes molten at room temperature and this simplifies the application procedure. After an exposure time of three hours, the grain boundary attack was visible under an optical microscope.

Scanning Electron Microscopy and Electron Backscattered Deflection

Other studies have shown that electron back scattered diffraction (EBSD) can be successfully performed on low volume fraction MMCs (74). Specimens were prepared by conventional diamond polishing, followed by low angle ion beam milling to reduce the topography of the reinforcement phase. In regions where the particulate phase distribution was relatively sparse, EBSD mapping proved to be effective. Closer to the matrix/reinforcement interface, however, mapping was inhibited due to the shadowing effect of the protruding ceramic particles on the low angle incident beam.

For MMCs with finer reinforcement particles at higher volume fractions, this problem is exacerbated as interparticulate spacing decreases. Additionally the fine grained nature of such alloys means that a very small beam width is required to index individual grains/subgrains and this is beyond the capabilities of equipment that is currently available.

Transmission Electron Microscopy

Transmission electron microscopy (TEM) has been successfully applied to MMCs but with certain limitations. There is an inherent difficulty in preparing a flat surface on an MMC because of the presence of a hard ceramic phase in a soft matrix. Techniques such as grinding, diamond polishing and electropolishing all have the effect of preferentially removing the matrix leaving the ceramic phase to protrude from the surface of the specimen. The problem is particularly acute in TEM specimen preparation as the regions close to the matrix/reinforcement interface tend not to be electron transparent. As for the EBSD mapping, if interparticulate spacing is high this does not create a major issue because large regions of the matrix are available for viewing. For composites with small interparticulate spacing, the viewable area is greatly restricted by the presence of "un-thinned" regions and analysis of the matrix/reinforcement interface is impossible.

It has been demonstrated that by applying a low energy ion beam at an angle of 6° to the surface of an electropolished MMC specimen, it was possible to remove some of the ceramic protrusions and thus provide a sample that was more uniformly thinned. Even in this case, analysis of the matrix/reinforcement interface proved to be a challenge (53).

The other limitation of TEM analysis is not uniquely relevant to the study of MMCs. The electron transparent area available for analysis for a single TEM specimen is limited, necessitating the preparation of multiple samples for a representative study of the microstructure. Due to the fact that MMC samples can take at least ten times the amount of time to prepare compared to monolithic alloys (10), it was decided that it would not be possible to prepare enough specimens during the course of the project to provide a representative quantitative analysis of the typical microstructure for each process condition. Contemporary techniques, such as EBSD provide an opportunity for rapid analysis of relatively large areas and proving whether this approach was possible was considered to be one the primary objectives of the current work. TEM would still however be available as tool for conducting high resolution analysis of specific microstructural features.

Focussed Ion Beam Microscopy

The focussed ion beam (FIB) system based on a gallium liquid-metal ion source became commercially available in the late 1980s (14) (12). The total number of systems in use worldwide by the end of the century was approximately seven hundred, a relatively small number compared to SEMs and TEMs. Until recently the primary use of a FIB microscope has been in the semiconductor industry in precision sectioning to a submicron scale and metal deposition on a substrate. The speed of development of today's commercially available FIB system can be attributed predominantly to the semiconductor industry. The primary use of the FIB system in materials science has been for site-specific preparation of TEM specimens. Currently available FIB systems now have spatial resolutions equivalent to those of conventional scanning electron microscopes. This has unlocked the potential of the FIB microscope as an imaging tool in addition to its milling and deposition capabilities.

The FIB microscope operates in a similar fashion to an SEM in that it rasters a beam of charged particles across a specimen surface and then detects the resultant signal to form an image. Rather than negatively charged electrons, the FIB primary beam consists of positively charged gallium ions from a liquid-metal ion source (Ga-LMIS). Typical resolutions of 5 nm or better are available from such an instrument. A FIB microscope can detect both secondary electrons and secondary ions, which are emitted from a specimen surface by a process known as sputtering.

In the late 1990s, the combination of in-situ FIB sectioning and FIB polishing proved to be a powerful technique in materials science due to the increased resolution capability of modern FIB equipment. The clear benefit over conventional techniques is the ability to perform site-specific analysis to a nanometre scale of accuracy. The technique is also highly suited to fragile specimens where conventional techniques would likely inflict mechanical damage and bring about microstructural modifications.

FIB imaging is performed by detection of either secondary ions or secondary electrons, which are emitted from a specimen surface during the interaction between atoms located in the proximity of the specimen surface and the incident gallium ion beam. Secondary electrons are collected by a microchannel plate biased positively, in the case of secondary electron detection, and negatively, for positive secondary ion collection.

Image contrast mechanisms fall into three separate categories, namely: crystallographic orientation contrast, atomic weight contrast and topographic contrast. Orientation contrast is of specific interest for the study of metallic specimens in that it permits the analysis of ultrafine grain structures, which are not observable through conventional optical techniques. The details of each technique will be outlined in Section 4.6: Microstructural Analysis of Aluminium MMC by FIB Imaging.

TEM Preparation by Focussed Ion Beam Specimen Preparation

Transmission Electron Microscopy provides a useful tool for microstructural characterisation of metals and alloys, permitting the determination of crystallography, phase morphology and chemical composition. It has also been successfully applied to metal matrix composites (10). The specimen thickness required for electron transparency is a function of material density and electron beam energy but is typically in the order of less than 100 nm (75).

Even without the presence of a ceramic particulate reinforcement phase, conventional Powder Metallurgy (PM) alloys are often difficult to prepare. This is mainly due to the presence of considerable porosity and the imhomogeneity of the microstructure. Conventional techniques, such as electropolishing and ion beam thinning tend to interfere with the interfaces of the sintered particles, preventing a coherent electron transparent film from being achieved.

The capability of the FIB system to produce in-situ stress free site-specific TEM specimens has been widely documented in recent years (76). The technique has been applied to semiconductors and powder metallurgy metallic alloys that are notoriously difficult to prepare by conventional means such as electropolishing. The FIB equipment is capable of preparing a site-specific section with a positional placement accuracy in the order of 20 nm (14).

Several researchers have documented the capability of the FIB to perform site-specific TEM specimen preparation (77) (78) (79) (80). In each of these cases an "H-bar" technique was employed whereby a specific region is loaded onto a TEM grid and milled to an electron transparent thickness. An alternative technique known as "lift-out" was developed whereby an electron transparent membrane is milled in bulk material (11) (81). The section is then cut free from both ends with the ion beam and lifted out of the bulk material by means of a needle tool. The membranes are mounted onto a copper grid for subsequent TEM analysis. Each technique has its relative merits. The "H-bar" process is useful for specimens that are already relatively thin (<150 μm). On inspection in a TEM, if the membrane is found not to be electron transparent, it can be reinserted into the FIB and further milling completed to achieve the correct section thickness. The advantage of the "lift-out" technique is that it can be carried out on bulk material and it can be fully automated by running a script. The disadvantage is that cutting and removing the specimen can inflict micro-mechanical damage and artificially modify the appearance of the specimen under the TEM.

The earliest reported FIB preparation of TEM slides on metallic specimens involved nickel and magnesium-zinc alloy powders (82). Such fine powder specimens are difficult to prepare by conventional means. The study was highly successful in revealing detailed microstructural features such as grain structure and dislocations. An evaluation of the accuracy of site-specific specimen preparation was carried out by Saka et al. (83). It was shown that "H-bar" specimens could be fabricated by the FIB technique to observe crack tips generated by a Vickers Hardness indenter in single crystals of silicon.

McPhee et al. demonstrated the capability of the FIB technique to prepare TEM specimens from a sintered powder metallurgy aluminium alloy (84). An aluminium-copper-magnesium alloy was sintered from mixed elemental powders. Slices were cut to a thickness of 1mm, punched and ground further on 1200 grit SiC grinding paper to a

thickness of 150 μm - 200 μm. Discs were ground on a Gatan Disc Grinder to a final thickness of 20 μm and a razor blade was used to cleave a straight edge at the centre of the specimen. The cleaved edge was then milled and polished using the FIB technique to a final thickness of approximately 100 nm. It was discovered that by directing the beam parallel to the surface of the disc, a wedge shaped film would form due to the sputtering of the ion beam (Figure 2.3a). By tilting the top of the specimen away from the beam at an angle of 3°, a parallel sided film could be achieved (Figure 2.3b).

The size of the electron transparent area achieved was approximately 600 μm^2. The microstructure of the alloy was clearly visible indicating that the introduction of mechanical damage and artefacts was kept to a minimum during FIB preparation. EDAX EDS analysis showed some gallium contamination from the ion beam.

It was concluded that the technique provided a very useful tool for preparation of powder metallurgy TEM specimens from bulk material in a relatively short space of time.

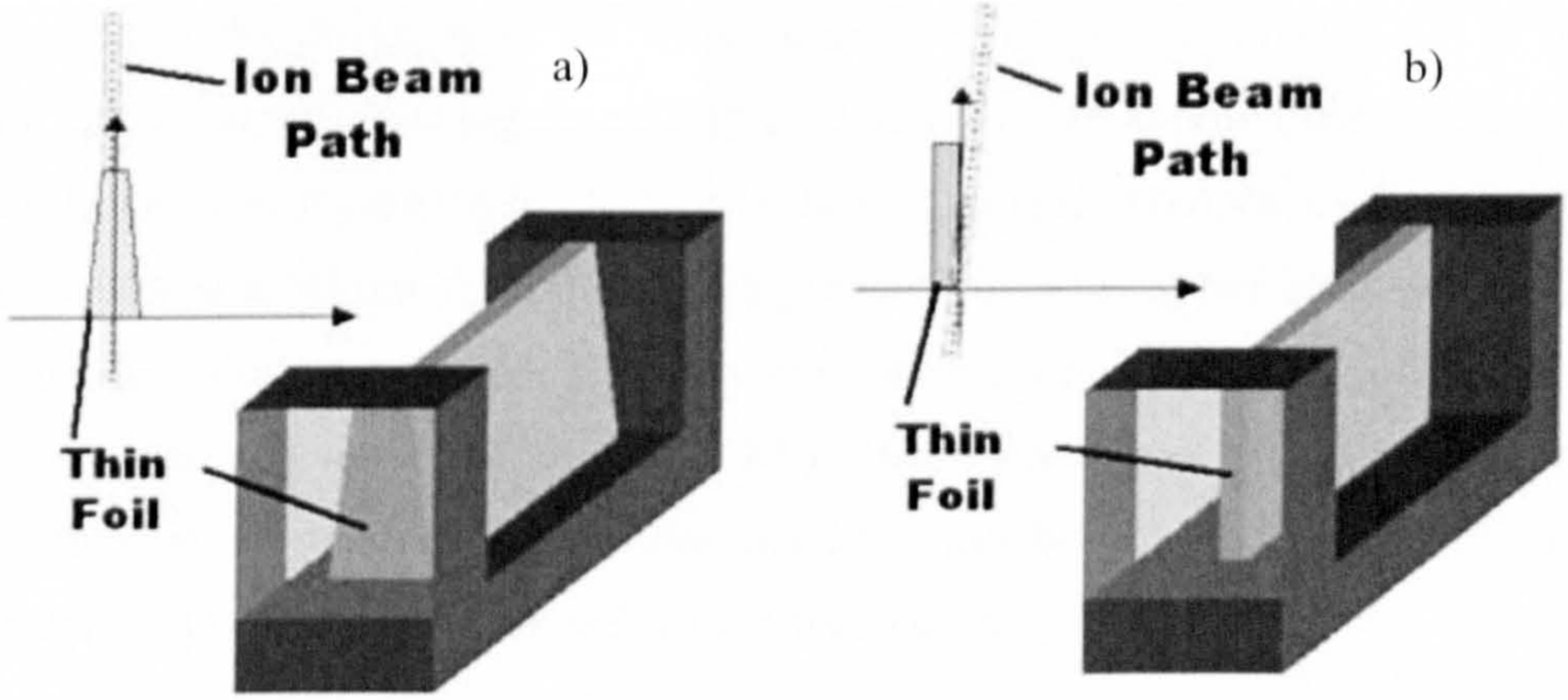


Figure 2.3 - A schematic diagram of the thin film in a FIB sample showing (a) the wedge shape film that the ion beam produces, and (b) the parallel sided film that can be produced by tilting the top of the sample away from the ion beam. Adapted from McPhee et al. (84).

The issue of surface damage to TEM slides during FIB preparation has previously been reported and is of relevance to the current study (85). It is essential to understand the damage brought about by the process in order to correctly interpret both the microstructural and chemical analysis data.

A range of modifications can be made to a TEM film during preparation by the FIB technique. These include mechanical damage, artefact deposition and surface amorphisation.

Mechanical damage is brought about due to residual stresses being relieved as the film thickness steadily decreases to electron transparency. This can lead to the build up or even recovery of dislocation structures that were not apparent in the bulk material and may have a significant bearing on the appearance of the microstructure.

Artefact deposition occurs as a result of the gallium ions from the ion beam source embedding themselves in the surface layers of the material. This effect can be relieved to a certain extent by a subsequent low energy, low angle (less than 6°) ion beam milling stage, which has the effect of sputtering the previously deposited gallium ions.

Surface amorphisation is a process whereby the atomic planes close to the surface of the specimen are disrupted by the incident ion beam. There is some uncertainty as to how much amorphous damage is produced by the sputtering mechanism (86). It has been reported that the thickness of the amorphous layer is directly proportional to the ion beam energy supplied during the milling process (87). The approximate thickness of an amorphised layer measured in an aluminium metal matrix composite was 10 nm (88). This means in a 50 nm thick TEM film prepared by FIB, approximately 40% of the material has been amorphised. This may have an impact on the clarity of the observed selected area diffraction patterns (SADPs). However, it has been shown that high resolution lattice images of crystalline materials can be obtained from FIB prepared specimens using both the h-bar and lift-out techniques.

A study into the FIB induced damage on an interstitial free steel showed that in the FIB irradiated area, there was a large amount of gallium implanted in the surface (89). A quantitative EDX analysis at the specimen surface showed a chemical makeup of 24.7 weight % gallium in the steel and at 20 nm below the surface this level dropped to 3.4 weight %.

It has also been shown that by using a low energy beam applied at a low incident angle (less than 6°), it is possible to produce a silicon TEM film with a surface condition similar to that of a cleaved surface (considered to be the least damage-inducing

approach for TEM specimen preparation of Silicon) (90). This type of work has previously been carried out on an aluminium MMC reinforced with 20 μm SiC particulate (91). Following preparation by FIB, a Precision Ion Polishing System (PIPS) was used to aim positively charged argon ions at a rotating specimen, at an angle of 0.5° to the surface. After one hour of polishing, the height difference between the matrix and reinforcement had been reduced by 75%. Additionally, the deposition of a 2 μm thick layer of platinum has been shown to offer significant protection from the effects of ion beam damage on specimens.

Although TEM specimens of many different materials, including PM alloys, have been successfully prepared by FIB, the preparation of powder metallurgy MMCs by this technique has not been widely reported in the literature.

3 Experimental Methods

3.1 Materials Studied

The material studied was a commercially produced powder metallurgy (PM) composite known as "AMC225xe," which was manufactured by Aerospace Metal Composites Ltd., Farnborough, U.K. The material consists of an aluminium alloy, AA2124 matrix, reinforced with 25 volume % SiC particulate with a nominal size of 3 - 5 μm. The compositional limits of AA2124 are shown in Table 3.1, below.

Table 3.1 - AA2124 composition (wt %)

Al	Cu	Mg	Mn	Fe	Zn	Ti	Cr
Balance	3.8-4.2	1.2-1.8	0.3-0.9	<0.3	<0.25	<0.15	<0.1

The AA2124 powder was produced by rapid solidification - gas atomisation. This was blended with the SiC particulate and Mechanically Alloyed (MA). The mechanically alloyed powder was degassed and consolidated to billet by Hot Isostatic Pressing (HIP). All subsequent processing operations were carried out at Imperial College London.

3.2 Extrusion

An ENEFCO 500 Tonne press was used to carry out the extrusion work. A billet of 58 mm diameter x 700 mm was cut into five sections, each approximately 100 mm in length. Each section was extruded in a 60 mm container, through flat-faced dies lubricated with graphite, at a constant speed of 1.8 mms^{-1} (1.8 x 10^{-3} ms^{-1}). The various extrusion temperature and extrusion ratio conditions used are detailed in Table 3.2, below.

Table 3.2 - Extrusion conditions

Billet Number	Extrusion Temperature (°C)	Extrusion Ratio
6139-1	450	20:1
6139-2	550	20:1
6139-3	450	10:1
6139-4	450	5:1
6139-5	350	20:1

A small hole was drilled into the base of each billet in order to locate a thermocouple and therefore accurately monitor the billet temperature during preheating. Each billet was soaked for 2hrs (±10 minutes) to achieve the required extrusion temperature. The extrusion die was preheated to 50°C below the extrusion temperature to prevent excessive heat loss from the billet during the process. Following extrusion, the material was air-cooled.

For the purposes of this study, the longitudinal extrusion direction is defined as the direction parallel to the axis along which the material was extruded. Conversely, the transverse extrusion direction is the direction that lies in the plane perpendicular to the axis along which the material was extruded.

3.3 Heat Treatment

After the material had cooled to room temperature it was solution heat treated in a Carbolite furnace at 505°C (±5°C) for one hour. It was then transferred in less than five seconds to a cold water quench maintained at a steady temperature of 18°C (±1°C). Finally, it was allowed to naturally age at 23°C (±5°C) for 100 hours, following the 'T4' designated AMC heat treatment route. Standard uniaxial tensile and rotating bend fatigue specimens were machined from the heat treated material.

3.4 Tensile Testing

Tensile tests were carried out on an Instron 8061 servo-hydraulic testing machine. A clip-on extensometer with a gauge length of 25 mm was used to measure strain. The sample itself had a gauge length of 30 mm, and a round cross-section with a diameter of 5mm. A strain rate of 0.00025 sec^{-1} was applied prior to yield and this was increased to 0.00183 s^{-1} beyond yield, according to BS EN 10002-1 for room temperature tensile testing. For each test, a chord modulus was calculated between 25 MPa and 100 MPa stress. Values for 0.1%, 0.2% and 0.5% proof stress were recorded as well as the ultimate tensile strength and the total strain to failure. Signals from the machine were converted to a ±2500 mV range and outputted to a Pico ADC-16 converter unit, which was connected to the serial port of a computer. The computer was running PicoLog data-logging software to enable real-time data capture and analysis. All data presented in the results section include error bars to indicate experimental data scatter based on a ±2 standard deviation statistical assessment.

3.5 Rotating Bend Fatigue Testing

Fatigue testing was carried out on a Rolls-Royce Rotating Bend Fatigue Testing Machine. Specimens were un-notched (Kt = 1) and the stress ratio (R) was -1. The test frequency was 48 Hz. Initial bending loads were calculated based on data from the literature under room temperature conditions (34). The applied bending stress was calculated using standard equations and the number of cycles to failure was recorded.

3.6 Specimen Preparation for Optical Microscopy

Specimens of AMC225xe for optical microscopy were prepared according to the following procedure. All specimens were mounted in a phenolic hot mounting resin. SiC grinding paper has been shown to provide an inferior surface finish to diamond abrasives due to high wear rates of the SiC reinforcement particles in the MMC on the grinding paper (73). Specimens were instead ground and polished using diamond abrasives with appropriate lubricants on a Struers TegraPol Modular Preparation System. Each of the following stages was carried out for approximately 3 minutes:

1. MD-Piano 120 with water lubricant
2. MD-Allegro, DP Susp P 9 μm with DP-Blue lubricant
3. MD-Plan, DP Susp P 9 μm with DP-Blue lubricant
4. MD-Dac, DP Susp P 3 μm with DP-Blue lubricant
5. MD-Nap, DP Susp P 1 μm with DP-Blue lubricant
6. OP-Chem Cloth with OP-S Suspension

3.7 Grain Size Determination

Due to the highly refined nature of the grain structure of AMC225xe, optical microscopy did not provide sufficient resolution to resolve the grain structure of the material. For this reason Focussed Ion Beam Microscopy was used as an alternative technique as it provided greater resolution. For the purpose of grain size analysis, secondary electron images were captured at a magnification of 10,000 times, which represented an area of approximately 900 μm^2. Grain size determination was carried out according to ASTM International Standard Test Methods for Determining Average Grain Size (92) according to the Planimetric Procedure.

Initially, the percentage area of SiC particles in a single image was measured by applying a threshold to each micrograph in ImageJ Image Analysis Software (93).

Grains were then counted according to the ASTM procedure. The number of grains per square millimetre, N_A, was determined through the following equation:

$$N_A = f\left(N_{Inside} + \frac{N_{Intercepted}}{2}\right)$$

Equation 3.1

where f is the Jeffries' Multiplier, N_{Inside} is the number of grains within the analysis area and $N_{Intercepted}$ is the number of grains that intercept the perimeter of the analysis area. The Jeffries' Multiplier was calculated as 20,000 for a magnification of 10,000 times. The average grain area, A, is the reciprocal of N_A and the mean grain diameter, d, is the square root of A. Where appropriate, error bars are included with the data to indicate scatter and are based upon a ±2 standard deviation statistical assessment.

3.8 Transmission Electron Microscopy – Conventional Sample Preparation

Conventional techniques such as jet polishing are unsuitable for the thinning of metallic composites samples with fine reinforcement particles as they preferentially polish the matrix in favour of the reinforcement, giving unevenly thinned films, thus preventing successful analysis of the matrix/reinforcement interface. This phenomenon is illustrated in the schematic, below.

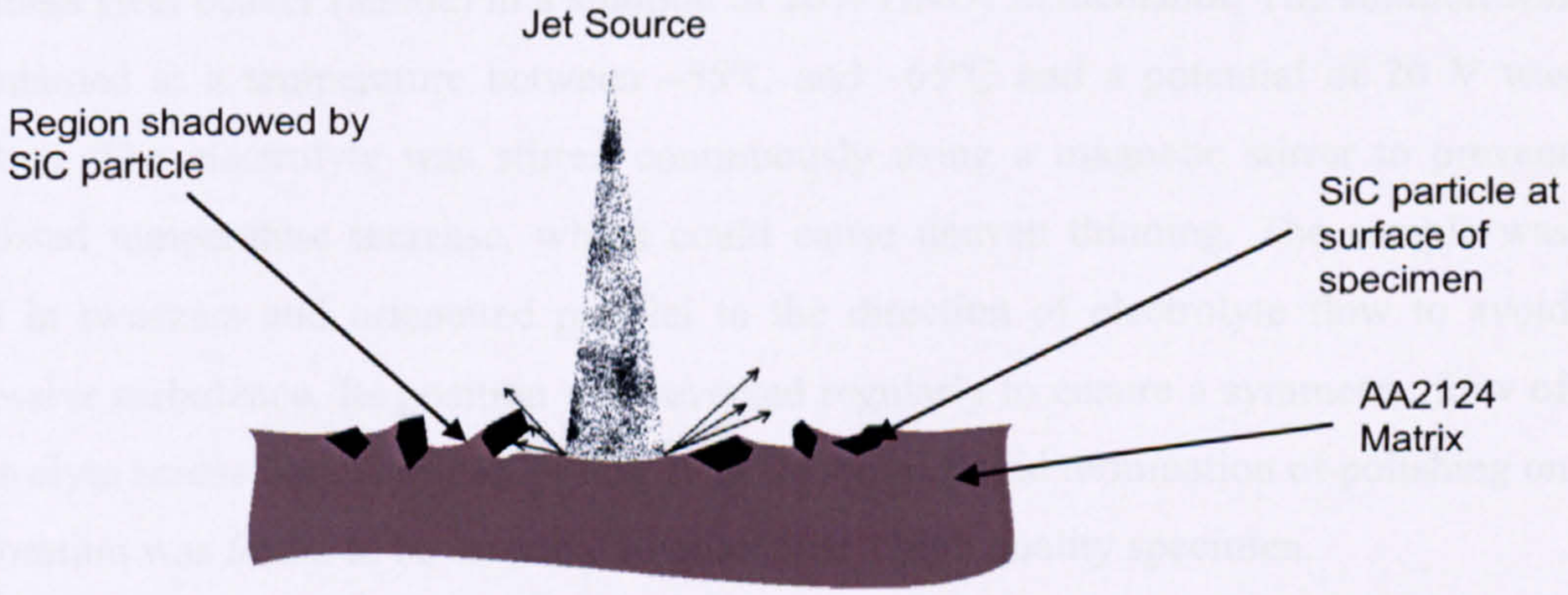


Figure 3.1 - A Schematic of the uneven thinning characteristics using the jet polishing technique

Evans and Boyd prepared samples from a similar material using a standard technique. Thin discs were produced and dimpled to a 10 μm central thickness. An ion-beam mill was then used to produce electron-transparent regions (10). This technique was shown

to be highly effective for analysing the matrix/reinforcement interface by providing even thinning of both phases, however, the process was time consuming.

Despite this limitation, it was decided that the technique would be applied to AMC225xe to offer a comparison to the novel techniques developed as part of the current study. Electropolishing using the "window technique" has been previously performed on AMC225xe with a reasonable degree of success (53), so a similar technique was applied for the current study. 3.0 mm discs were spark eroded from material with an initial thickness of less than 0.5 mm. It has previously been shown that prior dimpling or improved surface finish has little effect on the final quality of the film (53).

The simplest route for producing an electron transparent specimen was found to be as follows:

1. Hand grinding discs on coarse (240 grit) SiC paper to 150 μm thickness.
2. Electropolishing

Prior to electropolishing, lacquer was painted around the edge of the sample (cathode) to ensure that only the middle section was thinned. Electropolishing was carried out in a stainless steel beaker (anode) in a solution of 20% HNO_3 in methanol. The solution was maintained at a temperature between –55°C and –65°C and a potential of 20 V was applied. The electrolyte was stirred continuously using a magnetic stirrer to prevent localised temperature increase, which could cause uneven thinning. The sample was held in tweezers and orientated parallel to the direction of electrolyte flow to avoid excessive turbulence. Its position was reversed regularly to ensure a symmetric flow of electrolyte across both surfaces, giving even thinning. Rapid termination of polishing on perforation was found to be essential to guarantee a high quality specimen.

After polishing, the sample was washed in methanol, then ethanol and finally in clean methanol. The lacquer was then stripped away and a final methanol wash was repeated. The whole process had to be completed as quickly is possible to prevent the lacquer from hardening and therefore becoming difficult to remove.

Transmission Electron Microscopy was carried out on a JEOL 2000FX microscope operating at 200 kV. Both bright and dark field imaging and electron diffraction were conducted on this microscope.

3.9 Focussed Ion Beam – Specimen Preparation and Imaging

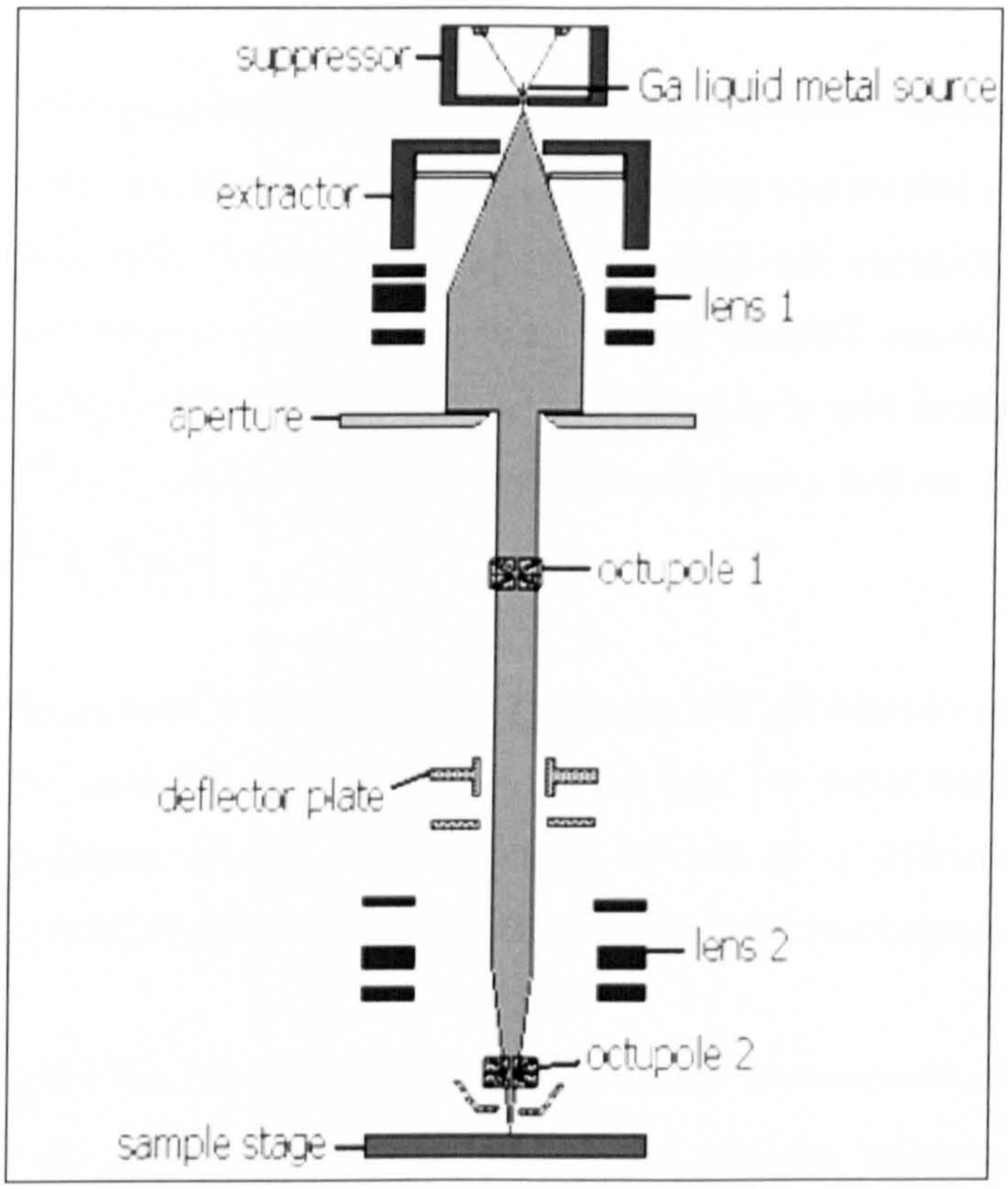


Figure 3.2 – Schematic of a Focussed Ion Beam Microscope

Focussed Ion Beam (FIB) milling, polishing and imaging were performed on an FEI Strata 200 TEM Focused Ion Beam Secondary Ion Mass Spectrometer. As shown schematically in Figure 3.2, a liquid metal source is subjected to an accelerating voltage of 30 keV and emits a beam of ions which is focused by a combination of lenses, octupoles and apertures to a spot size on a sample surface of several nanometres in diameter. The beam current may be varied from 50 pA - 30,000 pA. At high beam currents, sputtering rates are high so material removal is achievable through a process known as "milling." At low beam currents (<100 pA) sputtering rates are significantly lowered, so a sample can be imaged by the detection of Secondary Ions and Secondary Electrons emitted from a sample surface.

During the specimen preparation of TEM slides by FIB milling and polishing, it was necessary to protect the edge of the thin film at the region of interest by the ionisation of platinum gas to produce a 2 μm - 3 μm thick strip of platinum on the surface of the specimen. Further details of the development of the FIB technique can be found in Section 4.6: Microstructural Analysis of Aluminium MMC by FIB Imaging.

3.10 Elevated Temperature Compression Testing

Elevated temperature compression testing was carried out on an Instron 3369 Universal Materials Testing Machine, with a load cell capacity of ±50 kN. The machine was linked to a computer running Instron Bluehill software which provided control and monitoring facilities. Heat was supplied by a split furnace capable of operating at up to 1200°C. A thermocouple was inserted into a hole in the lower plattern to control the temperature.

Specimens were wire eroded from as-HIP'ed billet to cylindrical samples with a radius (R) of 4 mm and a length (L) of 10 mm. For room temperature testing, PTFE tape was wrapped around the specimens to act as a lubricant. At elevated temperatures, specimens were coated in a Boron Nitride Aerosol spray for the same purpose.

After the lower plattern had achieved the set temperature, specimens were placed inside with tongs, the furnace was closed and the upper plattern was lowered onto the specimen at a preload of 10 N. The temperature was allowed to equilibrate for five minutes prior to commencing the test. Tests were run in constant strain rate modes, controlled by the software on the connected computer. Testing was carried out according to the matrix shown in Table 3.3.

Table 3.3 - Compression Testing Matrix

Strain Rate	Temperature (°C)				
	23	350	400	450	500
0.0001 /s	X	-	-	-	-
0.001 /s	X	-	-	-	-
0.01 /s	X	X	X	X	X
0.1 /s	X	X	X	X	X
1 /s	X	X	X	X	X

3.11 X-Ray Diffraction

X-Ray Diffraction (XRD) techniques were applied to determine the macro textures of material fabricated under a range of extrusion temperatures and extrusion ratios. Experiments were carried out on a Philips PW1710 X-Ray Diffractometer, using Cukα radiation, which has a wavelength of 0.154060 nm.

Material specimens were approximately 8 mm in diameter by 5 mm thick and in the T4 cold water quench heat treatment condition. They were machined perpendicular to the extrusion direction. It was not necessary to polish the surface prior to analysis as a polished surface can lead to a reduction in the X-Ray yield.

Specimens were rotated and tilted simultaneously, so that sections of pole figures could be obtained for a single grain orientation. The pole figure orientation range (alpha angle) was set to 0° – 60°. All pole figures were corrected using machine specific factors as defined by reference samples, to account for the defocusing effect and changeable penetration depths.

4 Results and Discussion

4.1 The Influence of Extrusion Temperature on Tensile Properties

The graph, below, of extrusion load versus ram displacement (Figure 4.1) shows an increase in the peak load with a decrease in extrusion temperature. However, the plastic deformation behaviour was found to vary with temperature. At an extrusion temperature of 350°C, the extrusion load steadily decreased after the peak load had been achieved, showing apparent work-softening type behaviour. This trend was also observed at 450°C. At an extrusion temperature of 550°C, the plastic deformation behaviour was markedly different, with an increasing load required to maintain plastic flow.

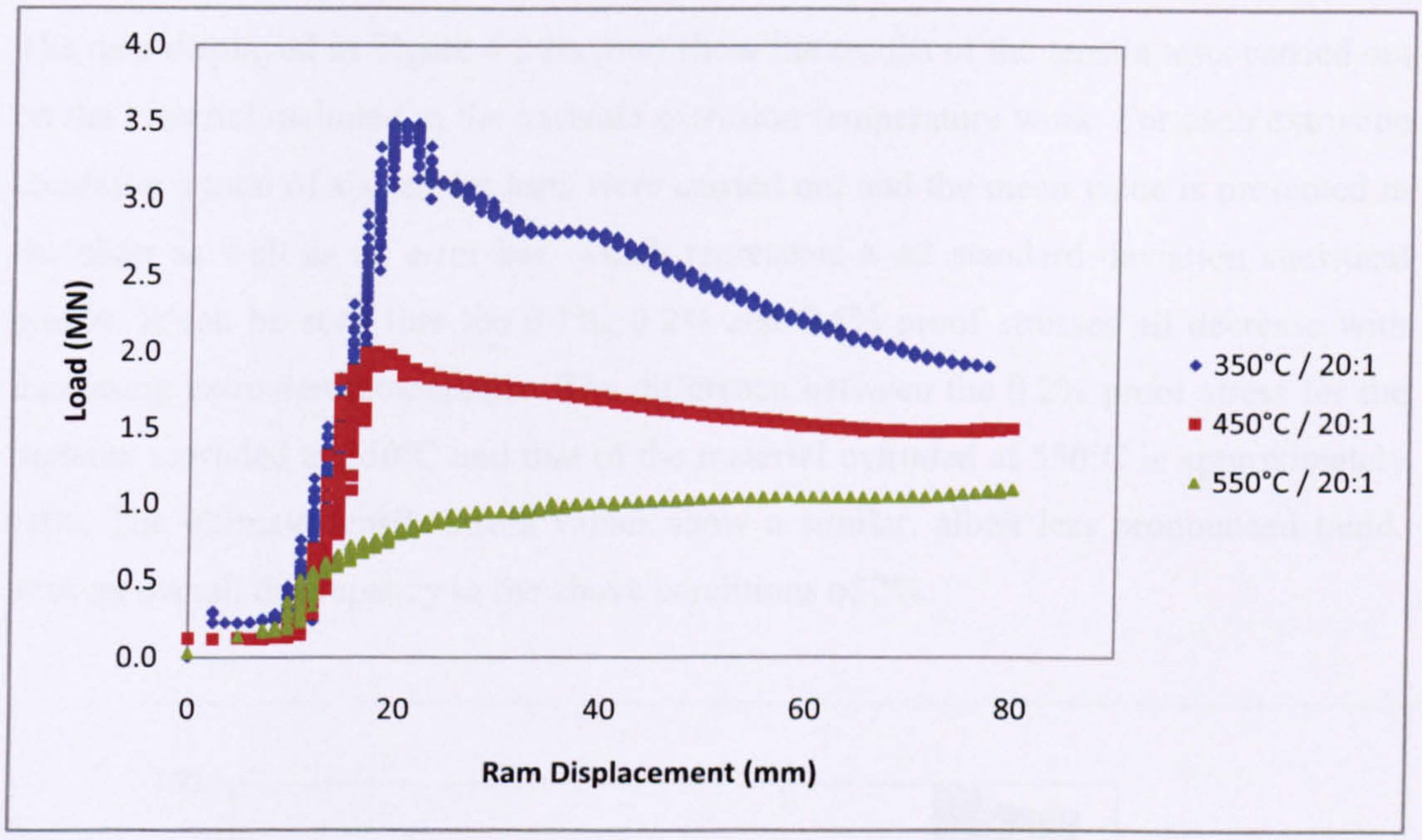


Figure 4.1 - Extrusion load versus ram displacement for range of extrusion temperature

These observations could be explained by the fact that at the two lower extrusion temperatures, there may be an adiabatic heating effect on the billet during extrusion so the process is not truly isothermal. As the billet temperature rises, the flow stress diminishes, giving the characteristic downwards slope. Another possible mechanism has been highlighted in previous studies, whereby dynamic recovery and recrystallisation may be occurring during extrusion at relatively low temperatures due to high stored energy within the MMC (30). This would cause dislocation mobility to increase, therefore progressively lowering the stress required to overcome the resistance to plastic deformation. At higher extrusion temperatures (above 450°C), grain/sub-grain growth

may begin to occur, albeit at a relatively slow rate. As the deformation mechanism is predominantly inter-granular at such temperatures, an increase in the average grain size causes a reduction in the available grain boundaries along which plastic deformation can occur, leading to an overall increase in the stress required to enable continuous plastic flow. These results have been previously observed in other studies of the same material (94) and are also know to occur in certain monolithic aluminium alloys (e.g. Al-Fe-V-Si) produced through a powder metallurgy / mechanical alloying route (95). The common features of such materials include their energy intensive processing route and the resulting highly refined microstructure as well as the presence of oxides and carbides which may act to pin grain boundaries.

The data displayed in Figure 4.2 (below) show the results of the tensile tests carried out on the material included in the variable extrusion temperature work. For each extrusion condition a total of six tensile tests were carried out and the mean value is presented in the chart as well as an error bar, which represents a ±2 standard deviation statistical scatter. It can be seen that the 0.1%, 0.2% and 0.5% proof stresses all decrease with increasing extrusion temperature. The difference between the 0.2% proof stress for the material extruded at 350°C and that of the material extruded at 550°C is approximately 10%. The ultimate tensile stress values show a similar, albeit less pronounced trend, with an overall discrepancy in the above conditions of 2%.

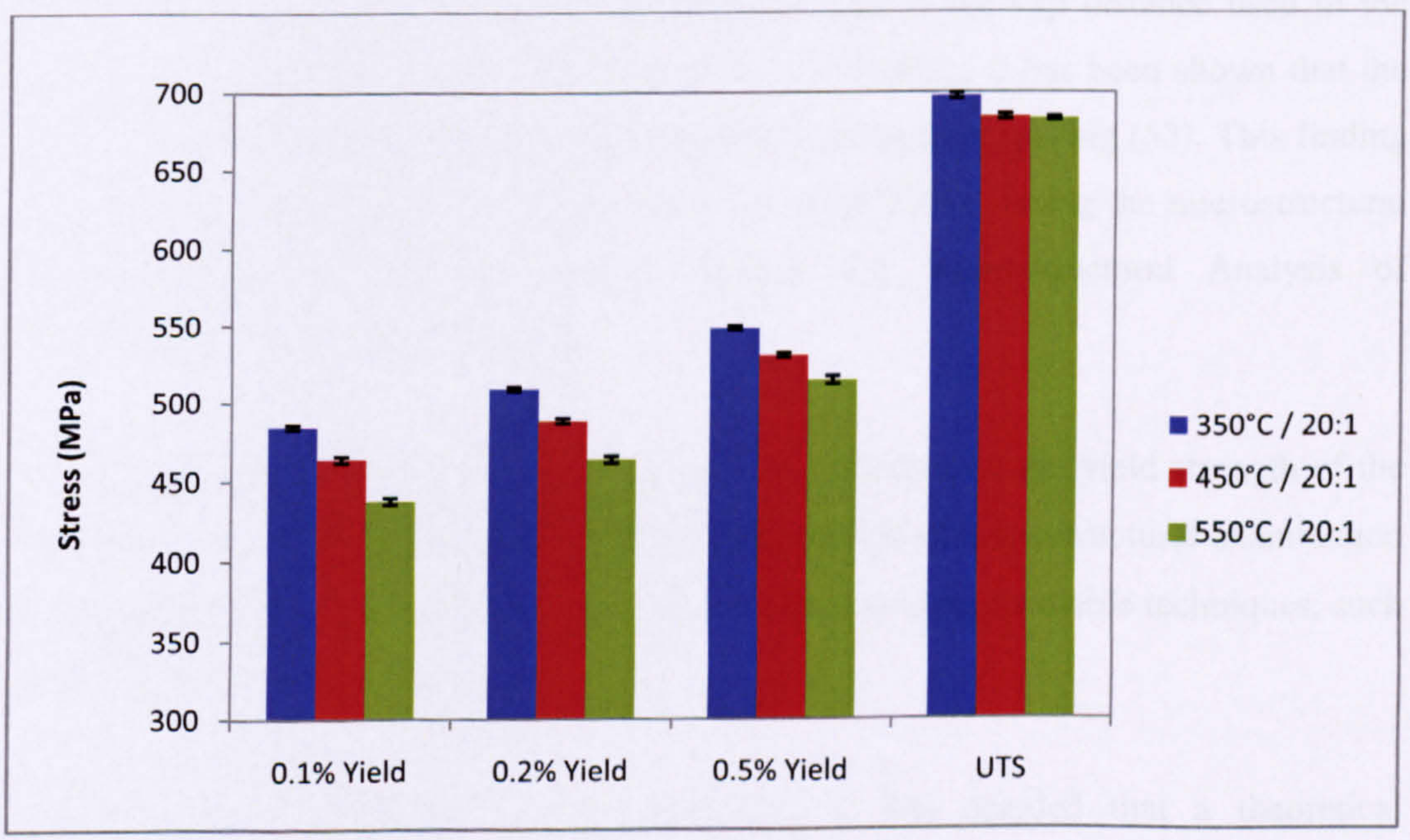


Figure 4.2 - Influence of extrusion temperature on tensile properties of composite

In order to understand and explain the mechanisms contributing to this behaviour, classical metallurgy theories should be applied.

In conventional monolithic alloys the Hall-Petch equation has been widely used to demonstrate the relationship between the average grain size and the yield stress of the material. It shows how a material's yield stress is inversely proportional to its average grain size. The equation has also been applied to metal matrix composite materials with a high degree of success. In fact, much of the literature suggests that Hall-Petch strengthening and Forest Hardening are considered to be the most important interactions with regards to composite strengthening (29). The Hall-Petch relationship predicts that:

$$\sigma_y = \sigma_0 + kD^{-\frac{1}{2}}$$

Equation 4.1

where:

σ_y – tensile yield stress

σ_0 – yield stress of single crystal of similar composition and dislocation density

k – locking parameter (material constant)

D – slip distance

The slip distance, D, is not always defined as the grain/subgrain size and if the reinforcement inter-particle separation is smaller, this is the slip distance used in the Hall-Petch relationship. In the case of AA2124 / 17% SiC_p, it has been shown that the average grain size is less than the reinforcement inter-particle spacing (53). This finding has also been validated by the current study on AMC225xe during the microstructural characterisation by FIB microscopy (Section 4.6: Microstructural Analysis of Aluminium MMC by FIB Imaging).

To determine the relative influence of grain/sub-grain size on the yield strength of the material, it was considered necessary to conduct a detailed microstructural examination of specimens subjected to all three extrusion conditions using available techniques, such as TEM and FIB microscopy.

Before such an investigation was undertaken, it was decided that a theoretical calculation should be made in order to predict the actual variations in grain size that

would be required in order to give the observed variation in yield stress values, if the discrepancies observed could be entirely attributed to grain growth and no other strengthening mechanisms were involved.

It is possible to use the Hall-Petch Equation for comparative purposes for this material by using a value of 16 MPa for σ_0, taken from the literature (96) and $k = 0.26$ MPa$\sqrt{m}$, as given by Hull et al. for high angle grain boundaries in an Al-Cu-Mg alloy (97). It must be remembered that both of these values have been taken for the monolithic alloy, so serve only to act as an indication. The actual value of the locking parameter, k, is subject to some debate because it is dependent upon whether a subgrain structure exists or whether grain boundaries are of the high angle type. These factors will be considered in more detail subsequently. The limitations of the current technique are acknowledged.

Therefore,

$$\sigma_y = 16 + (0.26 \times D^{-\frac{1}{2}})$$

Equation 4.2

Thus, a hypothetical value for d can be calculated through the following equation:

$$D^{-\frac{1}{2}} = (\sigma_y - 16)/0.26$$

Equation 4.3

This hypothetical value can be compared to the data for the other two extrusion temperatures and expressed as a percentage. An arbitrary value for the actual grain size of a typical grain in the material extruded at 550°C was chosen as 1 μm. The values for the other two conditions were calculated and the difference in the grain size was expressed in microns. Based on a TEM magnification of fifty thousand times, the predicted equivalent difference in grain size on a TEM micrograph was calculated, as shown in Table 4.1, below.

Table 4.1 - Calculation of grain size variations

Extrusion Temperature (°C)	0.2% Proof Stress - σ_o	Hypothetical 'D-value'	% of D-value at 550°C	Estimated Grain Size (For grain size = 1μm at 550°C extrusion)	Difference	Equivalent difference on negative (for TEM Mag = 50K)
350	492.8	2.68E-06	91.4%	0.85 μm	0.15 μm	7.5 mm
450	471.1	2.93E-06	92.8%	0.93 μm	0.07 μm	3.5 mm
550	453.9	3.16E-06	100	1.00 μm	0	0

It can be seen that if the difference in yield stress for the three extrusion temperatures could be entirely attributed to grain size variations, the difference in 'magnified' grain size on the TEM negatives would be up to 7.5 mm for 350°C and 550°C extrusion temperatures. This would certainly be discernable and therefore it is proposed that a microstructural evaluation of grain/sub-grain structure is carried out in order to compare actual values against the theoretical data. If no distinction in grain size is observed for the three extrusion conditions, other strengthening mechanisms must be considered as candidates for the source of the discrepancies in yield stress values.

If alternative strengthening mechanisms are considered, the question as to whether there is a high prevalence of low or high angle grain boundaries in the composite becomes pertinent. It is possible that recrystallisation may occur during processing at elevated temperatures and thus influence the mechanical properties of the material (53).

Another possible cause for the decrease in tensile strength with increasing extrusion temperature is the formation of an interfacial layer at the matrix/reinforcement interface at elevated temperatures. This phenomenon was observed by Evans and Boyd in a similar material (AA2080/SiC_p) but has not yet been shown to occur in AA2124/SiC_p. It was suggested that the extrusion process, carried out at 510°C, led to an increase in the thickness of an amorphous layer consisting of Si, Mg, Al and O, due to interdiffusion with the Al_2O_3 surface layer on the AA2080 powder. TEM observations showed that decohesion occurred by fracture through the interfacial layer. Another study on an AA2124 / 25%SiC_p composite, produced through semi-solid forming, observed an Al_4C_3 layer forming at the particle/reinforcement interface, when the material was processed at temperatures exceeding 550°C (73).

For the material in the current study, the mechanical alloying process ensures that this surface oxide layer becomes fragmented and evenly distributed throughout the material, but there is still a likelihood that it could also be in contact with the SiC particles, following consolidation. It therefore follows that as the extrusion temperature is increased, the potential for an interfacial layer to develop also increased, as rates of diffusion are accelerated. Subsequent heat treatment operations would have an equivalent effect on this layer for all three samples, but tensile testing would highlight the increased tendency for the material to fail through decohesion along the interfacial

layer in the material extruded at a higher temperature (i.e. 550ºC). Microstructural observations will help to substantiate this hypothesis.

The graph below (Figure 4.3) shows the influence of extrusion temperature on the strain to failure and elastic modulus values for the composite. It can be seen that there is minimal variation in the average strain to failure values. The modulus value appears to decrease with increasing extrusion temperature, but this data must be treated with caution due to limitations in the chord modulus technique employed to determine the parameter and the fact that there is a significant overlap in the statistical scatter. Typically for MMCs, the modulus is defined by the rule of mixtures applied to the relative abundance of matrix and reinforcement phases. It is also dependent on the coherency of the interface as adequate load transfer from the matrix to the reinforcement is necessary to reap the full benefits of the inclusion of the high stiffness reinforcement phase. A reduction in modulus with increasing extrusion temperature could be the result of reactions occurring at the matrix/reinforcement interface, but such behaviour has previously been observed in the composite at temperatures closer to 600ºC (73). If the increase in stress with increasing plastic strain during extrusion at 550ºC is related to a reduction in billet temperature then it is unlikely that the billet will experience temperatures exceeding 550ºC during secondary processing.

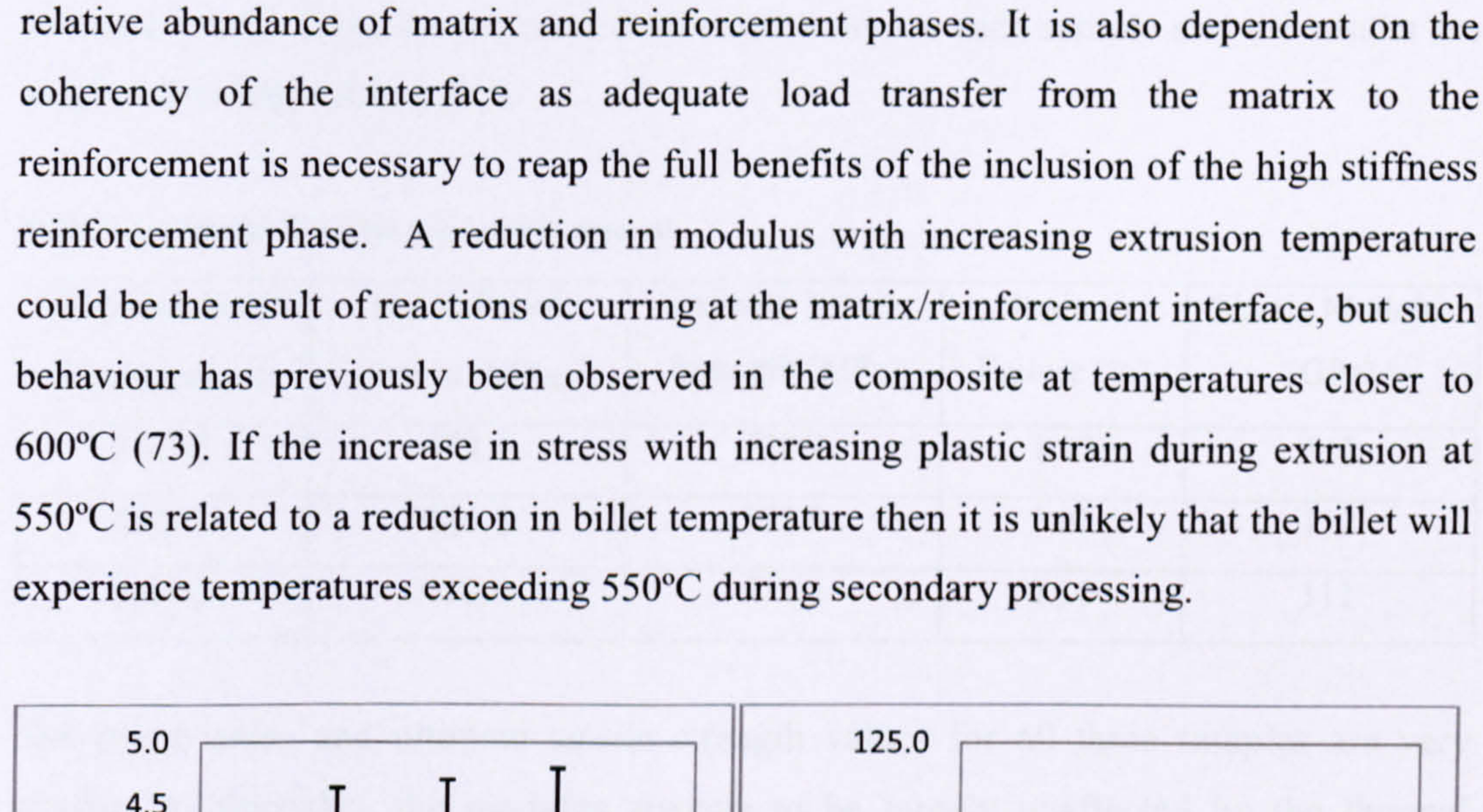


Figure 4.3 - The influence of extrusion temperature on strain to failure and elastic modulus

A further investigation was conducted in order to establish whether the variations in tensile strength could be attributed entirely to the influence of thermal exposure on the microstructure during extrusion and not the deformation processes. An experiment was set up to simulate the thermal conditions of the extrusion work using a controlled temperature furnace. Three samples of AMC225xe machined from as-HIP'ed billet were placed in separate furnaces, which had been preheated to 350°C, 450°C and 550°C, respectively. Following stabilisation, the samples were held at temperature for two hours (equivalent to the preheat time for the extrusion work). The samples were then allowed to air cool (similar to the extruded bars). After returning to room temperature, each sample was solution heat treated, cold water quenched and naturally aged for one hundred hours. Three tensile tests were carried out on each sample and the results are displayed in Table 4.2, below.

Table 4.2 - Tensile values for pre-soaked material

Thermal Soak Temperature	0.2% Proof Stress (MPa)	Ultimate Tensile Strength (MPa)	Strain to Failure (%)	Elastic Modulus (GPa)
350°C	473.1	578.3	1.92	112
450°C	466.5	582.8	2.01	112
550°C	470.4	577.2	2.10	111

The proof stress and ultimate tensile strength values for all three samples are very similar. Additionally, the modulus appears to be largely unaffected by the thermal exposure, even at 550°C (0.98 T_m). This evidence indicates that thermal exposure alone had minimal effect on the microstructure. This in turn suggests that the tensile strength variations observed for the extruded material cannot be entirely attributed to the thermal exposure during secondary processing and the microstructural evolution must occur as a result of the combined effect of temperature and deformation. This would appear to eliminate the theory of the coarsening of intermetallics (e.g. AlSiMn and Mg_2Si) as a likely cause of the reduction in strength at higher processing temperatures, as this phenomenon is likely to be influenced only by temperature through diffusion kinetics and not deformation.

For comparison purposes, another graph is shown below (Figure 4.4) which displays the current tensile data together with data taken from a previously conducted forging experiment at a range of forging temperatures. The tensile test pieces from the forged

material were taken in the forging longitudinal (F-L) direction, away from the dead zone.

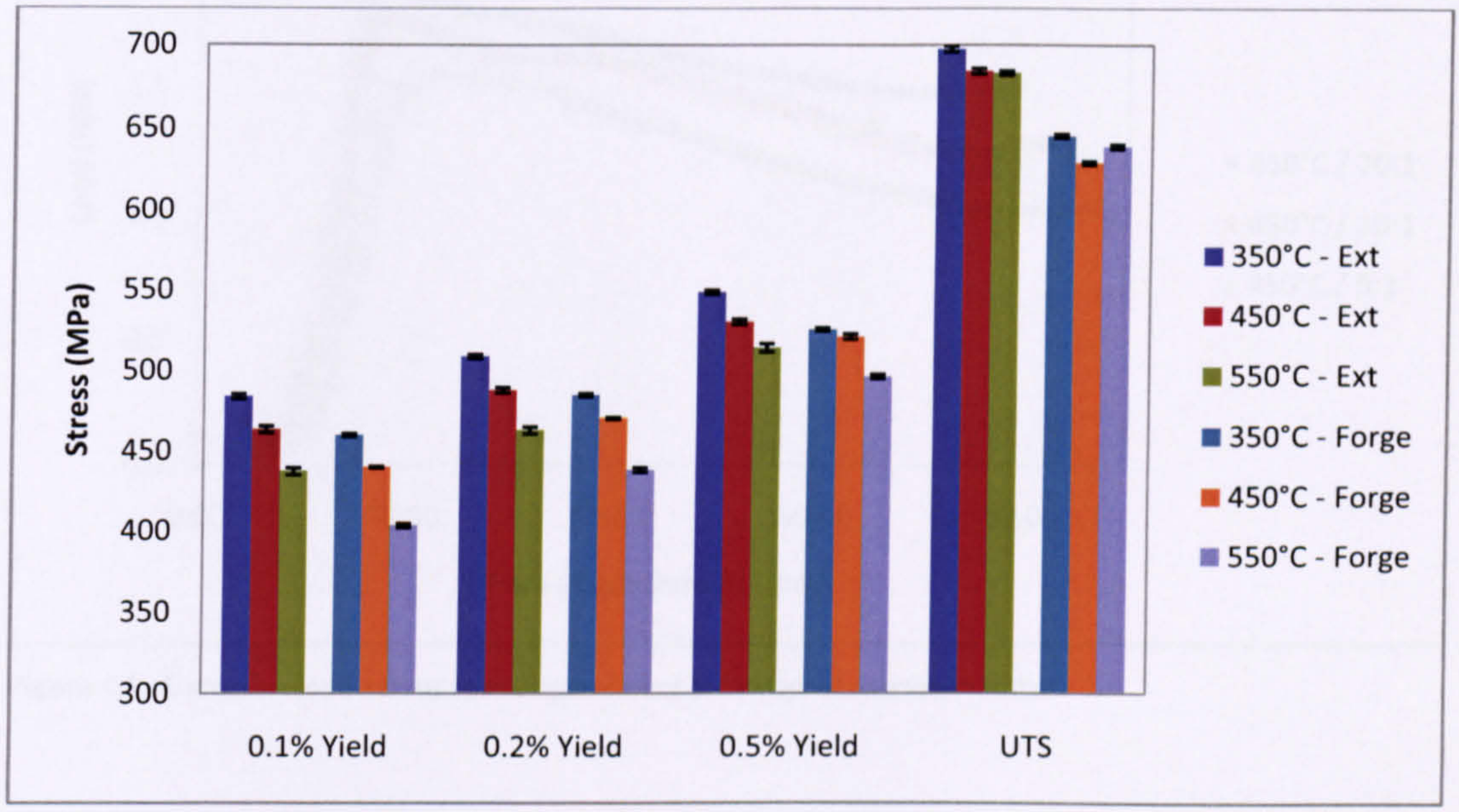


Figure 4.4 - Comparison of tensile properties for material forged or extruded at a range of processing temperatures

The response of the material to the two secondary processing conditions shows good agreement, supporting the validity of the current work. Overall, the values for the extruded material are approximately 4.5% higher than that of the forged material. This is likely to be due to more favourable grain alignment and texture formation in the extruded material, as well as an increase in deformation strain due to the high extrusion ratio.

4.2 The Influence of Extrusion Ratio on Tensile Properties

The second graph of extrusion processing data (Figure 4.5) shows the load versus ram displacement for the billets extruded at three different extrusion ratios. A higher ratio value is associated with a higher peak load as the degree of stress required to achieve plastic flow is increased. The plastic flow behaviour under all three conditions is similar, showing a decreasing load with increasing ram displacement.

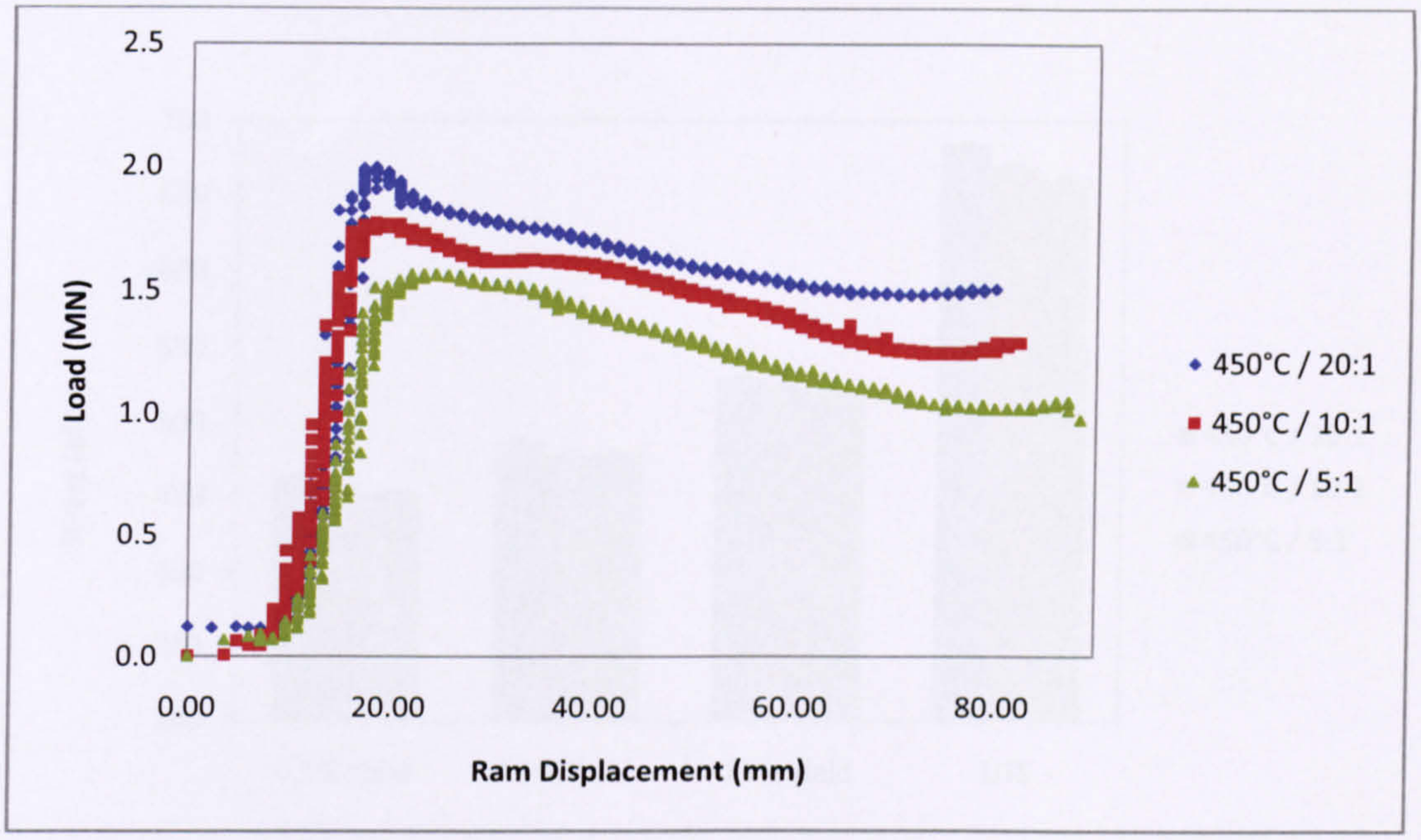


Figure 4.5 - Extrusion load versus ram displacement for range of extrusion ratios

Figure 4.6, below, shows the yield stress and ultimate tensile strength values for the material extruded at the three different extrusion ratios. The graph demonstrates that the higher the extrusion ratio and hence the amount of strain, the higher the yield stress value. The material extruded at a ratio of 20:1 has a 0.2% yield stress value approximately 2% greater than that of the material extruded at a ratio of 5:1. The ultimate tensile strength values vary more significantly, by approximately 3%. The difference in yield stress values may be attributed to the increase in rate of dislocation generation compared to the rate of recovery for the material extruded at the higher ratio, giving increased resistance to plastic flow through dislocation entanglement. Grain alignment and texture effects may also influence the yield stress values.

BUBL
LONDON
UNIV.

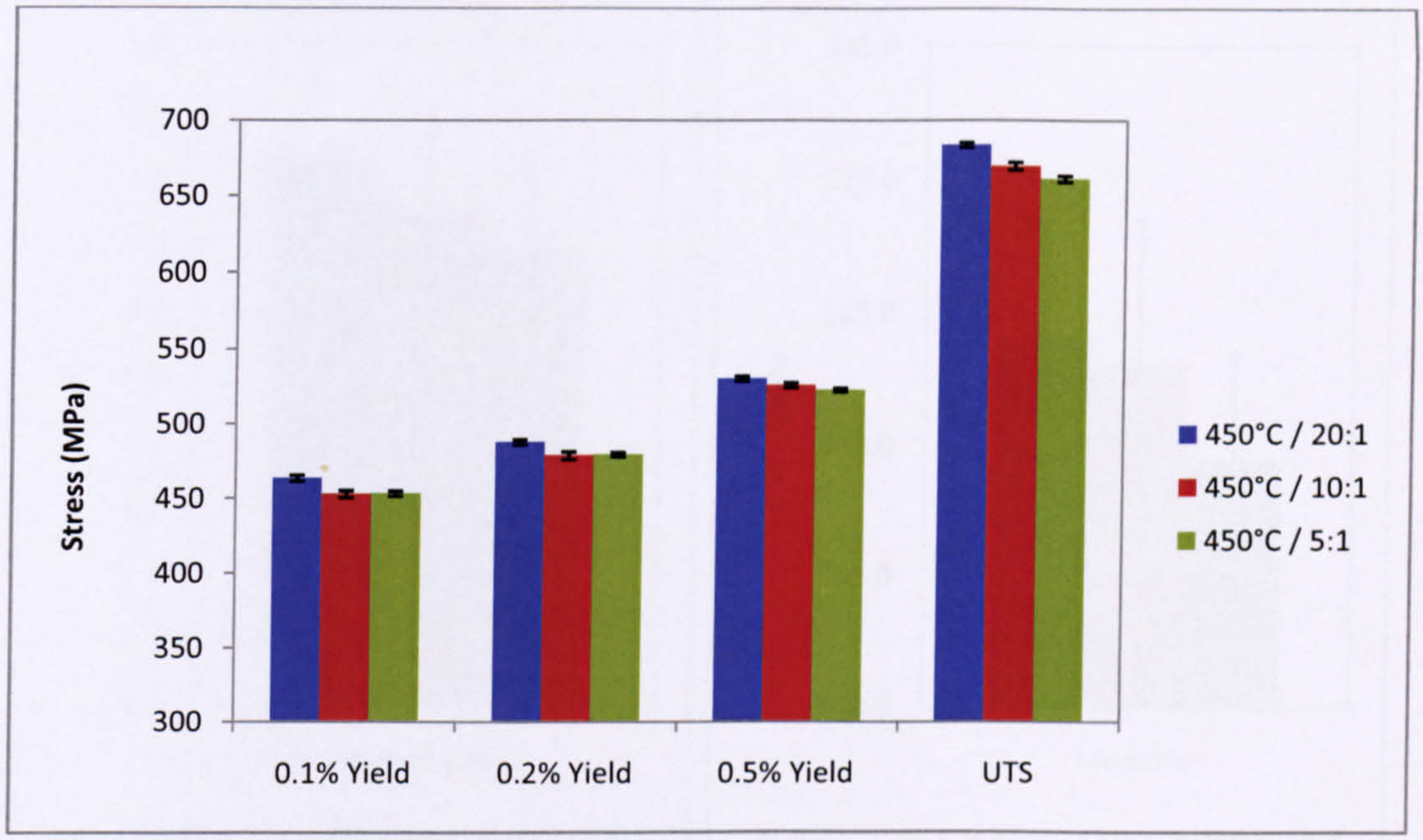


Figure 4.6 - Influence of extrusion ratio on tensile properties of composite

The following graphs (Figure 4.7) show the dependency of strain to failure and elastic modulus on the extrusion ratio. The graphs would suggest a reduction in ductility and elastic modulus with decreasing extrusion ratio, although there is significant overlap in the statistical scatter. Incomplete consolidation during processing has been ruled out as a likely cause as the combination of the HIP process followed by extrusion entirely eliminates the possibility of remnant porosity, as was demonstrated by routine density checking on the billet. The orientation of the specimens could be more significant, as they were machined from a larger cross section of material, increasing the likelihood of producing an 'off-axis' sample. It has been demonstrated that AMC225xe exhibits anisotropic properties following secondary processing, much like conventional aluminium alloys (34).

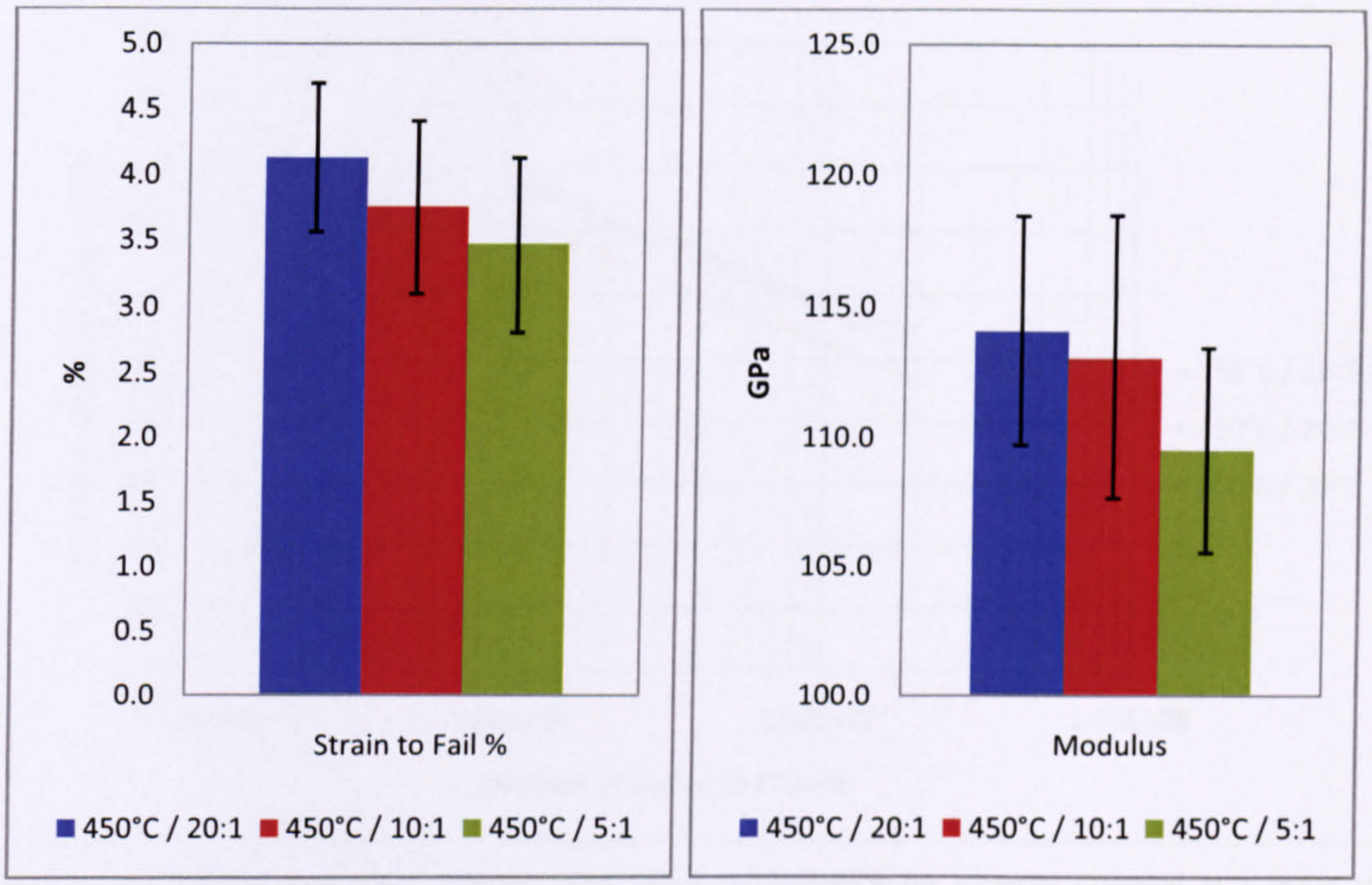


Figure 4.7 - Influence of extrusion temperature on elastic modulus and strain to failure

4.3 Fatigue Testing

The following graph (Figure 4.8) shows the results of the rotating bend fatigue tests carried out on the material extruded at various extrusion temperatures. It can be seen that there is minimal difference between the curves for the materials extruded at 350ºC and 450ºC. For the specimens taken from the bar extruded at 550ºC, there appears to be a more significant reduction in fatigue performance. This behaviour appears to correlate well with the static strength data for the three extrusion condition, again indicating that higher processing temperatures have a detrimental effect on the mechanical properties of the MMC.

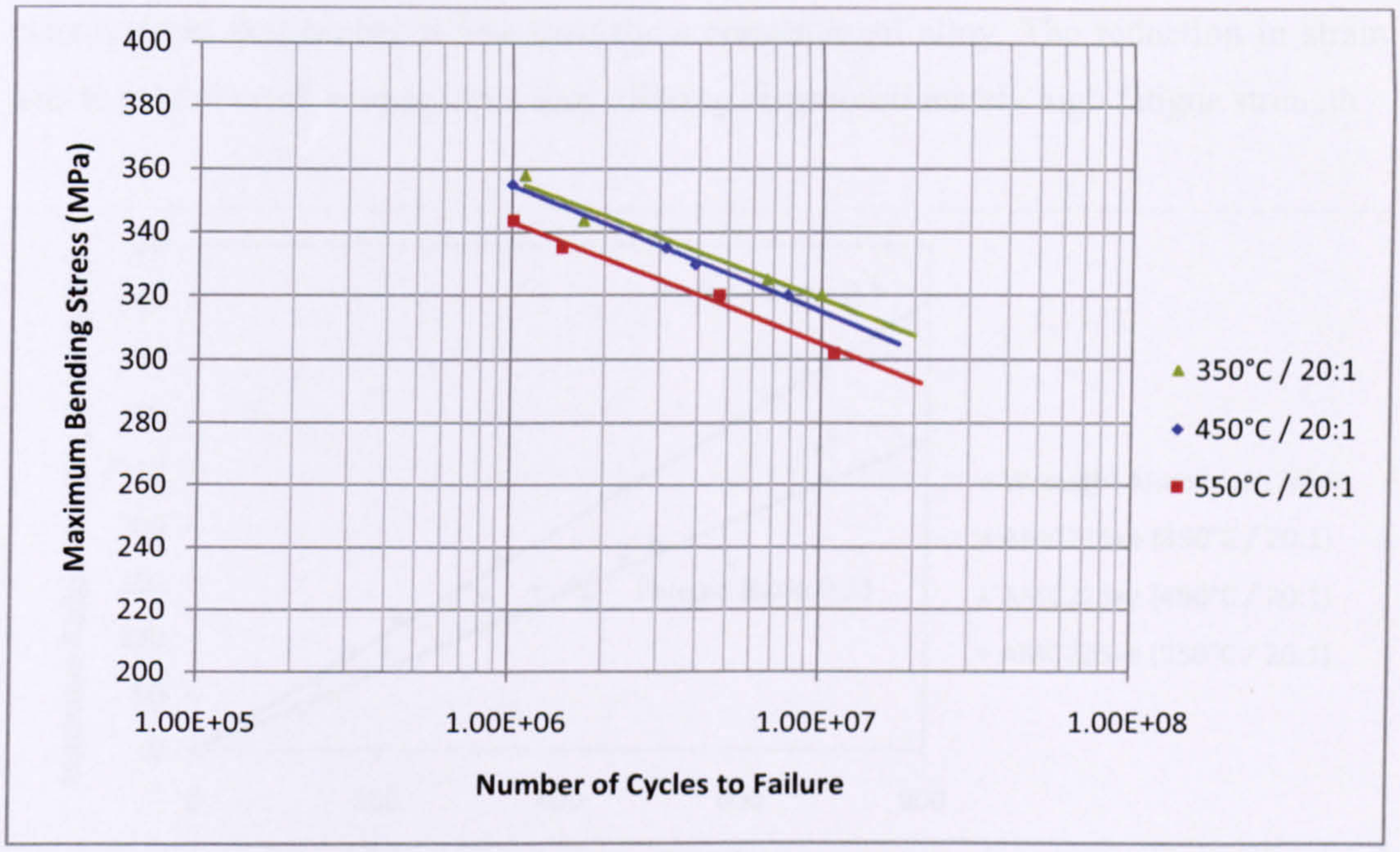


Figure 4.8 - Room temperature rotating bend fatigue performance for material extruded at a range of extrusion temperatures

A common procedure that is used to compare the fatigue resistance of a range of materials is to plot the unnotched, fully reversed fatigue limit versus the ultimate tensile strength of a material. The relationship between these two material properties is known as the "Fatigue Ratio" (98). For steels, the value of the Fatigue Ratio ranges between 0.35 and 0.6. For conventional wrought aluminium alloys, the value ranges between 0.35 and 0.5, as demonstrated in Figure 4.9, which has been adapted from the literature (98). As can be seen, the relationship is non-linear and for higher strength alloys (>450 MPa) the fatigue stress does not increase proportionally with tensile strength. In this case, the fatigue limit for aluminium alloys has been defined as the failure stress at 10^8 cycles, so it was necessary to extrapolate the curves for AMC225xe. For the MMC in all three extrusion temperature conditions a Fatigue Ratio of approximately 0.40 was achieved, which sits comfortably in the typical range for aluminium alloys, however, is considered relatively high for a "high strength" aluminium alloy.

This observation may be attributed to the increased stiffness of the MMC. For the majority of conventional aluminium alloys, the elastic modulus tends to be in the range of 70 GPa to 80 GPa, with some notable exceptions, such as hyper-eutectic Al-Si alloys. The modulus of the MMC is approximately 50% greater than that of the matrix alloy. This means that during the rotating bend fatigue test, for a given bending stress, the

elastic strain that occurs is less than for a conventional alloy. The reduction in strain acts to inhibit crack propagation, thus offering disproportionately high fatigue strength.

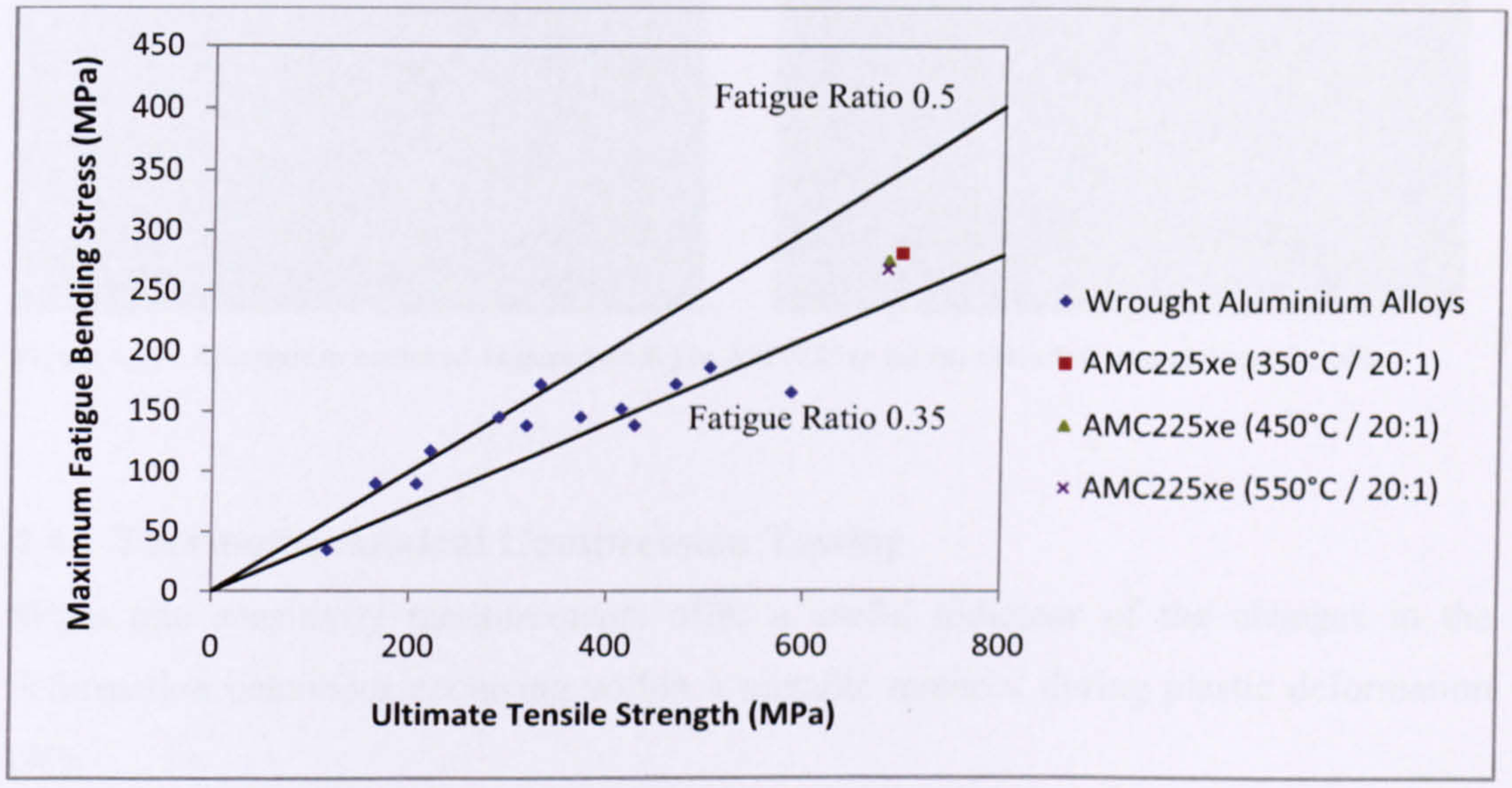


Figure 4.9 - Comparison of fatigue ratios for conventional aluminium alloys and AMC225xe (19)

As well as conventional microstructural features found in monolithic aluminium alloys, AMC225xe is also known to exhibit aluminium-enriched regions within the microstructure. These regions are a by-product of the mechanical alloying process, where a "perfect" distribution of SiC in the matrix does not occur. By altering the manufacturing parameters, it is possible to remove these features from the microstructure entirely. The economics of the process must be considered and the current parameters are defined to limit the volume percentage of these features to a level which has been shown to have minimal detrimental effect on the mechanical properties of the MMC. During the extrusion process, these regions become aligned into stringers with high aspect-ratios (see Figure 4.10). A greater level of strain leads to an increase in the aspect ratio of the feature. If these features are located at the specimen surface they may act as potential sites for fatigue crack initiation and thus cause premature failure. At lower extrusion ratios, the likelihood for these features to be located on the surface of a specimen increases, as their aspect ratio is reduced. This may have a bearing on the variation in fatigue performance of the MMC with respect to product form and test orientation.

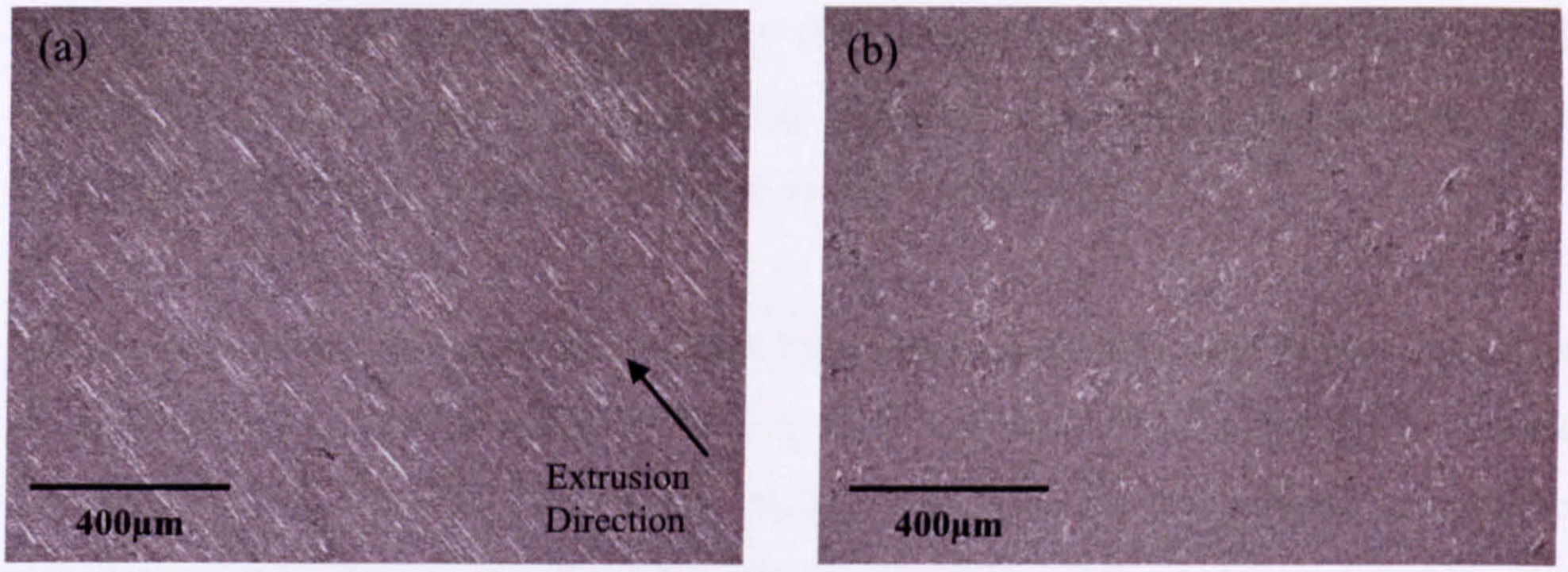


Figure 4.10 - Aluminium-enriched regions (white) in AMC225xe for (a) extruded material and (b) billet

4.4 Thermomechanical Compression Testing

Strain rate sensitivity measurements offer a useful indicator of the changes in the deformation behaviour occurring within a metallic material during plastic deformation (99).

The relationship between compressive flow stress and temperature can be expressed through the Norton-Hoff equation.

$$\sigma = \sqrt{3^{(m+1)}} k \dot{\varepsilon}^m . \exp\left(\frac{\beta}{T}\right)$$

Equation 4.4

σ – compressive flow stress

m – strain rate sensitivity index

k – constant

$\dot{\varepsilon}$ – strain rate

β – constant

T – temperature (K)

The equation can be simplified to the following expression:

$$\sigma = k \dot{\varepsilon}^m . \exp\left(\frac{\beta}{T}\right)$$

Equation 4.5

According to Equation 4.5, the value of the strain rate sensitivity index, m, can be approximated by plotting the natural log of strain rate versus the natural log of compressive flow stress, where "m" is the gradient of the line.

Compression tests were carried out in the temperature and strain rate ranges from room temperature up to 500°C and from 10^{-4} to 1 s^{-1}, respectively. For testing at elevated temperatures, the samples were heated using a split tube furnace and the temperature stabilisation time was 6 minutes. One sample was tested per condition. Samples were machined from a 68 mm diameter as-HIP'ed billet. The gauge section of each sample was a cylinder with a length (L) of 10 mm, and a radius (R) of 4 mm.

The room temperature dependency of compressive flow stress on strain rate is shown in Figure 4.11.

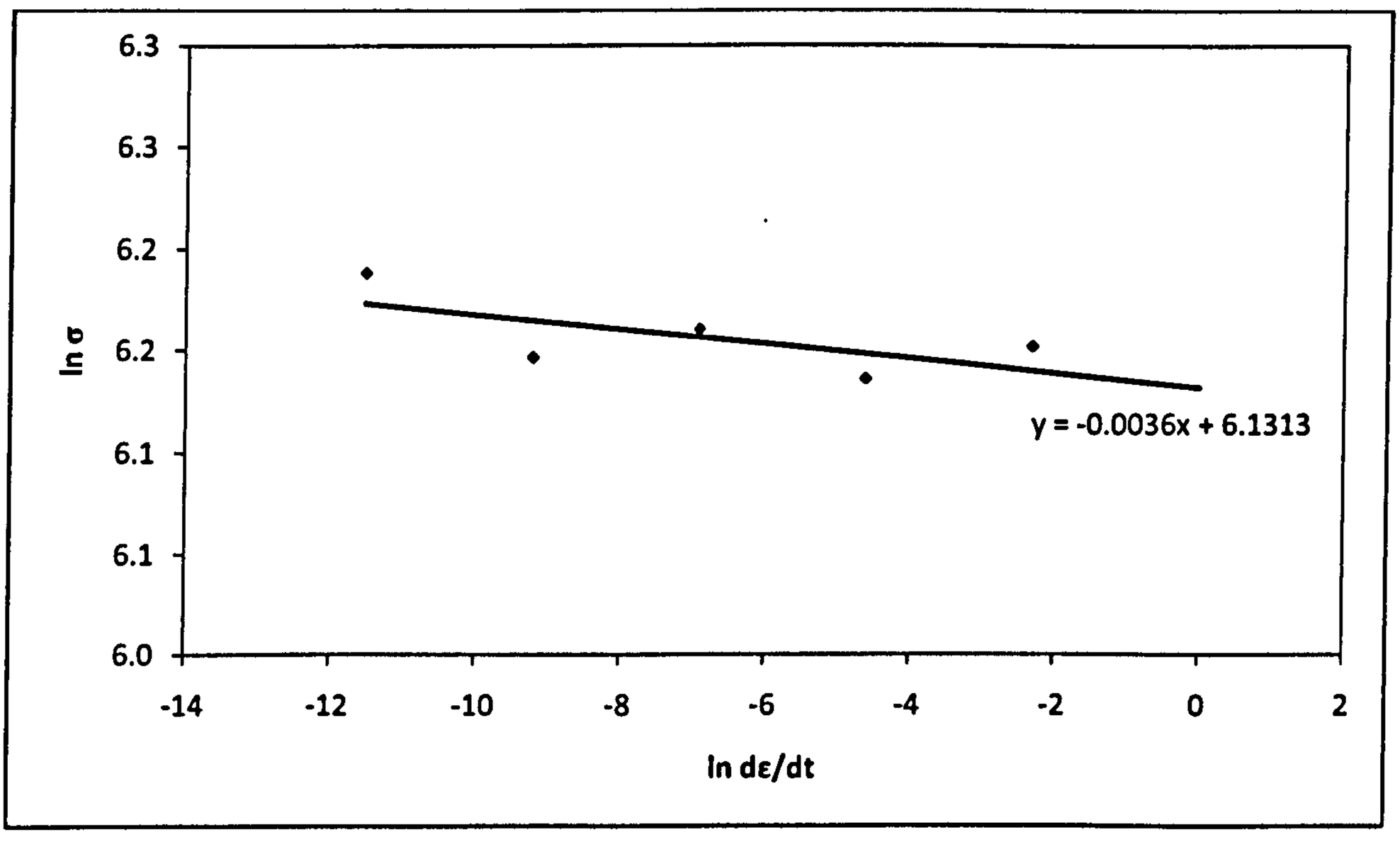


Figure 4.11- Strain rate sensitivity of AMC225xe at room temperature

As for conventional aluminium alloys, the MMC shows a very low strain rate sensitivity at room temperature. Typically, the value of the strain rate sensitivity index, "m," for an unreinforced aluminium alloy is < 0.1 (19). In the case of the MMC there is a slight downwards trend in flow stress with increasing strain rates, causing the value of "m" to be negative. This result has been verified through repetition of the experiment under the same conditions. A possible explanation is an adiabatic heating effect, offering more

energy for recovery mechanisms at high strain rates, although the limited duration of the test is likely to be insufficient for a significant temperature rise to occur. This behaviour has also been previously reported for dispersion strengthened aluminium alloys (100). It was postulated that a material with a negative strain rate sensitivity stores power during deformation, which is later dissipated through a temperature rise.

On completion of the elevated temperature compression testing work it was clear that conventional techniques for determining the compressive flow stress would not be valid for the material under investigation. This is because the material very rarely exhibits a steady state stress during deformation to high plastic strains for a range of temperatures and strain rates. The offset strain at which the compressive flow stress is measured will therefore have a marked effect on the value achieved. This effect is demonstrated in Figure 4.12 and Figure 4.13. At a deformation temperature of 350°C, the flow stress measured at 0.2% strain is approximately 129 MPa. If the flow stress is measured at 0.6% strain, this value would decrease to 119 MPa. Conversely, at 500°C the flow stress increases from 16 MPa to 18 MPa for the given strains. To mitigate any ambiguity, the flow stress value was measured and reported at a range of values for true strain for each test condition.

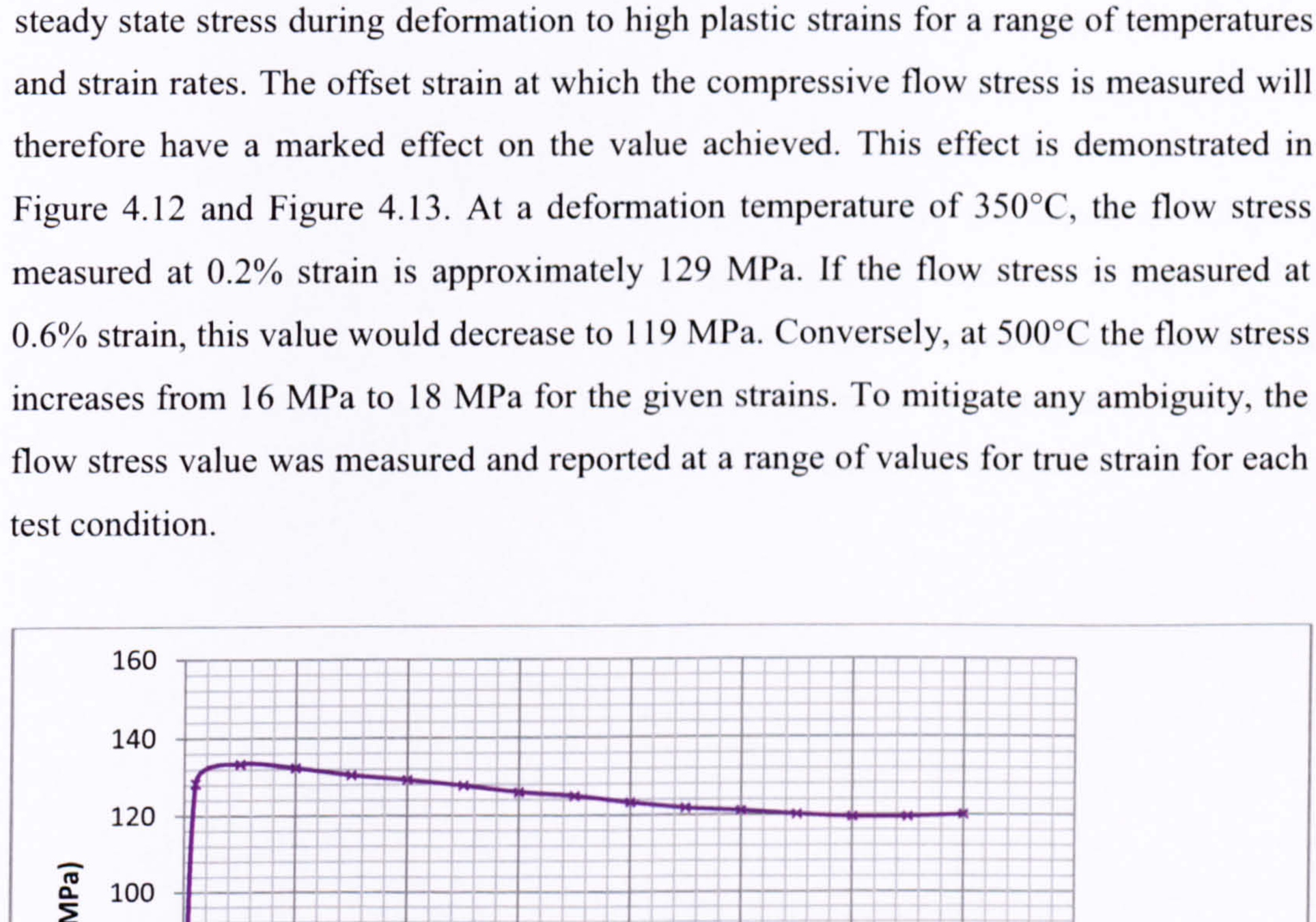


Figure 4.12 – True stress-strain curves at various temperatures performed at a strain rate of 0.1 /s

It can be seen in Figure 4.12 that at the lowest temperature, 350°C, the material exhibits strain softening behaviour. At 400°C the material plastically deforms at an approximately constant stress. Above 400°C the material exhibits strain hardening behaviour and the strain hardening exponent increases with increasing temperature. This behaviour is contrary to conventional metallic alloys, where at lower temperatures, strain hardening is usually apparent but at high temperatures ($T_m > 0.5$) strain softening is observed.

Figure 4.13 shows the response of AMC225xe to an applied compressive stress across a range of strain rates at 450°C. The results suggest that at lower strain rates, the flow stress gradually increases as the degree of strain increases. At this temperature it is postulated that the rate of dynamic recovery is likely to exceed the rate of dynamic recrystallisation. The accumulation of dislocations and the generation of subgrain boundaries offer resistance to further dislocation motion and contribute to a progressive increase in the compressive stress. At high strain rates, the prevailing deformation mechanism is likely to be dynamic recrystallisation and so the material exhibits flow softening behaviour with increasing strain due to a reduction in dislocation density over the test duration.

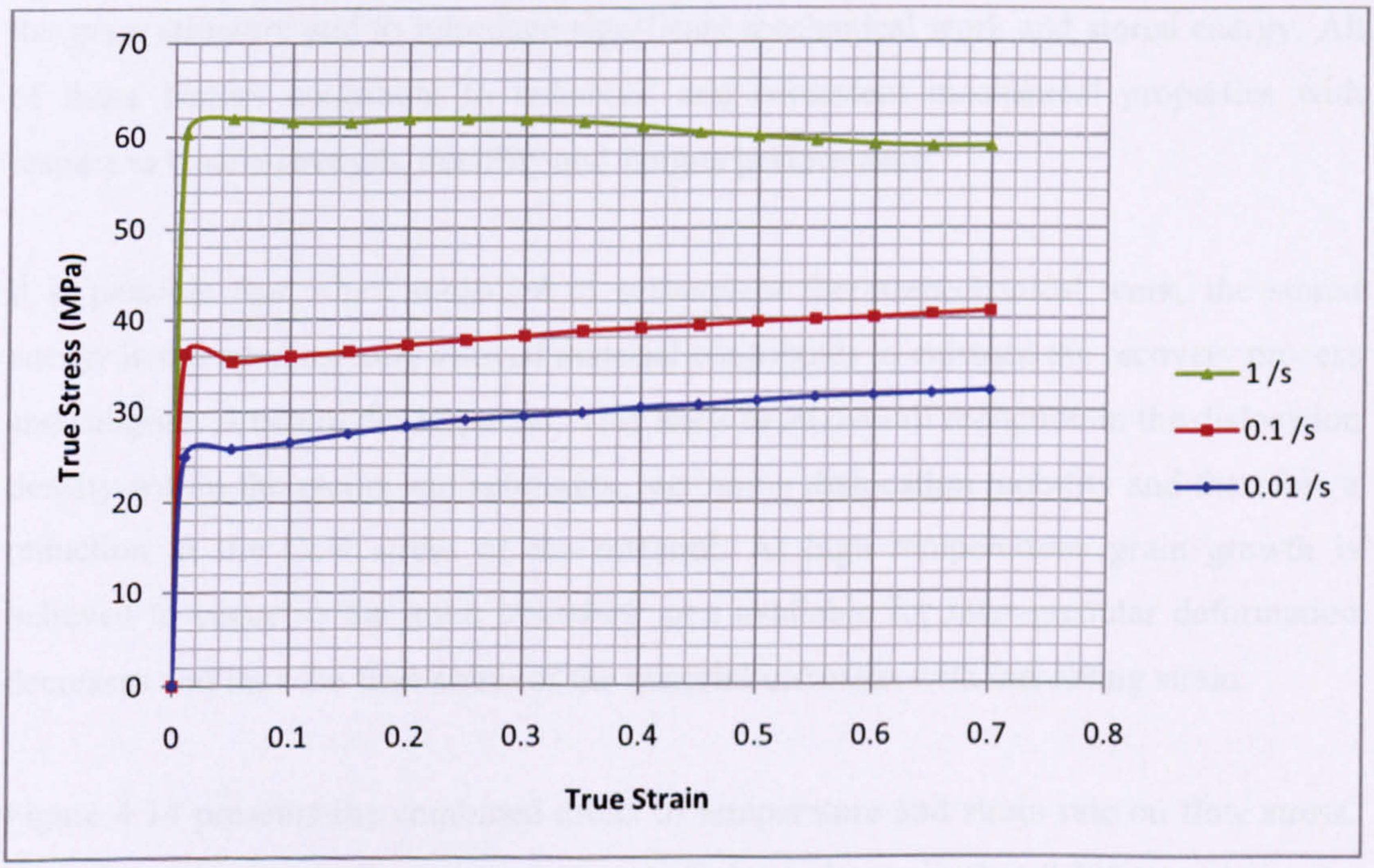


Figure 4.13 - True stress-strain curves at various strain rates performed at a temperature of 450°C

In previous studies on Al-Fe-V-Si elevated temperature alloys a similar thermomechanical response has been observed (95). Two alloys were manufactured with the same chemical composition. One of the materials was mechanically alloyed, through an identical route to that employed within the current study. The other material was not subjected to the mechanical alloying process and the as-atomised powder was directly consolidated. It was discovered that the mechanically alloyed material exhibited a decrease in the deformation stress with increasing strain at low temperatures and an increase in the deformation stress with increasing strain at high temperatures. This behaviour is consistent with that of the material involved in the current study. Conversely, for the material that was not mechanically alloyed prior to consolidation, the opposite behaviour was observed, which is more consistent with conventional aluminium alloys. It is therefore postulated that the primary contributing factor to this counter-intuitive thermomechanical response is the inclusion of the mechanical alloying process and not the presence of the reinforcement phase in the MMC. This theory is also supported by other studies on MMCs manufactured without the mechanical alloying process, which have shown the more conventional deformation response (40).

The mechanical alloying stage is included in the manufacturing process for a variety of reasons: to improve the distribution of the reinforcement phase in the MMC, to refine the grain structure and to introduce significant mechanical work and stored energy. All of these factors contribute to enhanced and consistent mechanical properties with respect to tensile strength, ductility and fatigue performance.

It is possible that when subjected to subsequent thermomechanical work, the stored energy in the mechanically alloyed material contributes to enhance the recovery process and subgrain structure development. This leads to an overall reduction in the dislocation density within the grains and subgrains, increasing dislocation mobility and therefore a reduction in the flow stress of the material. At high temperatures grain growth is believed to occur so the grain boundary area available for inter-granular deformation decreases and thus the flow stress of the material increases with increasing strain.

Figure 4.14 presents the combined effect of temperature and strain rate on flow stress. Here the compressive flow stress values have been determined at 0.1% true strain. As was predicted, flow stress increased with decreasing temperature and increasing strain rate.

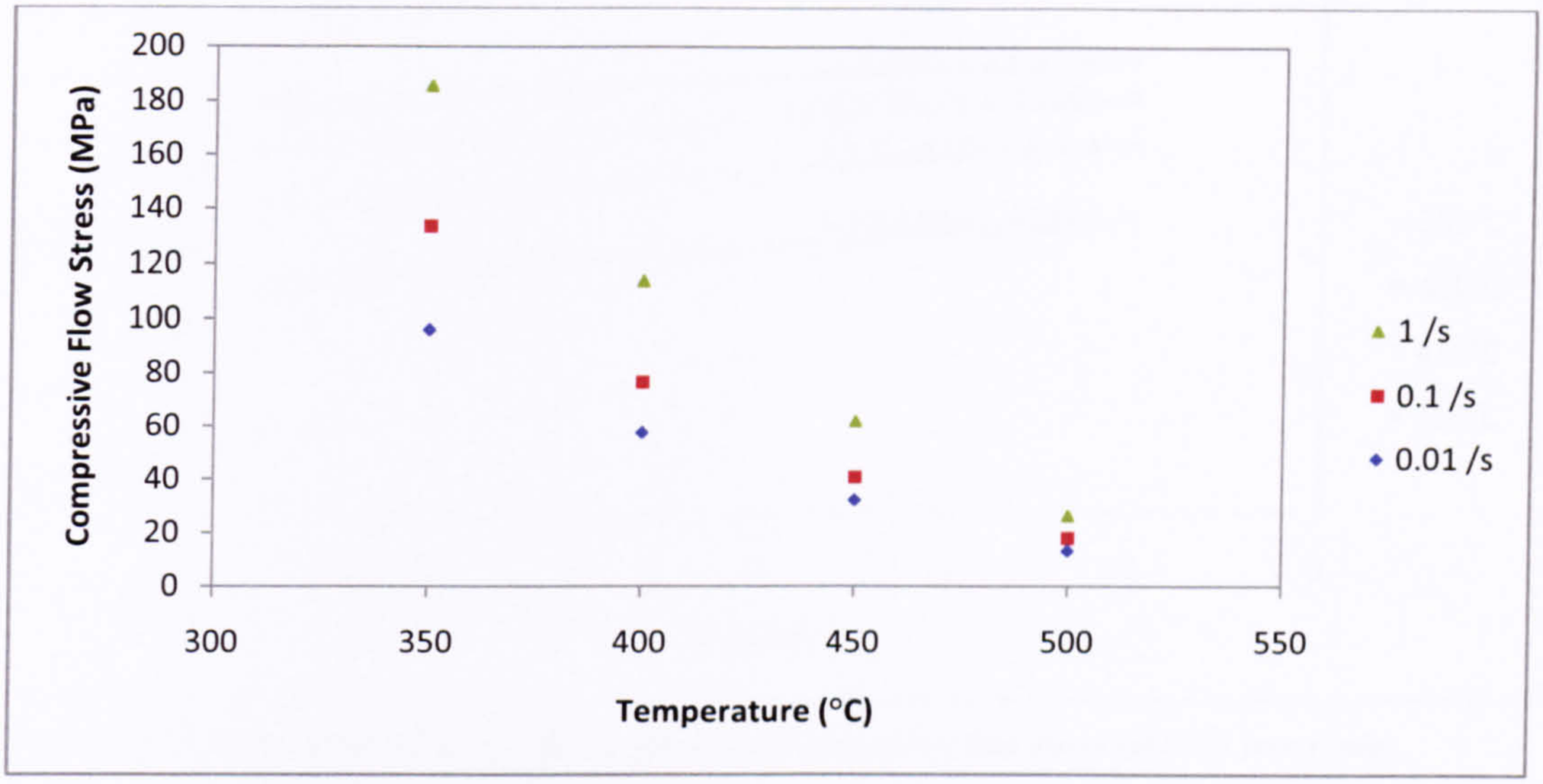


Figure 4.14 - Temperature and strain rate dependence of compressive flow stress (at 0.1% true strain)

Table 4.3 - Temperature and strain rate dependence of compressive flow stress (at 0.5% true strain)

	Temperature (°C)				
Strain Rate	**23**	**350**	**400**	**450**	**500**
0.0001 /s	487	-	-	-	-
0.001 /s	467	-	-	-	-
0.01 /s	474	94	56	31	13
0.1 /s	462	121	73	40	17
1 /s	470	148	99	60	26

The data in Table 4.3 also demonstrate that the flow stress of AMC225xe decreased with increasing temperature and decreasing strain rate. Compared to the compressive flow stress values at 0.1% true strain, as shown in Figure 4.14, the change in flow stress with strain rate for a given temperature is reduced at 0.5% true strain. This indicates that at high levels of plastic strain, compressive flow stress becomes less sensitive to changes in temperature and strain rate.

The value of the strain rate sensitivity index, "m" has been calculated for each test temperature by applying the simplified Norton-Hoff equation. From a plot of $\ln d\varepsilon/dt$ versus $\ln \sigma$, the gradient of the curve provides the value of "m," as shown in Figure 4.15.

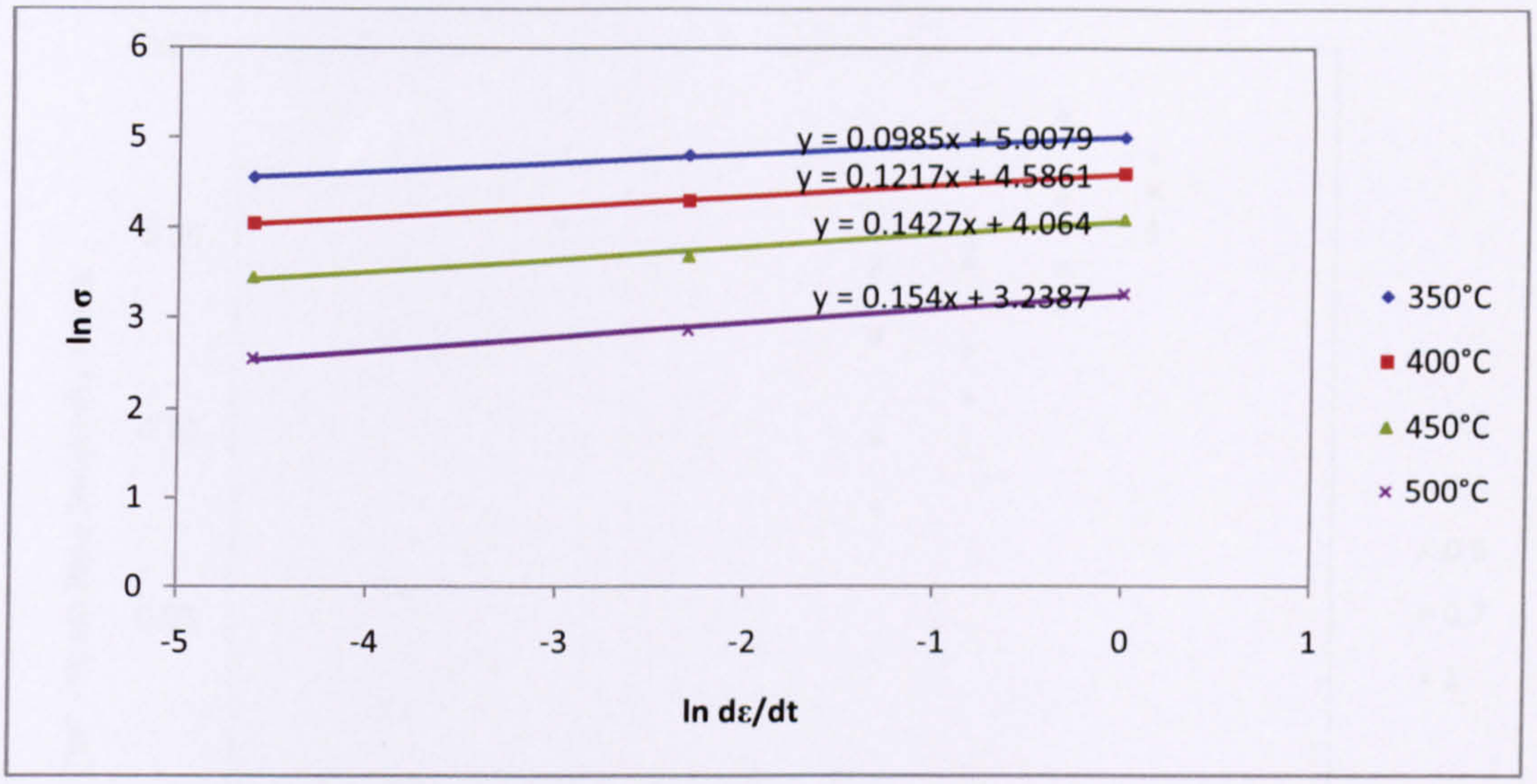


Figure 4.15 - Strain rate and temperature dependence of compressive flow stress (at 0.5% true strain)

The values of "m" have been plotted against test temperature for the entire temperature range in Figure 4.16. The corresponding true strain value at which the compressive flow stress was determined is displayed in the legend. The value of "m" shows a relatively small increase in the temperature range of 350°C up to 500°C. Previous studies have shown that the strain rate sensitivity of a material generally increases as the temperature increases. For aluminium alloys, it has been reported that when the test temperature exceeds half of the absolute melting point, the value of "m" will typically increase to between 0.1 and 0.2 (19). All of the tests in the current work were carried out at $T_m >$ 0.5 and all of the "m" values lie within this range. The strain rate sensitivity does not show a significant increase with increasing temperature, even up to a T_m value of 0.9. At higher temperatures, closer to the melting point, the values achieved are lower than those predicted in the literature for conventional aluminium alloys, typically 0.25 at 500°C (101). Previous studies have suggested that the MMC in the current study would exhibit superplastic behaviour because the material has a highly refined grain structure, which exhibits high thermal stability at elevated temperatures (73). However, the strain rate sensitivity data from the current work suggests that this may not in fact be the case, as typically a strain rate sensitivity index of 0.5 or greater would be required to achieve superplastic behaviour, where total plastic strains of up to 1000% may be observed.

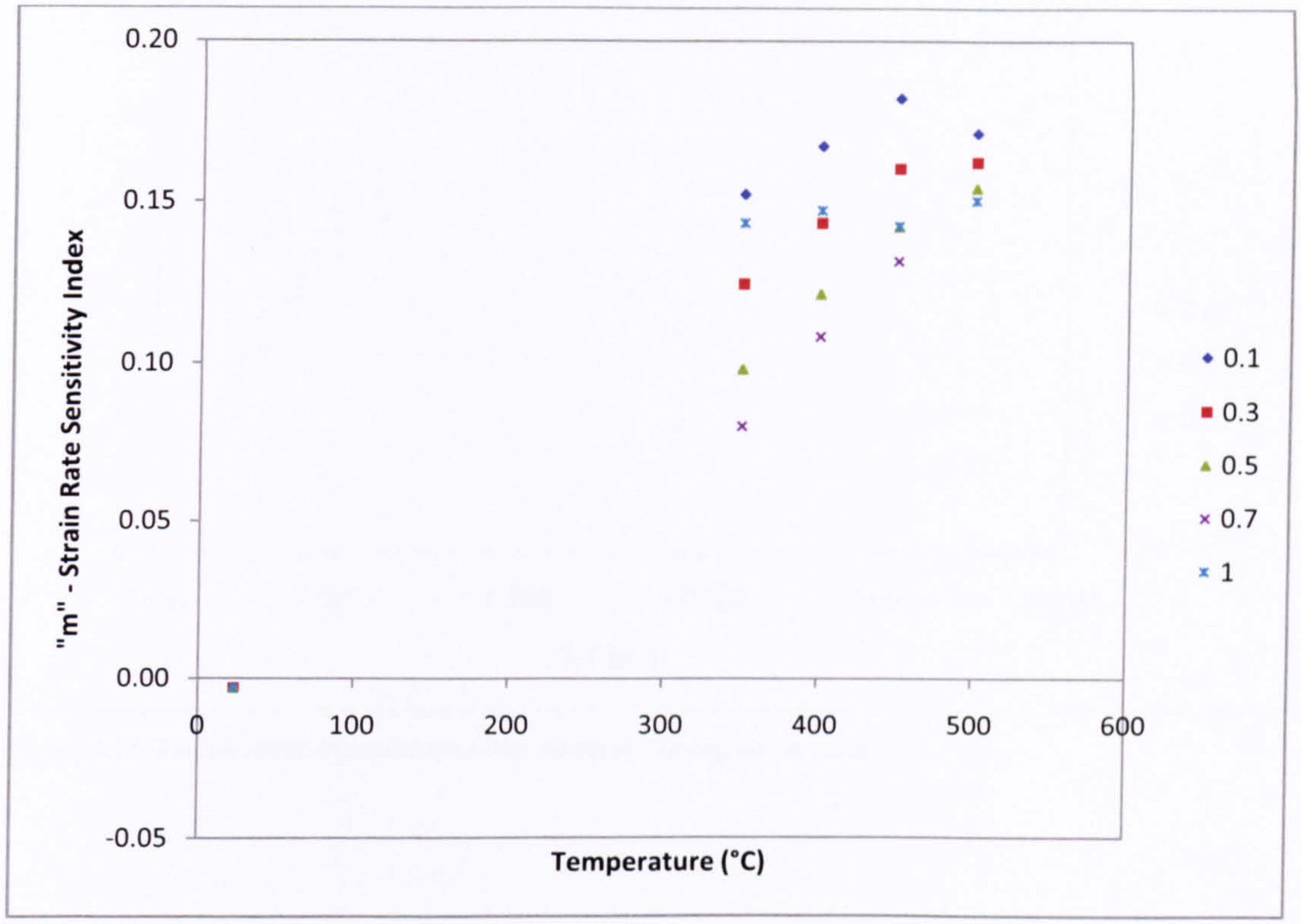


Figure 4.16 - Temperature dependence of strain rate sensitivity index for a range of true strain values

The constant, "β," from the Norton-Hoff equation can be determined by plotting compressive flow stress against test temperature for a given constant strain rate. The value of "β" gives an indication of the activation energy for dislocation motion within the matrix. The chart below (Figure 4.17) shows a non-linear relationship between the reciprocal of temperature and the compressive flow stress of the material for all strain rates. This finding suggests that the equation is an inadequate model of the behaviour. The data indicate that there is a potential change in the steady state deformation mechanism between 350°C and 450°C. This behaviour has also been identified in previous investigations and it has been suggested that it is related to a change in the prevailing plastic deformation mechanism from intra-granular, at low homologous temperatures, to inter-granular, at high homologous temperatures (102). This effect is exaggerated in metallic materials with highly refined and thermally stable grain structures due to the abundance of grain boundaries available for inter-granular deformation at elevated temperatures.

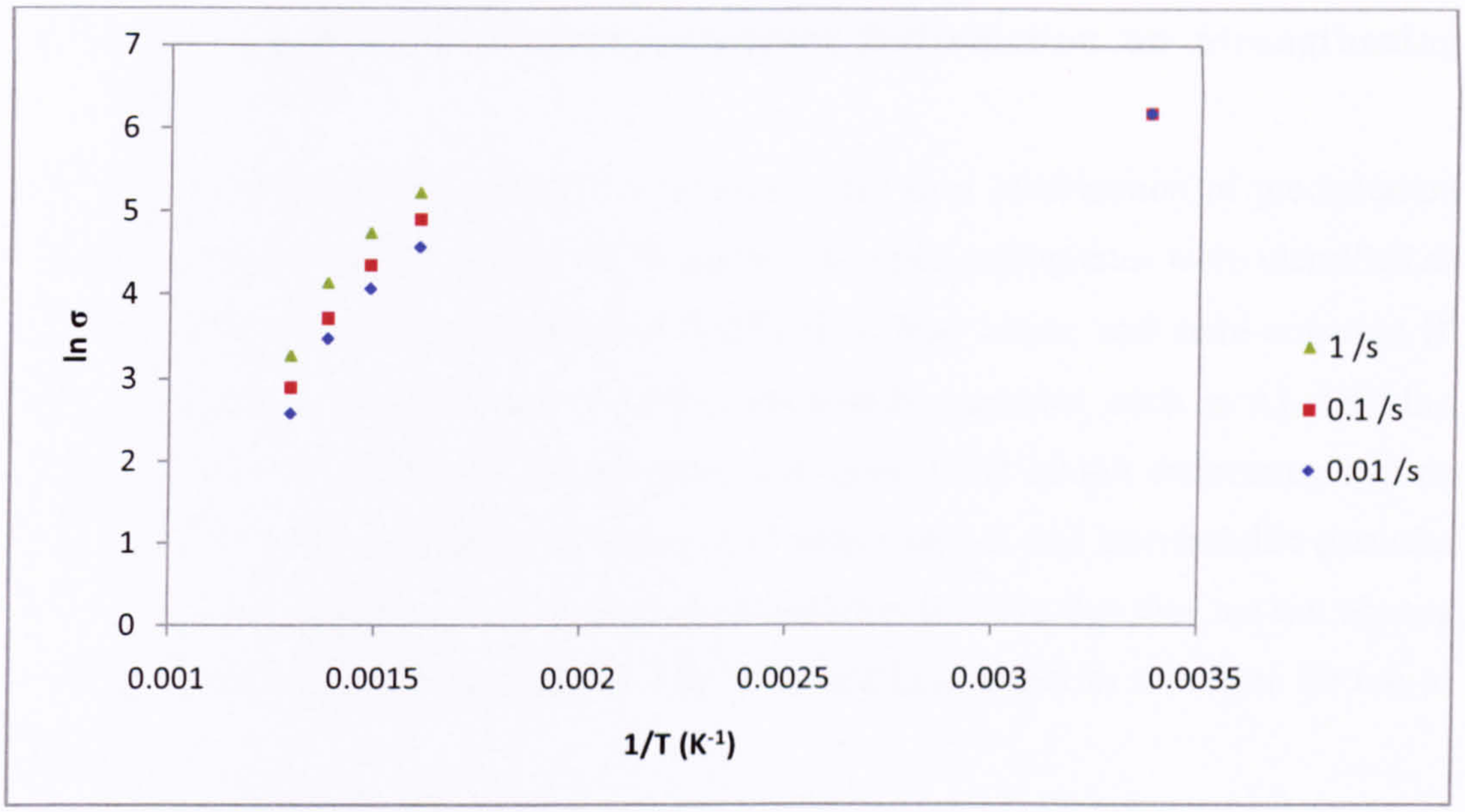


Figure 4.17- Temperature dependence of flow stress at varying strain rates

4.5 The Influence of Thermomechanical Deformation on Strengthening Mechanisms

The strength of the matrix material is primarily due to a combination of precipitation and dispersion hardening. During TEM studies, the main precipitates were identified as coherent Guinier–Preston–Bagaryatskii (GPB) (Cu, Mg) zones, and semi-coherent S' (Al_2CuMg) phase. The presence of stable intermetallic particles, such as $Al_{20}Cu_2Mn_3$, has previously been shown to favour grain size control and inhibit dislocation motion (103). However, the FIB image in Figure 4.18 demonstrates that intermetallic particles also exist within grains, as well as on grain boundaries proving that they are not always effective at pinning grain boundaries. The intermetallics ranged in size from 20 nm to 300 nm.

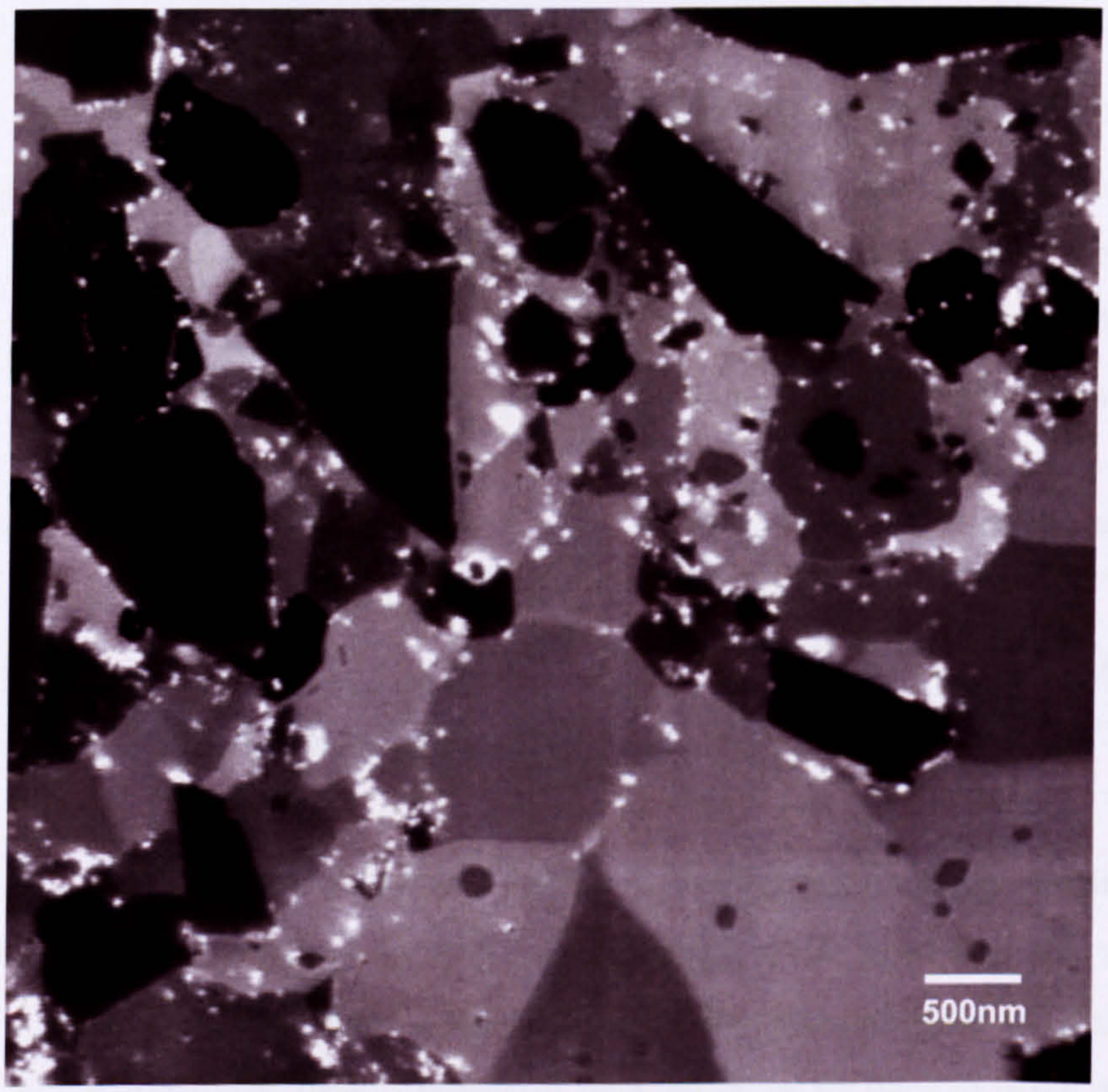


Figure 4.18 – FIB secondary electron image of intermetallic particles within grains (extruded at 350°C / 20:1 / E-T)

It is generally believed that Orowan strengthening, although the primary strengthening mechanism in aluminium alloys, is not significant for MMCs because reinforcement particles are relatively coarse and interparticulate spacing is large (104) (105). The literature predicts that for 25 vol% of 3 μm SiC_p in an aluminium alloy matrix, the

direct Orowan mechanism contribution of the reinforcement to yield stress would be just 9 MPa. As the metallographic assessment demonstrates within this work, the particulate reinforcement is predominantly located at grain boundaries, so whether the SiC offers any direct Orowan strengthening contribution is debatable. Indirectly, its contribution is highly significant due to the generation of dislocations through the mismatch in thermal expansion coefficient between the matrix and the reinforcement, which accelerates the nucleation of strengthening precipitates during ageing.

The Hall-Petch equation related yield stress enhancement through grain refinement to grain size, D.

$$\Delta\sigma_{YM} \approx kD^{-\frac{1}{2}}$$

Equation 4.6

The value of k is dependent on a range of factors but is typically 0.1 MPa√m (50). The strengthening contribution of grain size can therefore be predicted for each material variant. The average grain size data in Table 4.4 are taken from the FIB microstructural analysis work found in Section 4.6: Microstructural Analysis of Aluminium MMC by FIB Imaging. Data scatter is also shown in the table, indicating ±2 standard deviations.

Table 4.4 - Influence of extrusion temperature on grain size and predicted strengthening contributions

Extrusion Temperature (°C)	350	450	550
Average Grain Size, D (μm)	0.66 (±0.04)	0.73 (±0.03)	0.95 (±0.05)
Predicted Strengthening, $\Delta\sigma_{YM}$ (MPa)	123	117	103

As for conventional alloys, a close link between dislocation density and strengthening has been established for MMCs. Arsenault et al. estimated the strengthening effect, assuming that a misfit strain is relaxed by the punching of dislocation loops. The increase in dislocation density, $\Delta\rho$, was predicted by the following equation (104):

$$\Delta\rho = \frac{\Delta\alpha\Delta TNA}{b}$$

Equation 4.7

$\Delta\alpha\Delta T$ is the thermal misfit strain, N the number of particles, b the Burgers vector and A the total surface area of each particle. A simplified case was derived by Miller and Humphreys, assuming cube shaped particles (106):

$$\Delta\rho = 12\frac{\Delta\alpha\Delta T f}{bd}$$

Equation 4.8

where d is particle size. The foundation equation predicts a decrease in dislocation density as reinforcement particles become more spherical.

The influence of dislocation density on matrix yield strength, σ_{YM}, can be predicted through the following relationship:

$$\Delta\sigma_{YM} \sim Gb\sqrt{\rho}$$

Equation 4.9

where G is the shear modulus.

The predicted dependence of this strength contribution on reinforcement size and volume fraction is represented in Figure 4.19. The plots were obtained using the above equations based on a temperature reduction of 100°C.

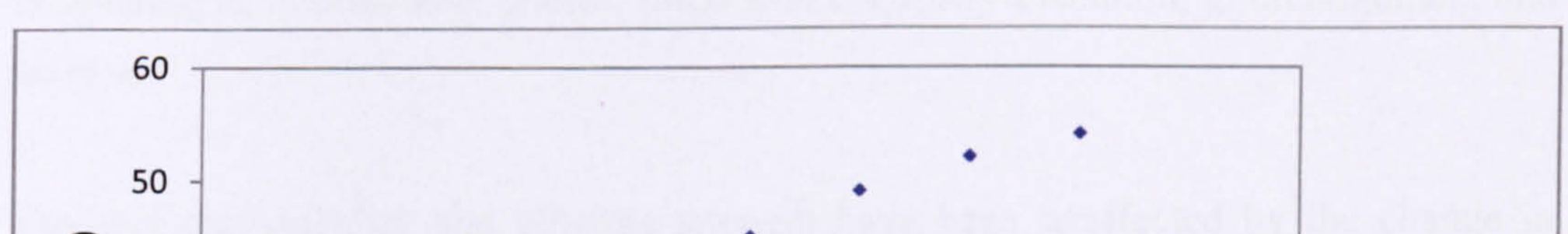


Figure 4.19 - Particle strengthening contribution. Adapted from Clyne and Withers (30).

The model assumes cubic particles, but the first equation demonstrates a reduction in dislocation generation with spherical particles. It can be assumed, therefore, that the

irregular morphology of the reinforcement particles in AMC225xe would give a strength increase less than that predicted in the chart (45 MPa). For a reduction in temperature of 485°C during solution heat treatment, the equations predict a strength increase of approximately 100 MPa (for cubic particles, 3 μm in size).

The substructural change at different extrusion temperatures is evidenced in the FIB images (Figure 4.20 and Figure 4.21). It can be seen that grain size increases with increasing extrusion temperature. This behaviour is typical for most metals (107). Some grain boundary pinning was observed and will be discussed in more detail later on.

Analysis of the mechanical properties for the material extruded at a range of temperatures shows that the yield strength is dependent upon extrusion temperature. The ultimate strength and ductility appear to be largely unaffected. Yield strength deteriorated by 46 MPa for an increase in extrusion temperature of 200°C from 350°C to 550°C. Table 4.4 shows that that this reduction can be partially attributed to the increase in grain size over the same temperature range. This would account for approximately 50% of the discrepancy. The remainder may be attributed to other factors including coarsening of intermetallic phases, interfacial chemistry evolution, grain alignment and texture.

The fact that ductility and ultimate strength have been unaffected by the change in secondary processing temperature indicates that the overriding factor governing failure is the presence of the reinforcement phase in the material. Conventional aluminium alloys usually show an increase in ductility and ultimate strength with increasing grain size due the enhanced accommodation of dislocations within the larger grains. The MMC did not show such a relationship. A possible explanation is that the typical failure mechanism for such materials is reinforcement cracking, although this usually occurs where the reinforcement particles are greater than 20 μm in size (108). As previously described, fracture occurs where the particle contains a sufficiently large flaw, which is more likely for large particles. During the metallographic examination of AMC225xe it was noted that a very small proportion of SiC particles showed signs of crack propagation, so this mechanism is relevant but only to a limited extent.

An example of crack formation within a SiC particle is shown in Figure 4.20. It is of particular interest that particle cracking only appeared to occur in the material extruded

at the lowest temperature, 350°C. This could be indicative of the greater stress concentration build-up during thermomechanical processing due to the relatively high flow stress of the surrounding matrix at this temperature.

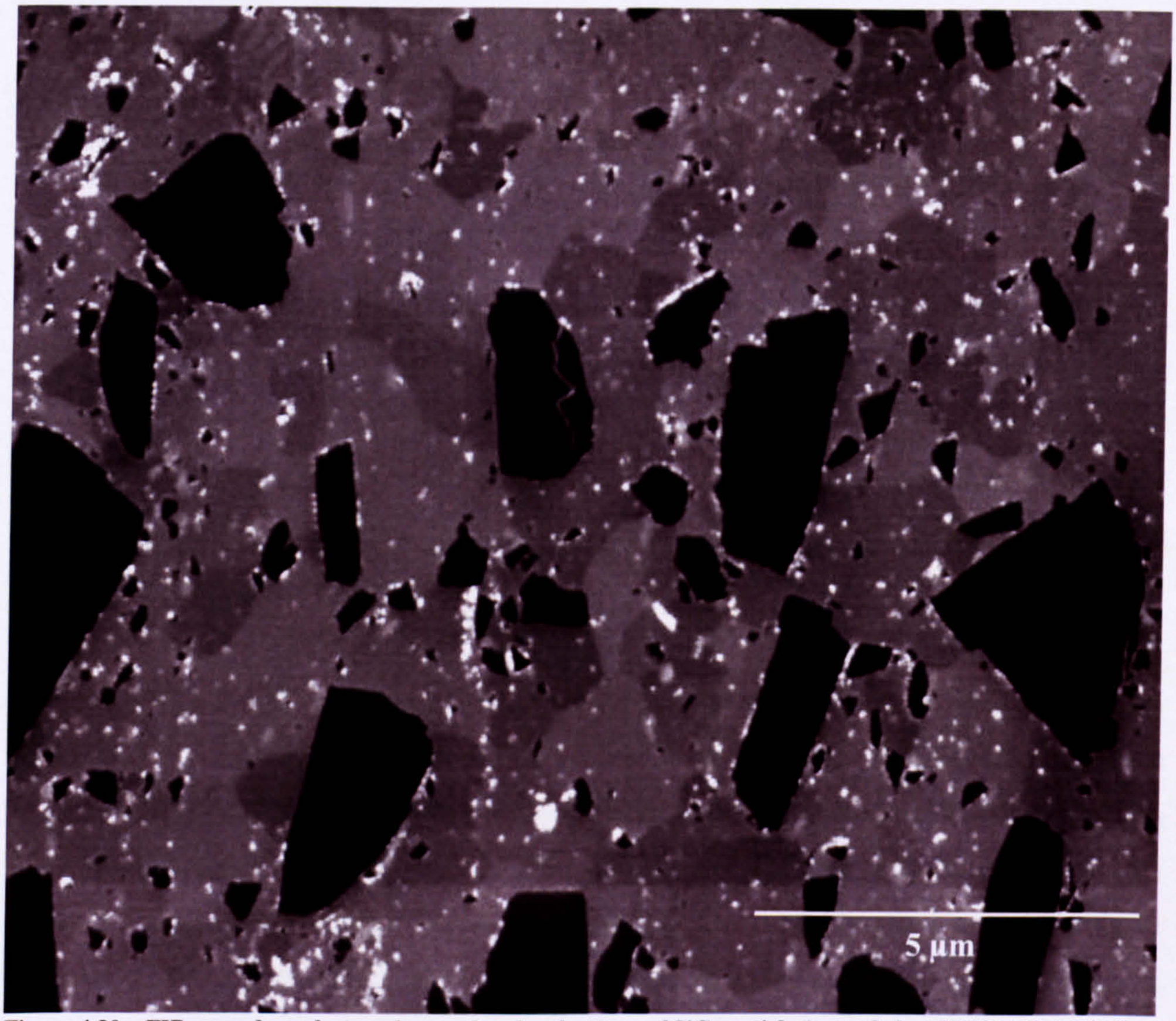


Figure 4.20 – FIB secondary electron image showing fracture of SiC particle (extruded at 350°C / 20:1 / E-T)

For particulate MMCs reinforced with finer particles, failure is usually dictated by the nucleation of cavities within the matrix and interfacial debonding. Cavities often form close to the interface region due to increased work hardening within these regions. This is a result of the mismatch in thermal expansion coefficients of the matrix and reinforcement and also a localisation of the applied plastic strain. The current metallographic assessment shows little evidence of brittle interface phases in AMC225xe, suggesting that nucleation is most likely to occur within the matrix. This is usually the case for MMCs with strongly bonded interfaces.

Raj carried out a development of the Frost and Ashby processing map to cater for metal matrix composites (109) (110). He defined two distinct damage mechanisms in an

AA6061 aluminium alloy reinforced with different levels of SiC particles. The first mechanism was cavity nucleation at the interface between the ductile matrix and hard particles. The second was wedge cracking at triple grain boundary points. Cavitation, which results in ductile fracture, was found to occur at high strain rates and low homologous temperatures. At high temperatures, the rate of void formation decreases due to the lower work hardening rate and the effect of recovery. At low strain rates, diffusion promotes stress relief at the particle interfaces.

Grain Structure

During extrusion dislocation generation occurs readily through pile up at interfaces, CTE mismatch induced strains and Orowan looping around oxide particles and other dispersoids. The presence of fine oxide particles, as observed during the metallographic assessment, has a significant influence on the nature of the grain and subgrain structure in a powder metallurgy MMC. Such oxide particles are particularly effective at pinning grain and subgrain boundaries.

The dislocation density surrounding a reinforcement particle is significantly higher than that found in the matrix as a whole. Through recovery processes in the proximity of the particles, the stored energy can be reduced by the removal of point defects and through dislocation structure rearrangement to form subgrain boundaries (30). Aluminium has a high stacking fault energy so dislocation rearrangement is highly prevalent, particularly in the proximity of reinforcement particles, leading to a fine subgrain microstructure in these regions. The process of subgrain refinement is counteracted by grain growth. Grain growth can be observed more readily in localised regions where reinforcement content is relatively low and interparticulate spacing is high. Within these regions, the particles do not constrain the movement of grain boundaries and so coarsening can occur. This effect can be observed in Figure 4.21, where the average grain size is approximately 0.7 μm in the regions of high reinforcement density (A) but increases up to 5 μm in regions where interparticulate spacing is high (B).

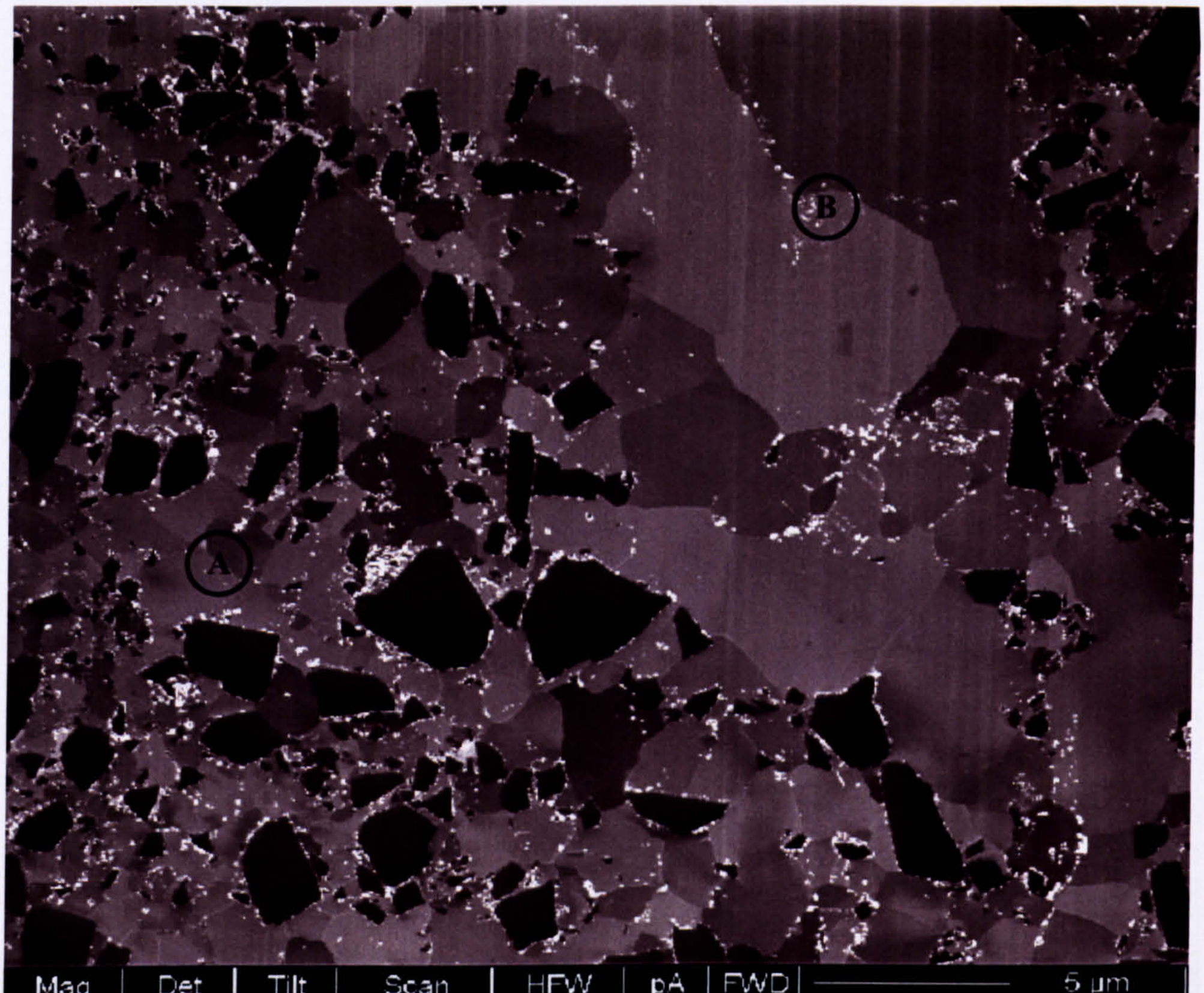


Figure 4.21 – FIB secondary electron image showing grain coarsening in unreinforced region (extruded at 550°C / 20:1 / E-L)

The presence of hard particles in the microstructure acts to impede deformation textural development, which is typically observed during the secondary processing of conventional aluminium alloys. This is due to the relaxation of deformation-induced primary dislocation structures, which leads to localised grain rotation that is not indicative of the bulk of the matrix. The extent of this effect is influenced by the particle size and the interparticulate spacing (111).

It has been demonstrated that small particles ($f/d > 0.1\ \mu m^{-1}$) are highly effective at pinning high angle grain boundaries in aluminium alloys (112). On the other hand, larger particles (> 1μm) tend to stimulate formation of recrystallisation nuclei (113). In the MMC, the modal reinforcement particle size is 3 μm, however, a typical particle size distribution (Figure 4.22) demonstrates that approximately 6% of particles are less than 1 μm in size, prior to processing. The mechanical alloying process is known to further reduce the average SiC particle size, so a situation arises where the

reinforcement particles, depending on their size, may act to either pin grain boundaries and thus inhibit growth of recrystallisation fronts or, conversely, stimulate recrystallisation. Combined with the presence of the fine oxide phase and the strengthening precipitates, it can be seen that study of the relative contribution of these particles on microstructural evolution during secondary processing and heat treatment is complex.

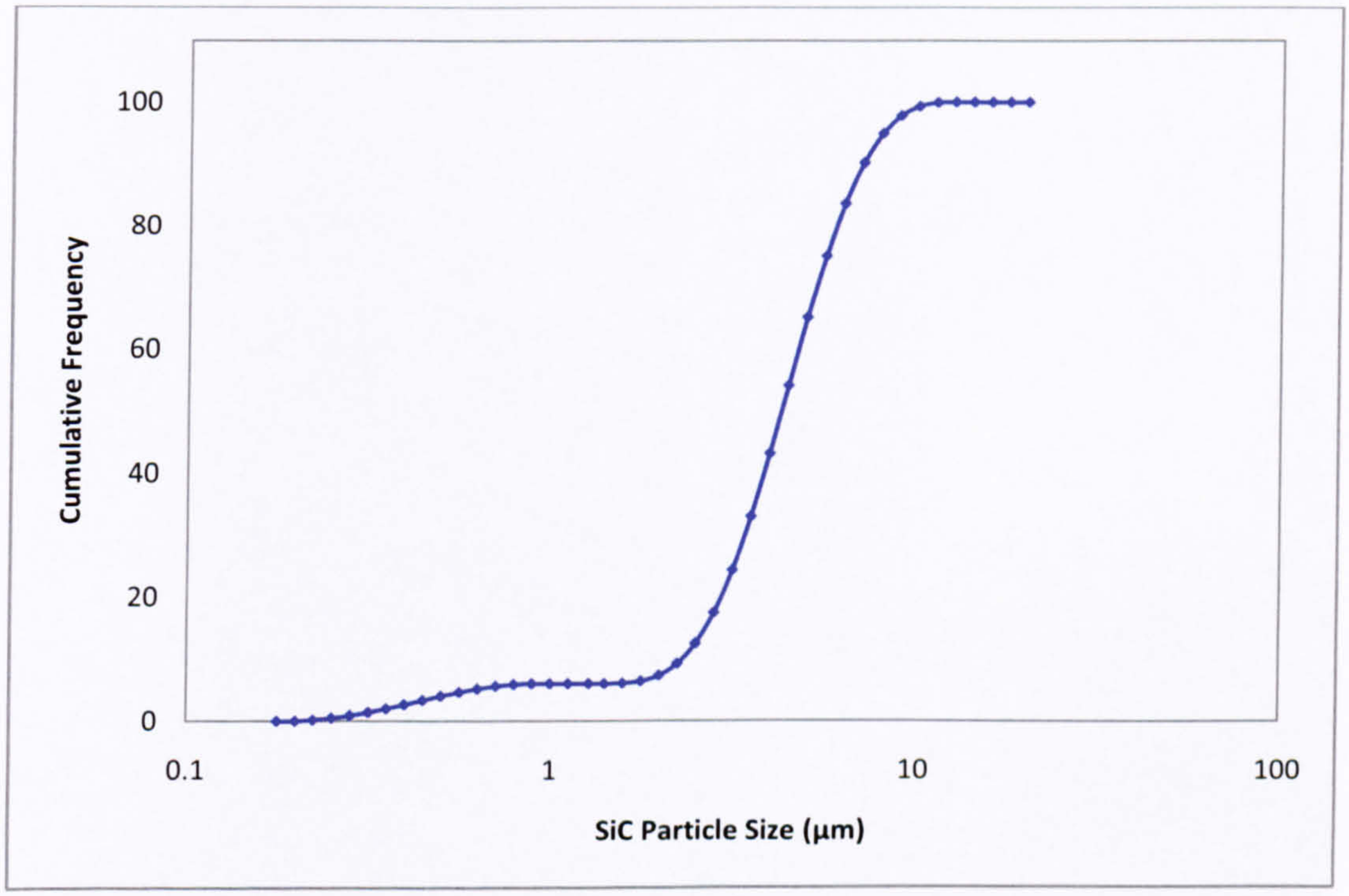


Figure 4.22 – Typical SiC Particle size distribution

Zener pinning occurs where particles inhibit grain boundary migration through a reduction in grain boundary area. Theoretical calculations in the literature have shown that the drag pressure for oxide particles in aluminium MMCs tend to be in the order of 0.1 MPa (114). In practise it has been shown that oxide particles in PM MMCs play a more significant role in hindering nucleation and grain growth of recrystallisation fronts (31) (115) (116).

The FIB microscopy study provides strong evidence to suggest that oxide particles act to pin grain boundary motion within AMC225xe. Bright white particles have been observed in all of the secondary electron images captured on the FIB microscope, as demonstrated in Figure 4.23, below. The particles and necklaces are typically located at

the matrix/reinforcement interface and at grain boundaries. The particles range in size from 20 nm to 200 nm.

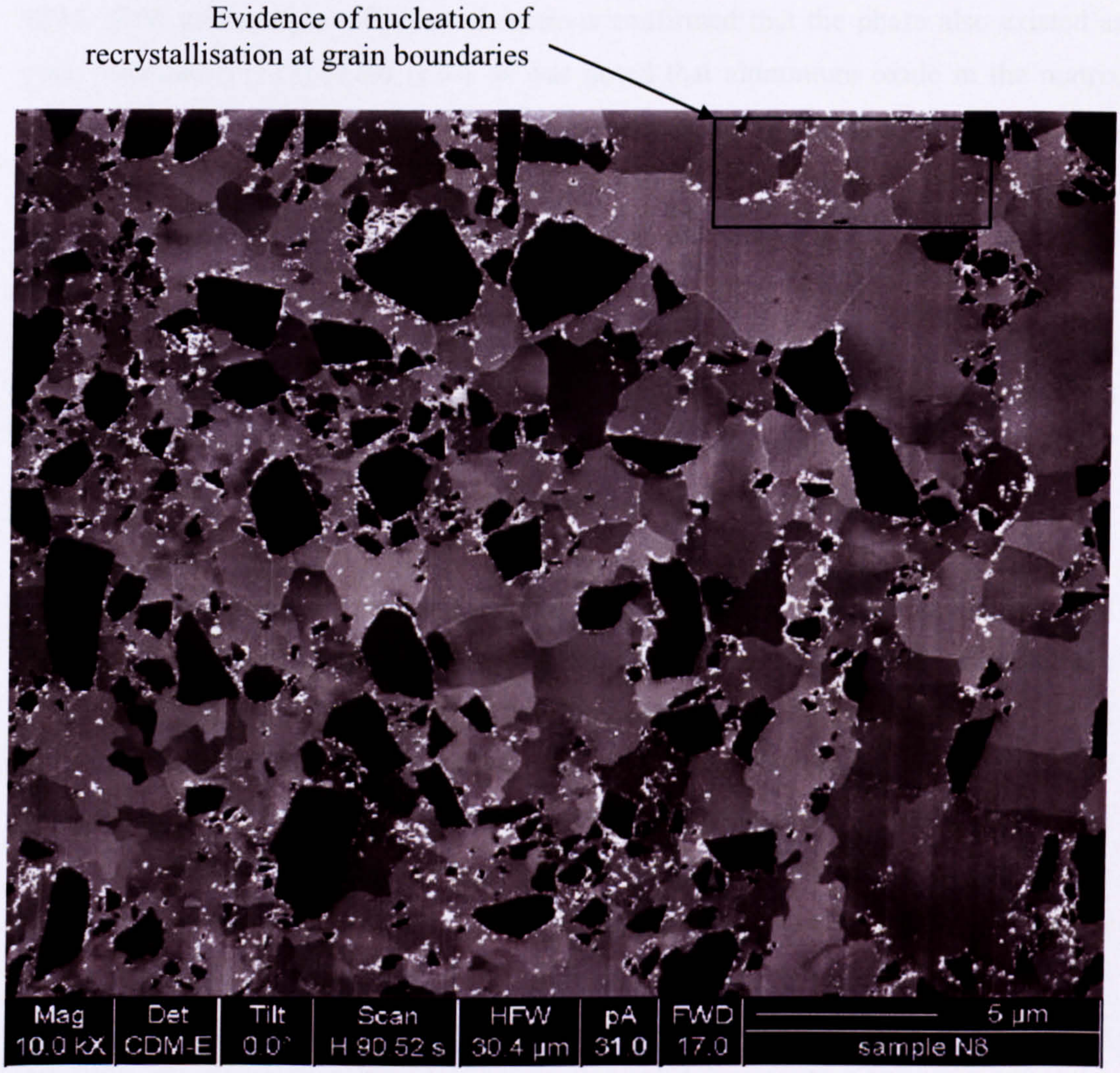


Figure 4.23 – FIB secondary electron image showing oxide particles at grain boundaries and interfaces (extruded at 550°C / 20:1 / E-L)

These particles have also been observed in previous microstructural studies on aluminium metal matrix composites. In one such study, similar bright features were observed at the matrix/reinforcement interfaces in an AA2080 alloy reinforced with 20 volume percent SiC particles at 3 µm in size (117). Following TEM analysis using selected area diffraction, it was discovered that these layers were 20 nm – 40 nm in thickness and amorphous. EDS analysis indicated that they were rich in Si, Mg, Al and O. Other studies on AA6xxx series based aluminium MMCs have also observed this phenomenon. For example, in a study on an MMC consisting of an Al-Mg-Si matrix,

reinforced with alumina, a fine dispersion of bright particles at the matrix/reinforcement interface were discovered to be Al_2MgO_4 (spinel). The phase was identified by dissolving the matrix and analysing the reinforcement particle surfaces by EDS in an SEM. SEM micrographs of polished sections confirmed that the phase also existed at grain boundaries (118) (119) (120). It was noted that aluminium oxide in the matrix became unstable in the presence of magnesium to form Al_2MgO_4 for magnesium concentrations of greater than 1 wt% and less than 4 wt%. Above 4 wt% magnesium, MgO would form. In the current study, the magnesium content is 1.2 wt% – 1.8 wt% so the most likely reaction product would be Al_2MgO_4. Spinel formation can occur in the solid state as aluminium oxide remains unstable below the solidus line (121). Although the kinetics would be retarded it would still be possible for the reaction to proceed within the current process due to the high temperature thermal exposure of the MMC during degassing, consolidation and heat treatment stages of manufacture.

In previous investigations on a magnesium alloy reinforced with particulate SiC, FIB imaging indicated the presence of a magnesium oxide phase at the matrix/reinforcement interface (122) (14). It was postulated that the phase formed during squeeze casting of the MMC when the magnesium reacted with silicon dioxide present on the surface of the SiC particle. It was also observed that subsequent thermomechanical work could cause the MgO to be detached from the SiC surfaces and become entrained in the matrix. As for the current work, the oxide phase could be observed in secondary electron micrographs due to a combination of ion channelling, topographic and atomic number contrast.

In a study most relevant to the current work the bright white particle dispersion was also discovered in a boron carbide reinforced Al-Cu-Mg alloy (123). This MMC was manufactured according to the same route as AMC225xe with the only difference being the type of reinforcement phase employed. The particles were first identified during FIB microscopy. By utilising the Secondary Ion Mass Spectrometry (SIMS) capability of the same system it was possible to gain chemical information relating to the nature of the bright particles. Regions containing high concentration clusters of the particles were subjected to FIB sputtering whilst secondary ions were collected. A mass spectrum could be obtained from the secondary ion data. The same procedure was carried out on regions bereft of white particles to obtain a "background" spectrum.

The spectrums obtained from the scans are shown in Figure 4.24, below.

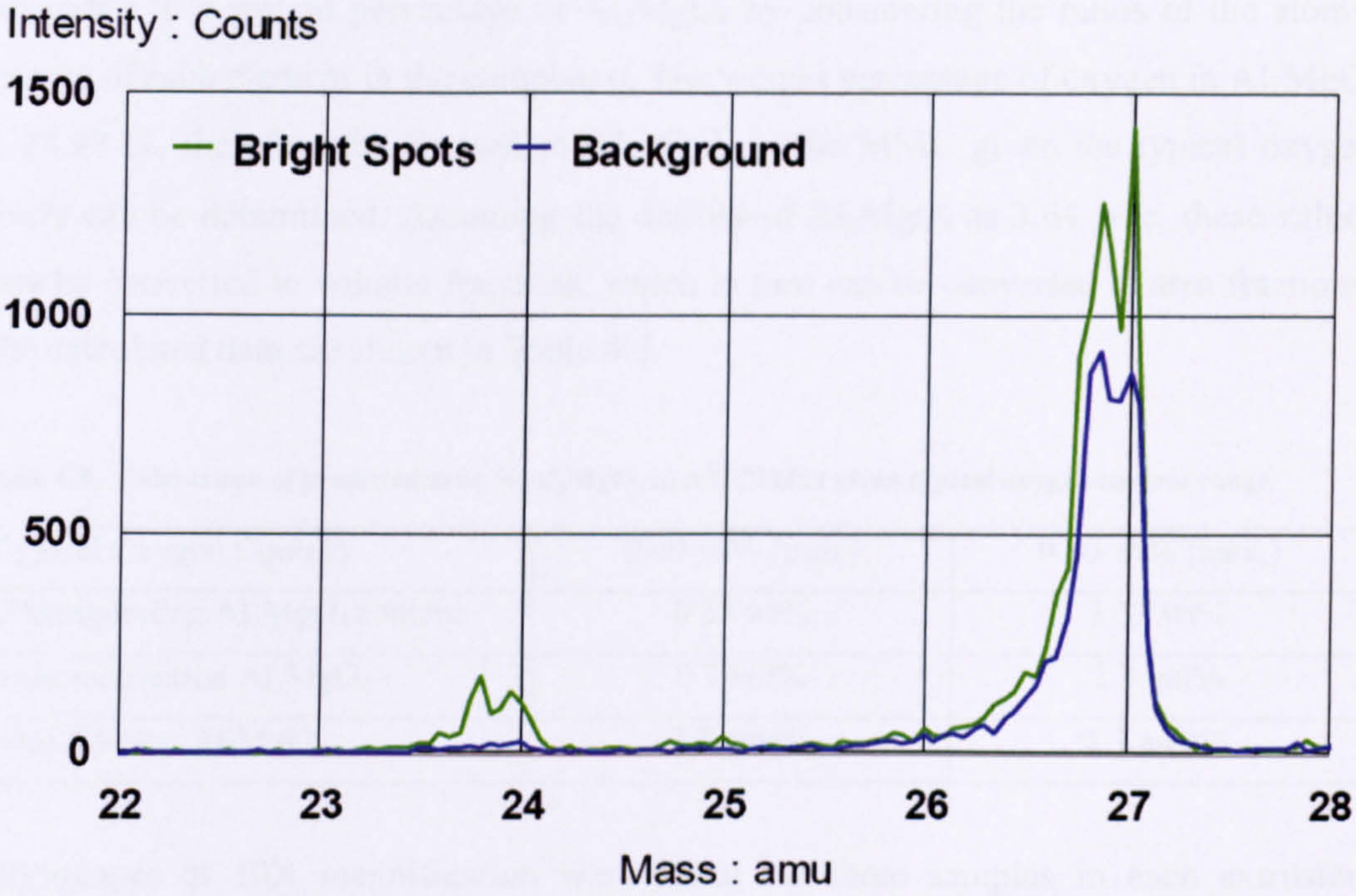


Figure 4.24 - SIMS mass spectrum of bright spot regions and background

The peak at 24 amu indicated the presence of magnesium, which was confirmed by additional peaks at 25 amu and 26 amu, representing magnesium isotopes, which corresponded well to natural abundance values. This evidence helped to substantiate the notion that the bright white particles are the Al_2MgO_4 phase.

A similar SIMS analysis was carried out to determine whether oxygen was also present in the regions containing bright spots (124). Although less conclusive due to the high "background" signal for oxygen in the sample, oxygen levels in the bright spot regions were found to be almost double those in the background regions. It is thought that the background oxygen signal was relatively high due to the instantaneous re-oxidisation of the FIB polished surface in the presence of the residual vacuum species.

For additional clarification, the area percentage of the bright white spots found in the micrographs was calculated and compared to predicted Al_2MgO_4 levels, based on typical oxygen contents of the MMC.

Routine gas analysis carried out by AMC on AMC225xe shows that oxygen contents typically vary in the range of 0.4 wt% to 0.6 wt%. These typical values can be converted to a weight percentage of Al_2MgO_4 by considering the ratios of the atomic masses of each element in the compound. The weight percentage of oxygen in Al_2MgO_4 is 44.98 %, therefore the amount of Al_2MgO_4 in the MMC given the typical oxygen levels can be determined. Assuming the density of Al_2MgO_4 as 3.64 g/cc, these values may be converted to volume fractions, which in turn can be converted to area fractions. The calculated data are shown in Table 4.5.

Table 4.5 - Calculation of predicted area % Al_2MgO_4 in AMC225xe given typical oxygen content range

Typical Oxygen Content	0.40 wt% (min.)	0.60 wt% (max.)
Corresponding Al_2MgO_4 content	0.89 wt%	1.33 wt%
Volume fraction Al_2MgO_4	0.7 vol%	1.1 vol%
Area fraction Al_2MgO_4	0.7 area%	1.1 area%

FIB images at 10X magnification were taken for three samples in each extrusion condition. A threshold was applied to each micrograph using ImageJ image analysis software to extract the bright spots. The area percentage of the spots was determined with the software by dividing the area percentage of the threshold by the total area percentage of the image. Little variation in area percentage was observed for samples from each extrusion temperature, indicating that the abundance of the phase was independent of this parameter. Typical values ranged from 0.8 area% to 1.5 area%. This correlates reasonably well with the predicted values for the Al_2MgO_4 phase from Table 4.5. Discrepancies may be due to the subjective approach of image thresholding or differences between the theoretical and experimental property data for Al_2MgO_4. Again these findings provide strong evidence to suggest that the bright spots represent the Al_2MgO_4 phase.

Based on the available data, it was possible to determine the extent of the drag effect of the oxide particles on grain boundaries migration. The drag pressure for a random array of spherical particles, assuming that the each exert the same maximum pinning force, can be approximated using the following equation (125):

$$P_{Zener} = \frac{3\gamma f}{d}$$

Equation 4.10

where γ represents the grain boundary energy per unit area, f is the volume fraction of the pinning phase and d is the diameter of the pinning particles. An appropriate value of γ was taken from the literature for an unreinforced aluminium as 0.33 MJ/m^2 (126).

The value of f was taken to be 0.01, as this figure satisfied both the theoretical amount based on oxygen analysis of the MMC and the experimentally determined value based on the microstructural evaluation. The mean diameter of the particles was deduced by assessment of the particle size distribution, as shown in Figure 4.25. As can be seen, it was not possible to detect particle sizes below 20 nm in size due to limitations in resolution (~4 nm) and quality of images at high magnifications. The modal diameter, assuming spherical particles, was found to be 22.4 nm.

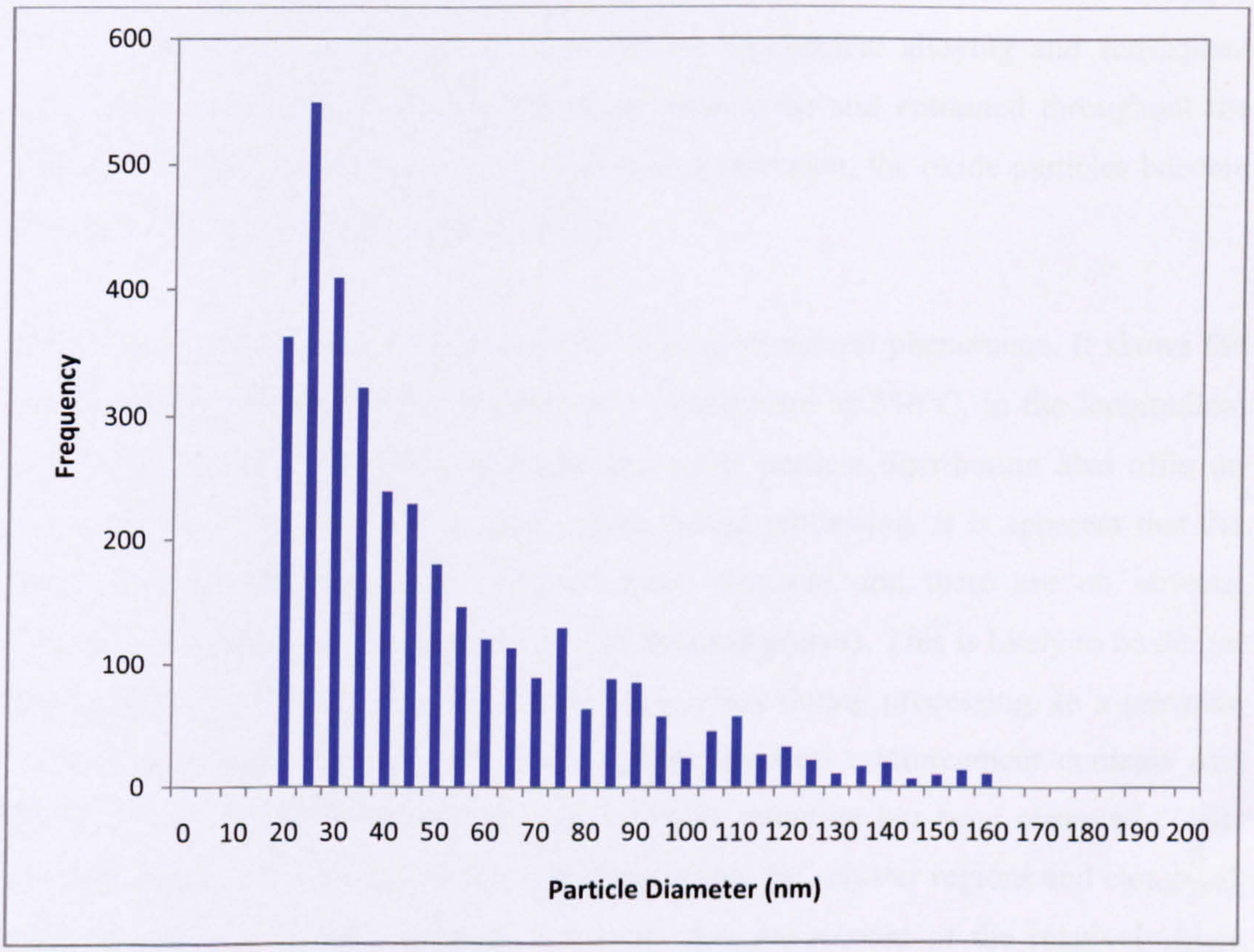


Figure 4.25 - Histogram of spinel particle size distribution

By substituting these data into Equation 4.10, a value of 0.44 MPa was obtained for the drag pressure. This value is considerably higher than the predicted value of 0.1 MPa

reported in the literature (30). Even if a mean particle diameter of 50.1 nm was used instead of the modal value, the drag force derived is 0.18 MPa, which is still in excess of the predicted value. The likelihood is that the calculation in the literature is based on alumina being the oxide phase, however the conclusion that this phase is in fact spinel in the current material under study will lead to an increase in the theoretical volume fraction of oxide particles present in the MMC.

Both of these values are significant and support the notion that inhibition of both nucleation and growth of recrystallisation fronts by Zener drag is considerable in aluminium MMCs containing oxide dispersions.

As discussed, Figure 4.23 indicates the presence of the Al_2MgO_4 phase in AMC225xe. It can be seen that the particles not only exist at the matrix reinforcement interfaces but also at grain boundaries. The particles are thought to have been formed initially at alloy powder surfaces following atomisation, when the aluminium reacts with air, resulting in the formation of a surface oxide layer. During mechanical alloying and subsequent fabrication stages, the oxide boundaries are broken up and entrained throughout the matrix. Previous studies have shown that during extrusion, the oxide particles become aligned with the direction of extrusion (30).

Figure 4.23 provides evidence for additional microstructural phenomena. It shows the microstructure of AMC225xe extruded at a temperature of 550°C, in the longitudinal extrusion direction. The grain structure and oxide particle distribution also offer an indication as to the direction of matrix flow during processing. It is apparent that the matrix has largely retained its original grain structure and there are no obvious indicators of grain elongation due to the deformation process. This is likely to be due to the fact that the SiC particles have a shielding effect during processing. In a previous study of aluminium MMCs with lower volume fraction reinforcement contents and therefore higher interparticulate spacing, a duplex structure has been observed (116). This structure consisted of equiaxed subgrains within SiC cluster regions and elongated subgrains outside of these regions. It appears that on account of the relatively high density of the reinforcement in AMC225xe, there is very little opportunity for grain elongation within the matrix during deformation due to the constraining effect of the SiC particles on high angle grain boundary migration.

Recrystallisation is promoted by the presence of reinforcement particles, however nucleation efficiency is somewhat retarded due to the pinning effect of oxide dispersions on low angle grain boundaries and SiC particles on high angle grain boundaries (111) (116). The net effect is a reduction in the number of nucleated recrystallisation grains and a finer recrystallised grain size than would otherwise be observed. Figure 4.23 shows evidence of the nucleation of recrystallised grains, in a region of relatively low reinforcement particle density, at grain boundaries. It is of note that the recrystallised grains appear to have been pinned by the spinel phase which is abundant in these regions. This microstructural evidence further substantiates the notion that the growth of recrystallisation fronts is inhibited by the presence of the fine dispersion of oxide particles.

As discussed, there are two opposing microstructural mechanisms at work and the potential for promotion of recrystallisation must also be considered. Theory suggests that on account of the increased stored energy in MMCs compared to their monolithic counterparts, the driving force for recrystallisation is much higher and therefore can occur at lower temperatures as illustrated in Figure 4.26.

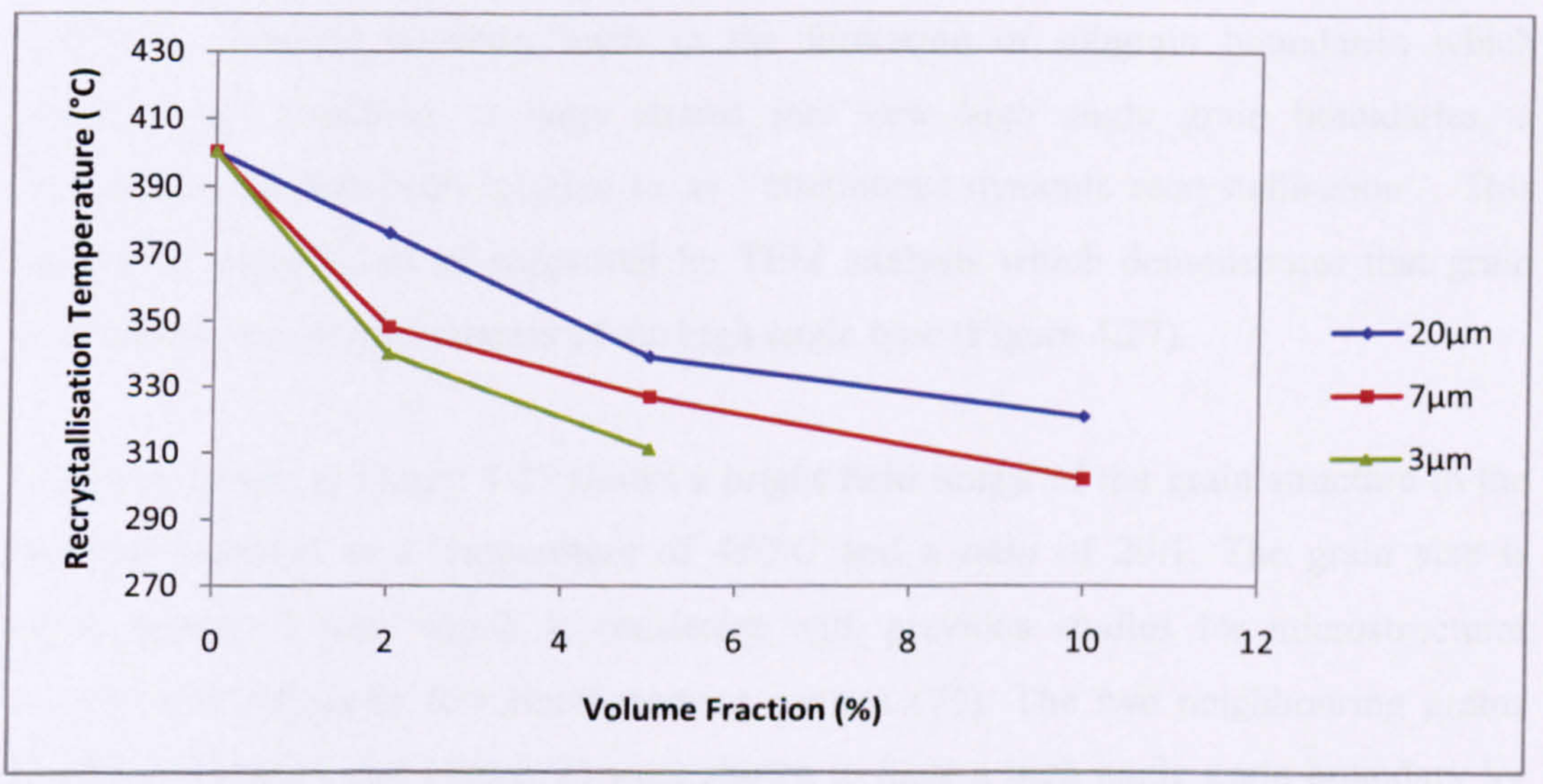


Figure 4.26 - Influence of particle size and volume fraction on recrystallisation temperature in an Al MMC. Adapted from (115)

At higher processing temperatures, the driving force towards particle stimulated recrystallisation is retarded as the amount of stored energy available is considerably less than at lower temperatures. This is because there is no dislocation accumulation in the

proximity of the ceramic particles because dislocation climb and diffusion are able to relax the primary dislocation structures (30). The current work, however, suggests that recrystallisation does not tend to occur at lower secondary processing temperatures. Instead, dynamic recovery appears to take place due to the high levels of stored energy within the matrix.

Aluminium is a high stacking fault energy material and is characterized by easy dislocation climb and cross slip during deformation. Previously, dynamic recovery was believed to be the only mechanism promoting softening during the plastic deformation processing of aluminium alloys. Recently it was observed that dynamic recovery, dynamic recrystallisation or their combination occur under certain conditions during deformation. Lin et al. studied the combination of dynamic recovery and dynamic recrystallisation during hot compression of an aluminium alloy (127). Dynamic recrystallisation was found to occur under certain conditions involving a specific combination of temperature and strain rate.

The uniform and fine grain size observed during the FIB analysis of AMC225xe may be partly attributable to the occurrence of dynamic recrystallisation (128) (129). In particular, dynamic recovery leads to the formation of subgrain boundaries which progressively transform at large strains into new high angle grain boundaries, a mechanism that has been referred to as ''continuous dynamic recrystallisation''. This supposition appears to be supported by TEM analysis which demonstrates that grain boundaries were predominantly of the high angle type (Figure 4.27).

The micrograph in Figure 4.27 shows a bright field image of the grain structure in the material extruded at a temperature of 450°C and a ratio of 20:1. The grain size is approximately 2 μm, which is consistent with previous studies for microstructural regions with relatively low reinforcement content (73). The two neighbouring grains (right hand side, 1 and centre, 2) were shown to have a high angle grain boundary by comparing selected area diffraction patterns (SADPs) for each grain. The zone axes were [112] and [111] respectively. Grain 2 exhibited a fine anomalous precipitate throughout, which could not be positively identified during the TEM study. The dark regions at the periphery of the image are SiC reinforcement particles. Intermetallic particles are also clearly visible within the grains and range in size from 50 nm to 150 nm which is consistent with the earlier FIB microscopy analysis.

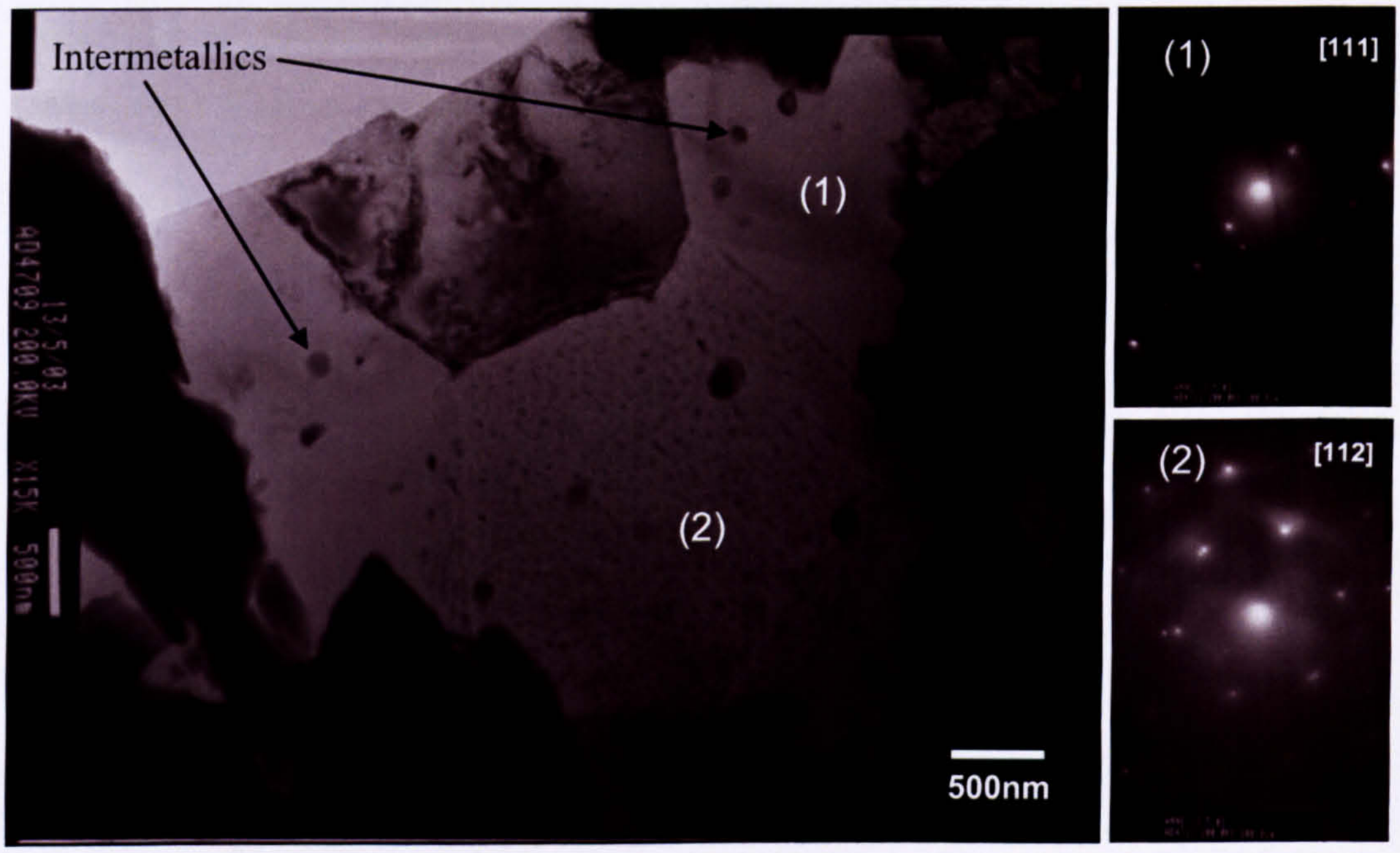


Figure 4.27 - Bright field image of grain structure, surrounded by SiC particles (main) and SADPs of grains (1) and (2) (extruded at 450°C / 20:1 / E-T)

Section 4.6: Microstructural Analysis of Aluminium MMC by FIB Imaging, details the grain structure analysis of AMC225xe by FIB imaging. The table below shows a summary of the data obtained by this technique. This data has been augmented with an analysis of the average grain size prior to secondary processing (the as-HIP'ed condition) to offer an indication as to the microstructural evolution that has occurred and the mechanisms that are involved.

Table 4.6 - Influence of extrusion temperature on grain size

Extrusion Temperature (°C)	As-HIP'ed Billet	350°C	450°C	550°C
Average Grain Size (μm)	0.92 (±0.01)	0.66 (±0.04)	0.73 (±0.03)	0.95 (±0.05)

As Table 4.6 demonstrates, extruding at 350°C and 450°C, has led to a reduction in average grain size of 28% and 21% respectively. Evidence suggests that this is due to the development of a subgrain structure through the formation of low angle grain boundaries, followed by subgrain rotation giving rise to a combination of low angle and high angle grain boundaries. This theory is supported by microtexture analysis in Section 4.7: Microtexture Analysis by Focussed Ion Beam Microscopy. As the rate of recovery diminishes at higher extrusion temperatures, the formation of a subgrain

structure is inhibited. For an extrusion temperature of 550°C the average grain size has marginally increased, indicating that recrystallisation and grain growth may have occurred at this temperature.

Texture

An X-Ray Diffraction study of the macrotextures of the MMC extruded at three different extrusion temperatures gives an indication as to the prevalent deformation mechanisms operating in each extrusion condition (Figure 4.28).

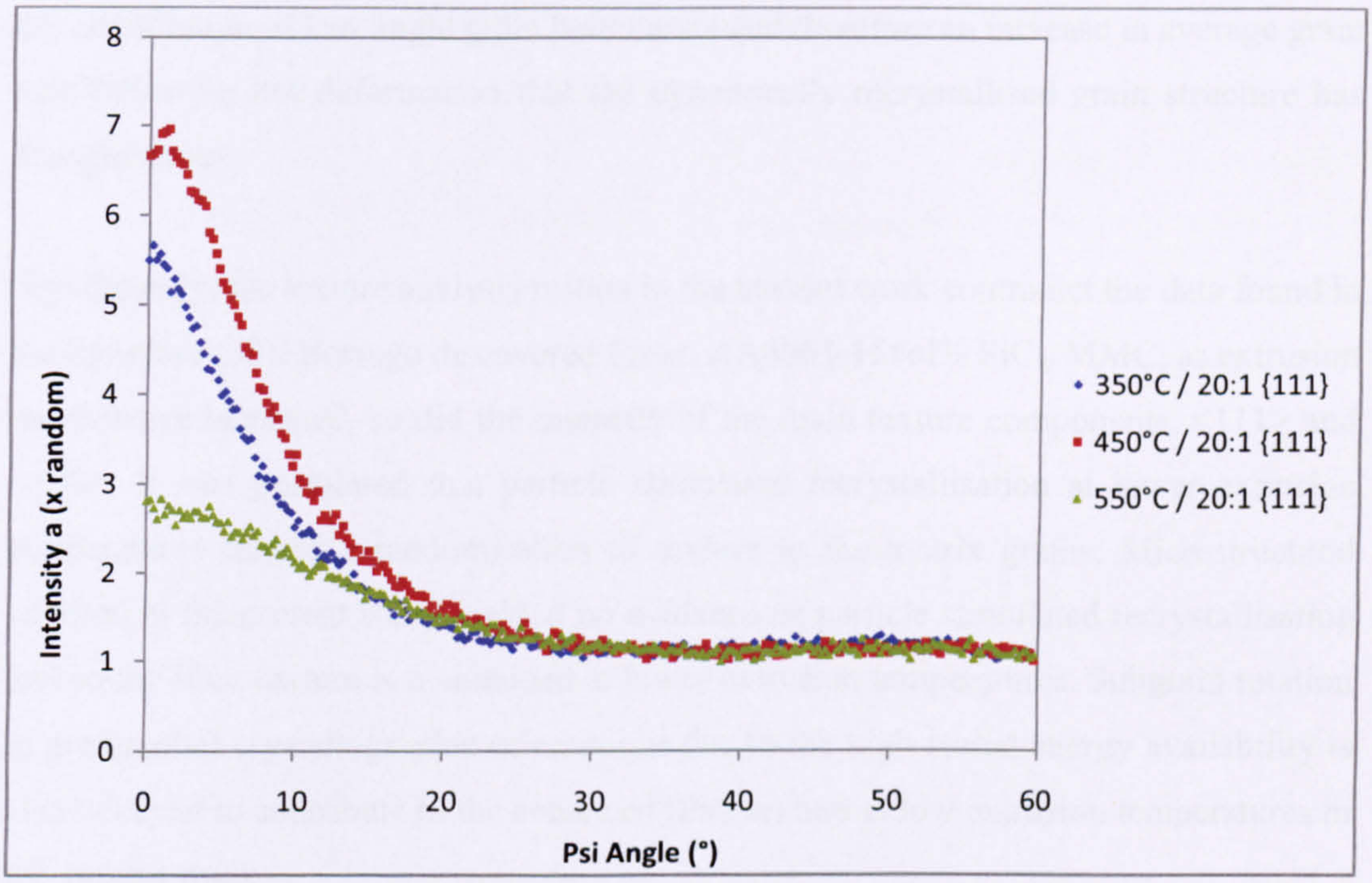


Figure 4.28 – Section of pole figure showing <111> Deformation textures in extruded AMC225xe

As can be seen, for material extruded at 350°C and 450°C a <111> deformation texture is evident, albeit a weak one. Dillamore and Roberts reported that extrusion textures in F.C.C. materials have been observed as double fibre textures combining the <111> and <100> textures parallel to the fibre axis (130). The presence of a weak <111> deformation texture in the MMC is consistent with previous studies, which have shown a 40% weakening of the <111> deformation texture of a 20% reinforced aluminium MMC, compared to the unreinforced alloy (131). Additionally, Grewen and Wasserman demonstrated that the <111> fibre texture was significantly weakened by the presence of impurities in aluminium (132). The key finding in the current work is that this <111> deformation texture is no longer observed for the material extruded at 550°C. The

assertion is that although particle stimulated recrystallisation may have been retarded at this temperature through a reduction in available stored energy, grain boundary nucleation of recrystallised grains is still possible. This is evidenced by the microstructure of Figure 4.23, which clearly indicates the presence of recrystallised grains in regions of relatively low volume fraction reinforcement. It is likely that the recrystallisation phenomenon has placated the texture effect generated during the extrusion process. The fact that the yield strength of the MMC is lower at this temperature would indicate that the recrystallised grain structure offers a reduction in strength compared to a non-recrystallised microstructure. This is primarily a result of the annihilation of low angle grain boundaries and therefore an increase in average grain size following hot deformation that the dynamically recrystallised grain structure has brought about.

Significantly, the texture analysis results in the current work contradict the data found in the literature (33). Borrego discovered for an AA6061-15vol% SiC_w MMC, as extrusion temperature increased, so did the intensity of the main texture components, <111> and <100>. It was postulated that particle stimulated recrystallisation at lower extrusion temperatures caused a randomisation of texture in the matrix grains. Microstructural analysis in the current study yielded no evidence of particle stimulated recrystallisation and so the fibre texture is maintained at lower extrusion temperatures. Subgrain rotation to preferential crystallographic orientations due to the high stored energy availability is also believed to contribute to the enhanced fibre texture at low extrusion temperatures in the current study.

4.6 Microstructural Analysis of Aluminium MMC by FIB Imaging

The most effective technique for analysing the microtexture of the MMC was found to involve FIB polishing and imaging. A process was originally developed by M.W. Phanuef whereby a FIB polished section was tilted and imaged at a range of incremental angles (14). The intensity of individual grains could be plotted as a function of tilt angle and it was possible to determine relative individual grain orientations based on the angular width of troughs and the angular distance between troughs.

Previously, this technique has never been applied to MMCs so the current work would explore the capability of the process for this material.

Initially, it was necessary to identify individual grains and subgrains within the composite in order to differentiate between them during microtexture analysis. The FIB imaging technique proved very effective in differentiating between individual grains and subgrains. On this occasion, it was decided to tilt the specimen through 45° and image at 1° increments. This was deemed necessary as a single image at a specific tilt angle could not differentiate between two adjacent grains with similar orientations. In practise, it was discovered that imaging the same area a total of 45 times gradually caused surface degradation due to the damage inflicted by the ion beam. This was leading to deterioration in the image quality that inhibited accurate determine of the locations of grain and subgrain boundaries, as shown in Figure 4.29.

A decision was taken to modify the incremental angle to 2°. Although a sacrifice would be made with regards to the sensitivity of the technique, this was deemed to be inconsequential to its relative accuracy. A total of 24 images were taken during the tilting process. Significantly less damage was inflicted on the surface under analysis (see Figure 4.30).

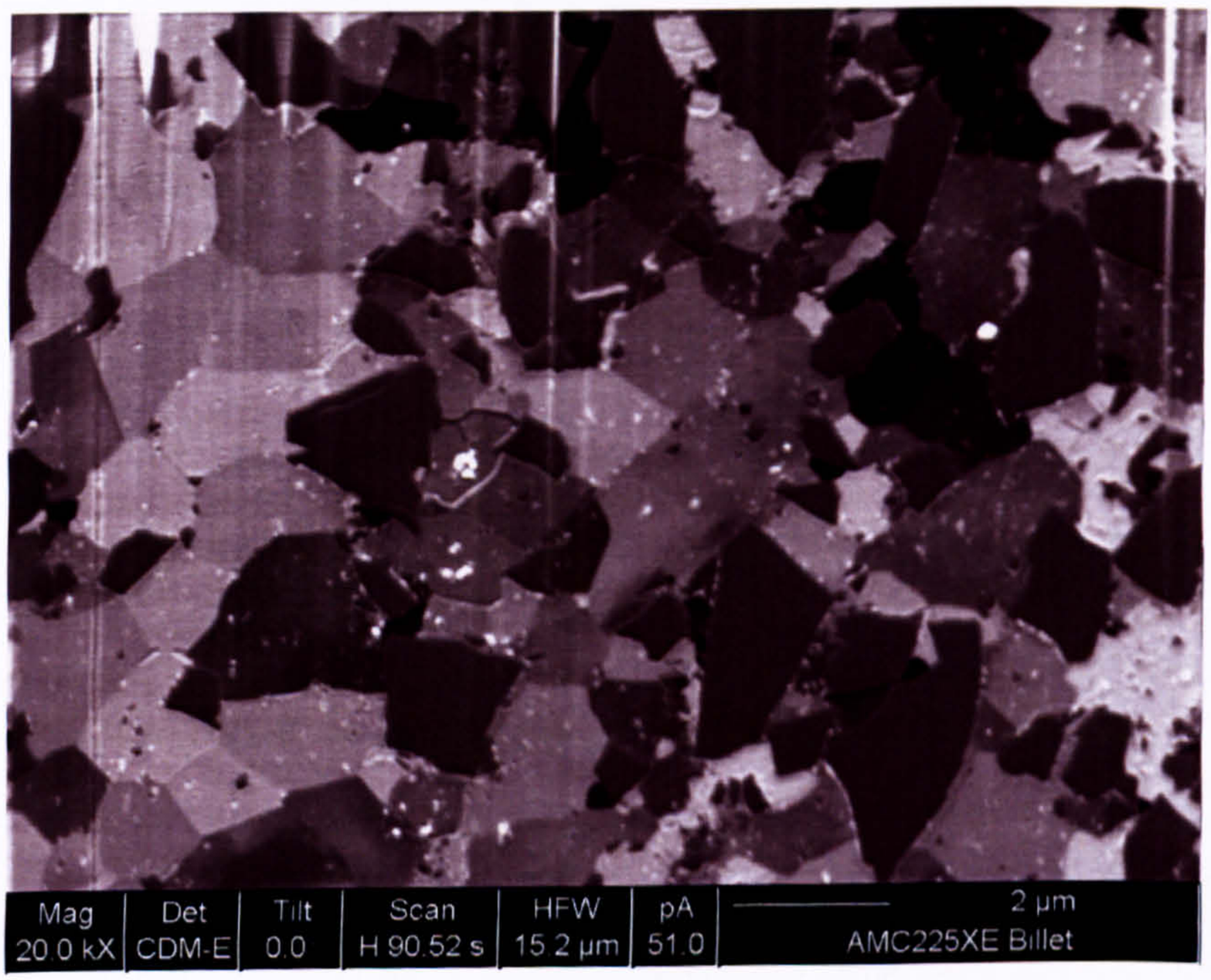


Figure 4.29 – FIB secondary electron image of polished region after being subjected to 45 images (Extruded at 350°C / 20:1 / E-T)

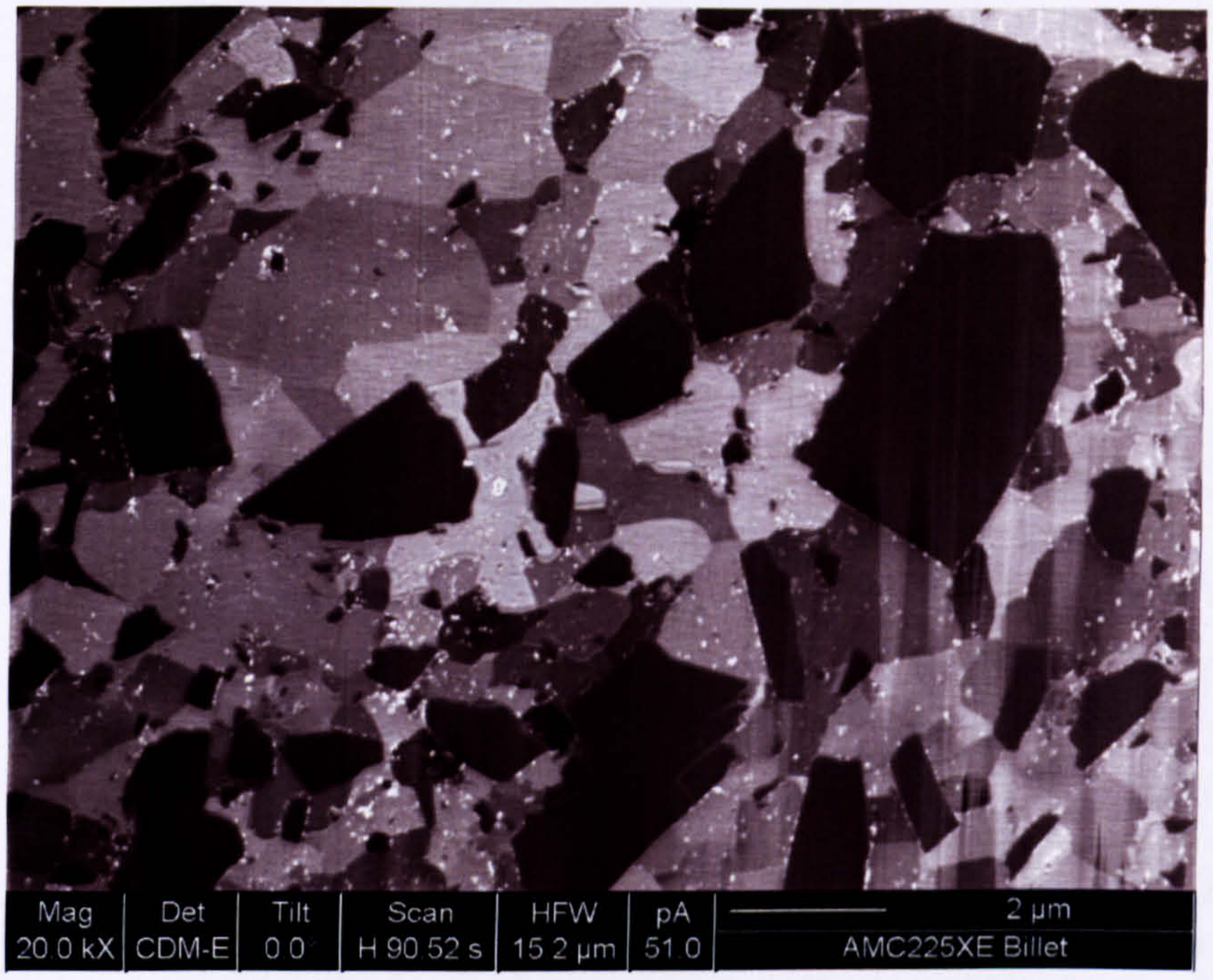


Figure 4.30 – FIB secondary electron image of polished region after being subjected to 24 images (Extruded at 350°C / 20:1 / E-T)

Accurate grain boundary determination was carried out by applying simple image analysis techniques using "ImageJ" image analysis software. The 24 images taken across the 45° tilt angle range were stacked. A 'Find Edges' algorithm was used and the resultant images were overlaid in order to produce a grain/subgrain boundary map, as shown in Figure 4.31.

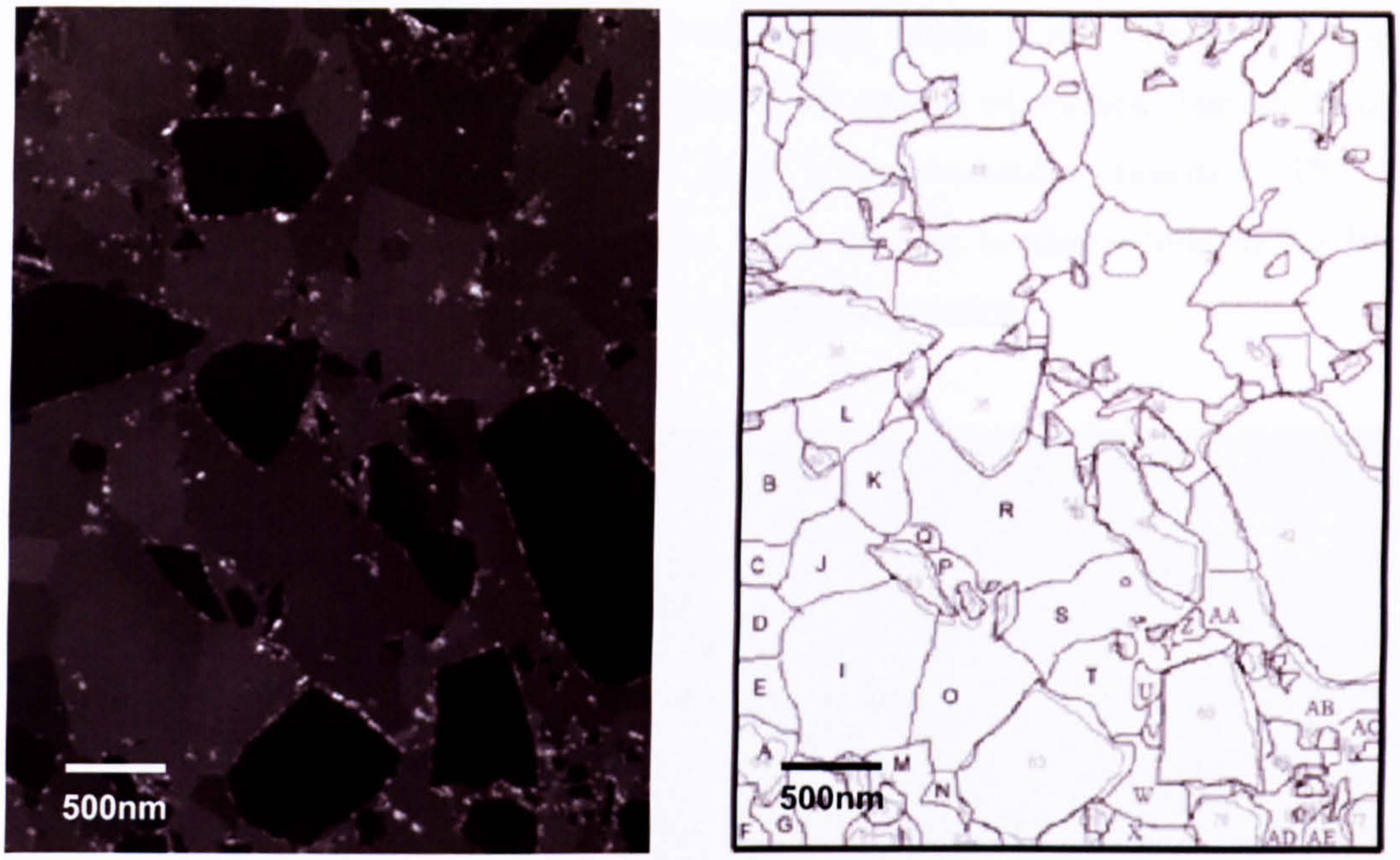


Figure 4.31 - Indexing of aluminium grain structure by analysis of FIB image (Extruded at 550°C / 20:1 / E-T)

Individual grains were then indexed and SiC particles were labelled to differentiate them from the matrix alloy grain structure.

The first level information that could be extracted from the images was grain size and aspect ratio data. Slices were taken from the grip sections of three failed tensile test pieces from each extruded bar, after heat treatment. The slices were spark eroded to a 3 mm diameter and sliced to 0.5 mm thickness at an angle of 30° to the perpendicular of the extrusion axis. The samples were mounted in the FIB in such a way that sections could be polished both perpendicular and parallel to the original extrusion direction.

Initially, a 50 μm x 50 μm surface was milled at an ion beam current of 20 nA in order to remove surface debris and bulk material in preparation for final polishing. The beam current was reduced to 5 nA for rough polishing and final polishing was carried out at 300 pA to ensure a flat surface with limited ion beam damage. After completion of the polishing stage, each specimen was tilted through an angle of 90° so that imaging could be carried out. The ion beam current was reduced to 30 pA, allowing for high quality imaging without inflicting excessive surface damage.

The following sequence of images demonstrates the preparation sequence (Figure 4.32). Image A shows a low magnification overhead perspective of the spark eroded disc.

Image B shows the 50 μm x 50 μm polished region. Image C is a side-on direction of the polished region and gives an indication of the degree of surface flatness. Finally, image D shows the polished surface from a perpendicular direction. The SiC reinforcement phase is clearly visible. Ion beam damage is also visible in the lower portion of the image and is aligned with the ion beam direction.

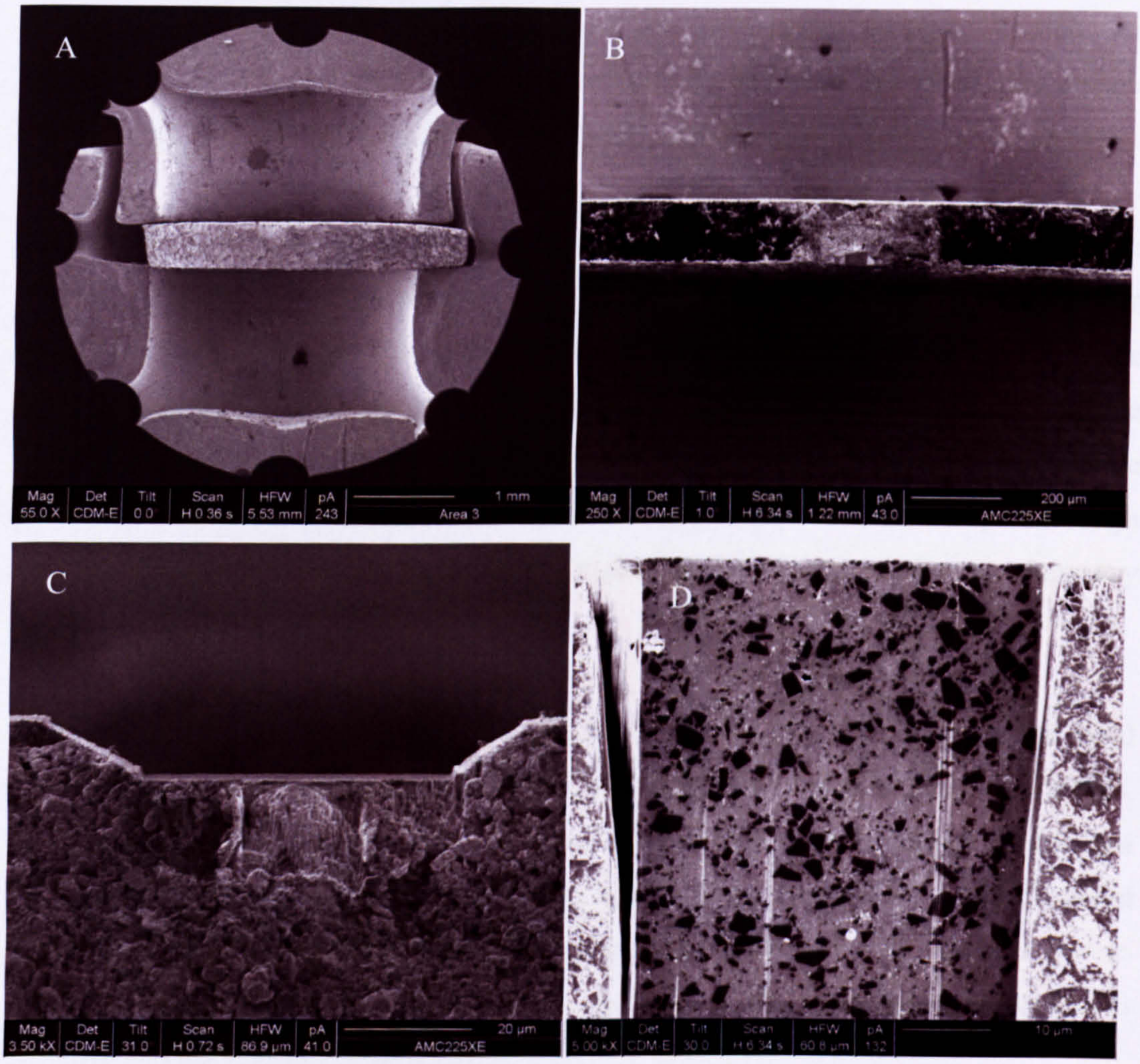


Figure 4.32 - Surface preparation of AMC225xe by FIB milling and polishing

With regards to detection, the FIB microscope operates according to the same principles as the scanning electron microscope (SEM). In the case of a FIB microscope, a beam of positively charged ions is moved in a raster pattern across a surface and the resultant signals, either secondary ions or secondary electrons, are used to form an image (14).

Initial inspection of typical micrographs taken perpendicular to the material surface showed a pale background representing the AA2124 matrix and the SiC particulate phase could be seen as a dark phase distributed throughout the matrix.

There are several causes of image contrast in FIB microscopy, which have been discussed in detail in previous studies (12) (133) (134). For materials science specimens, the three primary mechanisms are orientation contrast through ion channelling, atomic weight contrast and topographic contrast. All three mechanisms interact with each other, depending on the specific nature of the material under analysis.

For metallic specimens, orientation contrast provides a very useful mechanism for grain structure analysis. The mechanism arises from the channelling of secondary ions between lattice planes of the specimen. The depth to which the ions penetrate the specimen surface is dependent upon the relative orientation of the ion beam and the lattice plane and the interplanar spacing of the lattice (14). Channelling contrast can be observed in both secondary ion images and secondary electron images, though secondary electron yield is significantly higher and is less sensitive to chemistry variations.

Atomic weight contrast is more readily observed in secondary ion images where yield variation for different elements is more significant than for secondary electron images. In the current study, however, it was found that secondary electron images contributed useful information to the chemical characterisation of the composite. It was observed that elements with higher atomic weights appeared lighter and this effect is due to higher secondary electron emission rates, just as is the case for a conventional secondary electron image from an SEM.

Topographic contrast can be explained by differences in signal emission as a function of the angle of incidence relative to specimen surface normal as the local inclination of the specimen surface varies (14).

In previous studies it has been observed that milling rates are dependent upon specific grain orientation, whereby sputtering efficiency increases due to alignment of the lattice. The current study, however, shows negligible topographic variation and this is thought to be due to fine grain nature of the MMC. Additionally, it was discovered that

in spite of the significantly slower sputtering rates for the SiC particles, only a minor topographic variation between the matrix and the reinforcement phase was evident. During topographical analysis carried out on a Zygo Newview White light Interferometer, a peak to valley height of approximately 70 nm was detected on an MMC surface prepared by FIB polishing (94). This compares to a value of approximately 650 nm for a conventional diamond polishing technique, illustrating the enhanced capability of the FIB process and its propensity toward preparing flat surfaces.

For the analysis of FIB images taken across a range of tilt angles it was necessary to correct the height of the image in accordance with the incident angle between the specimen and the detector. For a viewing angle perpendicular to the surface of the specimen, no correction was necessary.

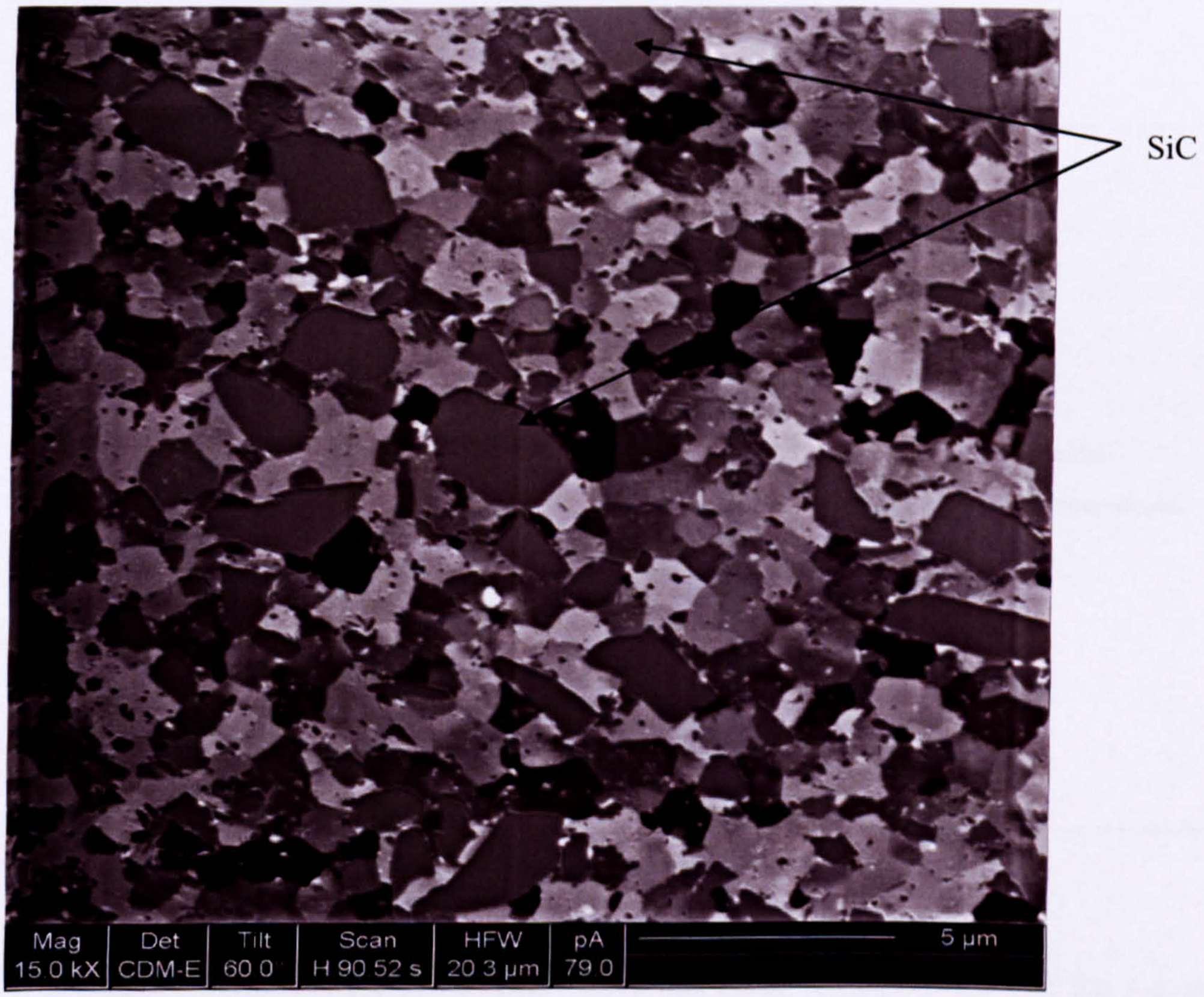


Figure 4.33 – FIB secondary electron image showing a typical microstructure (Extruded at 450°C / 20:1 / E-T)

The above micrograph, Figure 4.33, demonstrates the presence of the SiC reinforcement in the aluminium alloy matrix and shows the high level of grain structural detail that can

be obtained using this preparation and imaging technique. SiC reinforcement particles can be identified as the relatively featureless pale grey phase, as indicated. The surrounding regions are the aluminium alloy matrix and individual grains can be identified due to the orientation contrast phenomenon outlined previously.

Images such as this were captured for samples in each of the five extrusion conditions both parallel and perpendicular to the extrusion axis. A sample of AMC225xe in the as-HIP'ed billet condition was also indexed. All material had been heat treated to a T4 condition prior to analysis. Grain size and aspect ratios were calculated using the ASTM Planimetric Procedure (92). Six regions were indexed for each extrusion condition and the average grain size was determined. Error bars are included to indicate a statistical scatter of ±2 standard deviations.

The results are displayed in Figure 4.34.

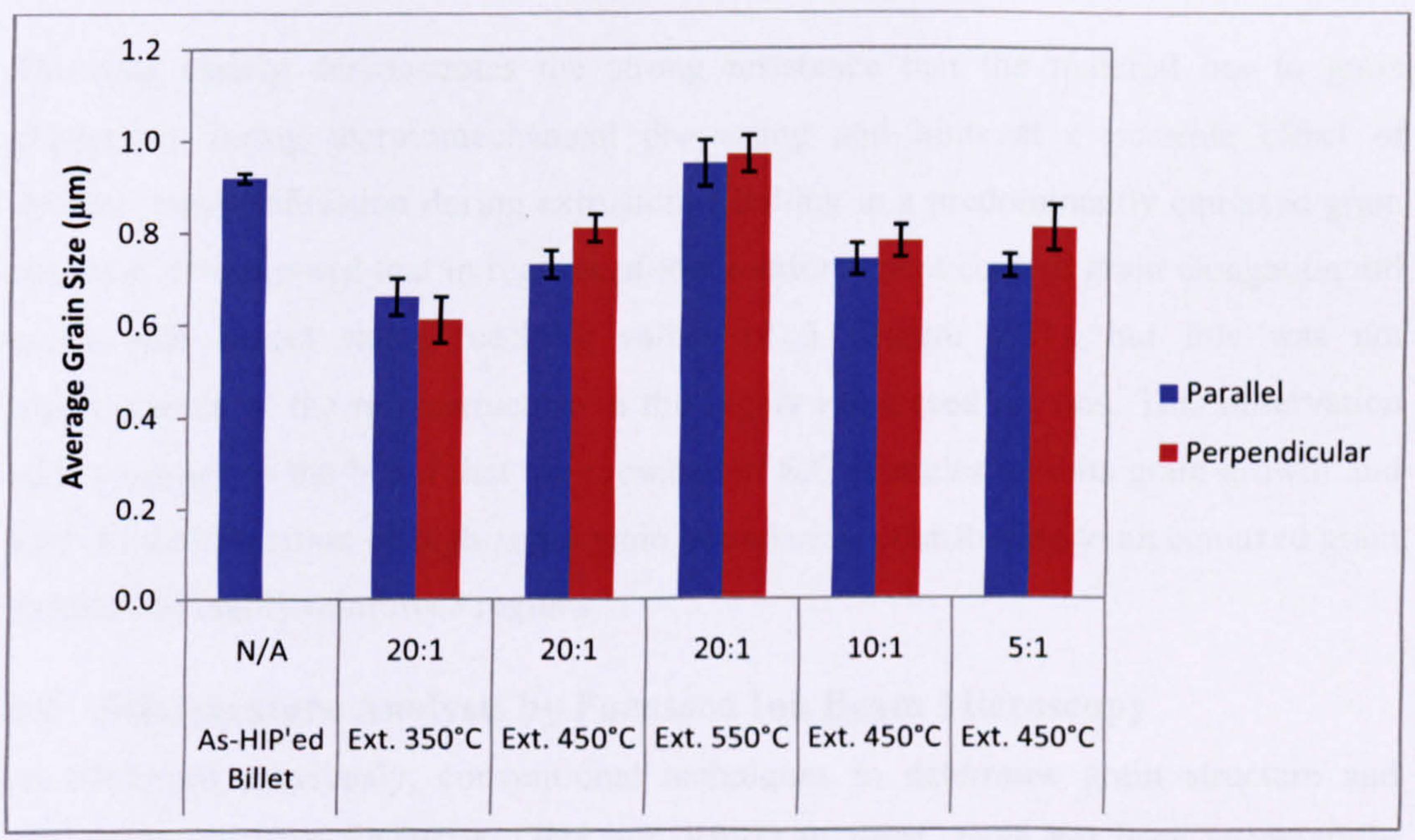


Figure 4.34 - Influence of extrusion temperature and ratio on average grain size

The material condition (extrusion temperature and ratio) is displayed along the x-axis and data are shown for both directions: parallel and perpendicular to the extrusion axis. The as-HIP'ed billet does not possess directional characteristics so a single data point is shown for an arbitrary direction within the billet. Grain size shows an apparent increase

with increasing extrusion temperature whilst the extrusion ratio appears to have a negligible effect on grain size.

Table 4.7 summarises the values for grain aspect ratios in directions parallel and perpendicular to the extrusion axis.

Table 4.7 – The influence of processing conditions on grain structure aspect ratios

Material Condition	As-HIP'ed Billet	Extrusion	Extrusion	Extrusion	Extrusion	Extrusion
Extrusion Temperature	N/A	350°C	450°C	550°C	450°C	450°C
Extrusion Ratio	N/A	20:1	20:1	20:1	10:1	5:1
Aspect Ratio - Parallel	1.01	1.08	0.96	0.99	1.01	0.99
Aspect Ratio - Perpendicular	N/A	1.03	1.00	0.92	0.98	1.05

The data clearly demonstrates the strong resistance that the material has to grain elongation during thermomechanical processing and hints at a possible effect of dynamic recrystallisation during extrusion, resulting in a predominantly equiaxed grain structure. It was noted that in regions of low reinforcement content grain elongation did occur with aspect ratios reaching values of 3 (Figure 4.21), but this was not representative of the microstructure in the highly reinforced regions. This observation adds credence to the belief that the presence of SiC particles inhibits grain growth and leads to the formation of high angle grain boundaries, contributing to an equiaxed grain structure in highly reinforced regions.

4.7 Microtexture Analysis by Focussed Ion Beam Microscopy

As discussed previously, conventional techniques to determine grain structure and orientation, such as SADP in TEM and EBSD in SEM, have not been successfully applied to MMCs with reinforcement particle size and content levels such as those found in the current study. Focussed Ion Beam microscopy provides a novel approach for determining the microtexture of such materials, by exploiting the phenomenon of orientation contrast through ion channelling.

Levi-Setti et al. and Franklin et al. demonstrated the phenomenon of orientation contrast in a nominally pure aluminium alloy (135) (136). Grain intensity was plotted against

deviation from normal incidence as a specimen was tilted through a 45° angle, relative to the ion beam. The intensity of an individual grain was monitored at incremental angles and was found to be dependent upon lattice orientation and interplanar lattice spacing. A similar procedure was carried out in the current study in an attempt to derive grain orientation information from a series of FIB images.

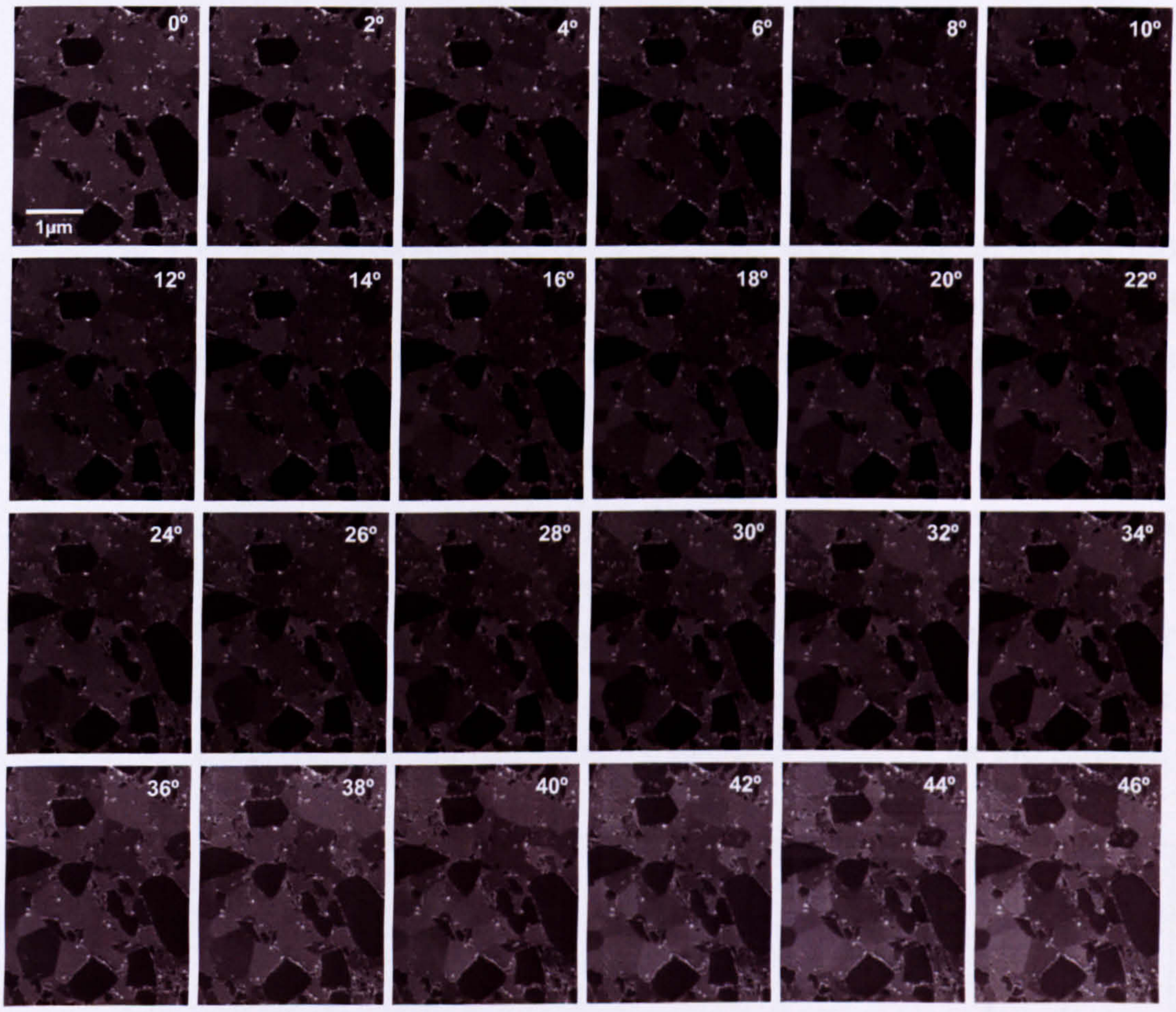


Figure 4.35 - Influence of tilt angle on FIB image (Extruded at 550°C / 20:1 / E-T)

The composite image in Figure 4.35 shows a series of micrographs taken as a specimen was tilted inside the FIB microscope. As the tilt angle becomes more obtuse to the specimen surface, the height of each image decreases due to a foreshortening effect. This behaviour was negated by stretching each image to the size of the original image and allowing the image processing software to interpolate the missing pixels. This technique has been applied to the series of micrographs shown in Figure 4.35.

As mentioned, during the tilting process, the angle between the secondary electron receiver and the specimen surface becomes more obtuse. As this continues, the quantity of secondary electrons that can be received by the detector diminishes. This means that as tilting progresses, subtle variations occur in the interpolated image intensity. It is therefore necessary to normalise the image in order to determine the relative grain grey levels more accurately. This can be done by monitoring the grey level of an amorphous feature on the specimen surface. In the case of the MMC in the current study, the SiC particles provide such a feature and their grey levels were used to normalise the images.

Grey levels were determined by monitoring pixel colouration variations over a specified area using the image analysis software, "ImageJ." Digital images extracted from the FIB microscope were initially converted to greyscale images. A reference point was located on a SiC particle within each image and its grey level was recorded through the full range of tilt angles using a colour extraction software tool.

Figure 4.36, below, shows the variation in grey level intensity of six SiC particles from the region in Figure 4.35 as it is tilted through an angle of 46° from the normal (0°) at 2° increments. As can be seen, as the tilt angle increases so does they grey level (region of interest becomes lighter in colour). Also of note is the fact that the grey levels are identical for each particle indexed confirming the amorphous nature of the SiC particles.

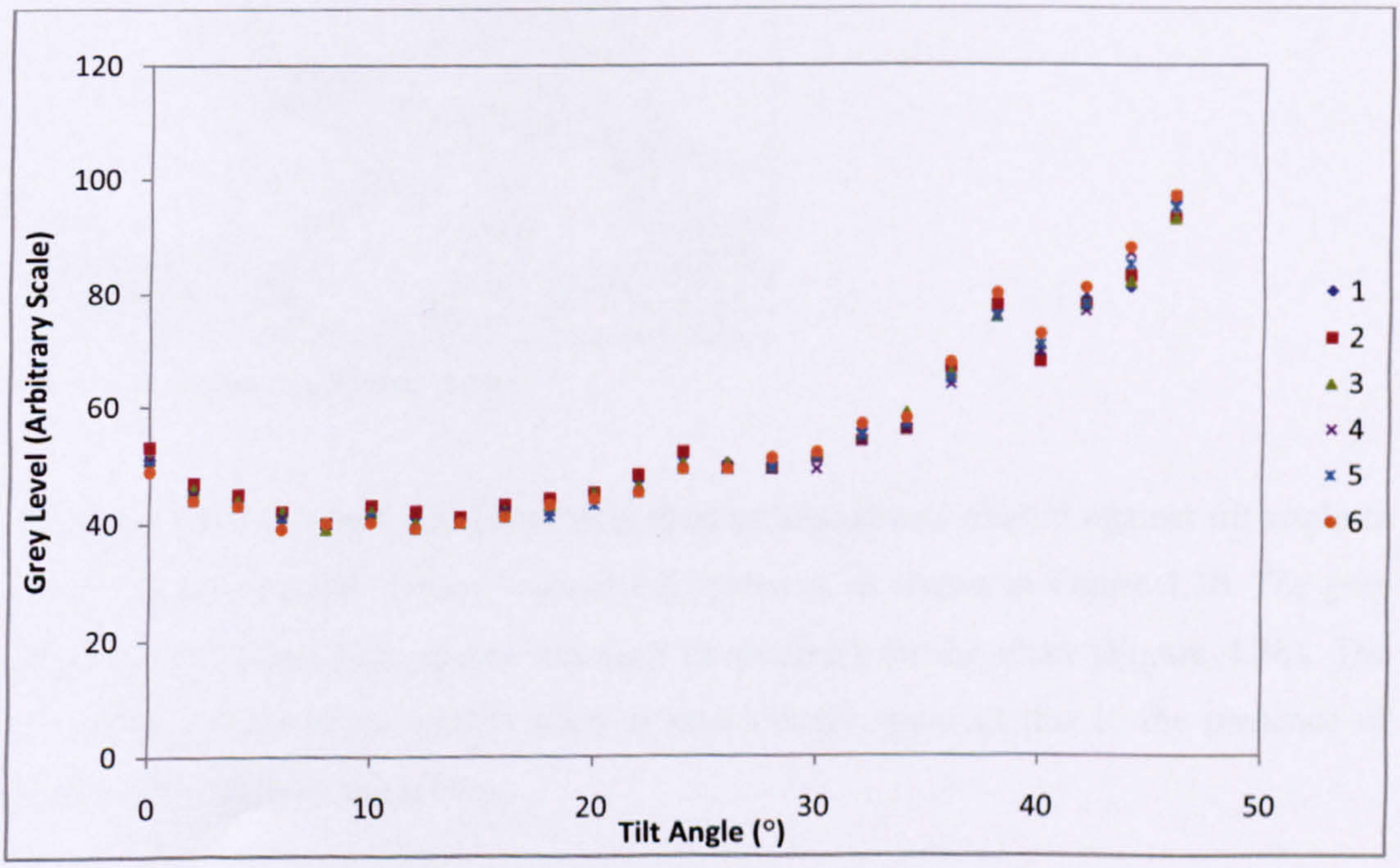


Figure 4.36 - Variation in grey level of SiC particles with tilt angle

In order to interpret all of the micrographs, it was necessary to carry out this normalising procedure for each image by monitoring the grey level variation for an amorphous SiC particle. On completion of this process, the grey levels for each individual grain within a micrograph were plotted against tilt angle. These charts were then compared to reference data from the literature in order to determine relative grain orientations within the samples.

The following figures offer an example of this procedure and compare the non-corrected and corrected grey level charts for the indexed aluminium grains. In Figure 4.37 the micrograph for the area of interest is labelled with SiC particles being assigned numbers and aluminium grains being assigned letters.

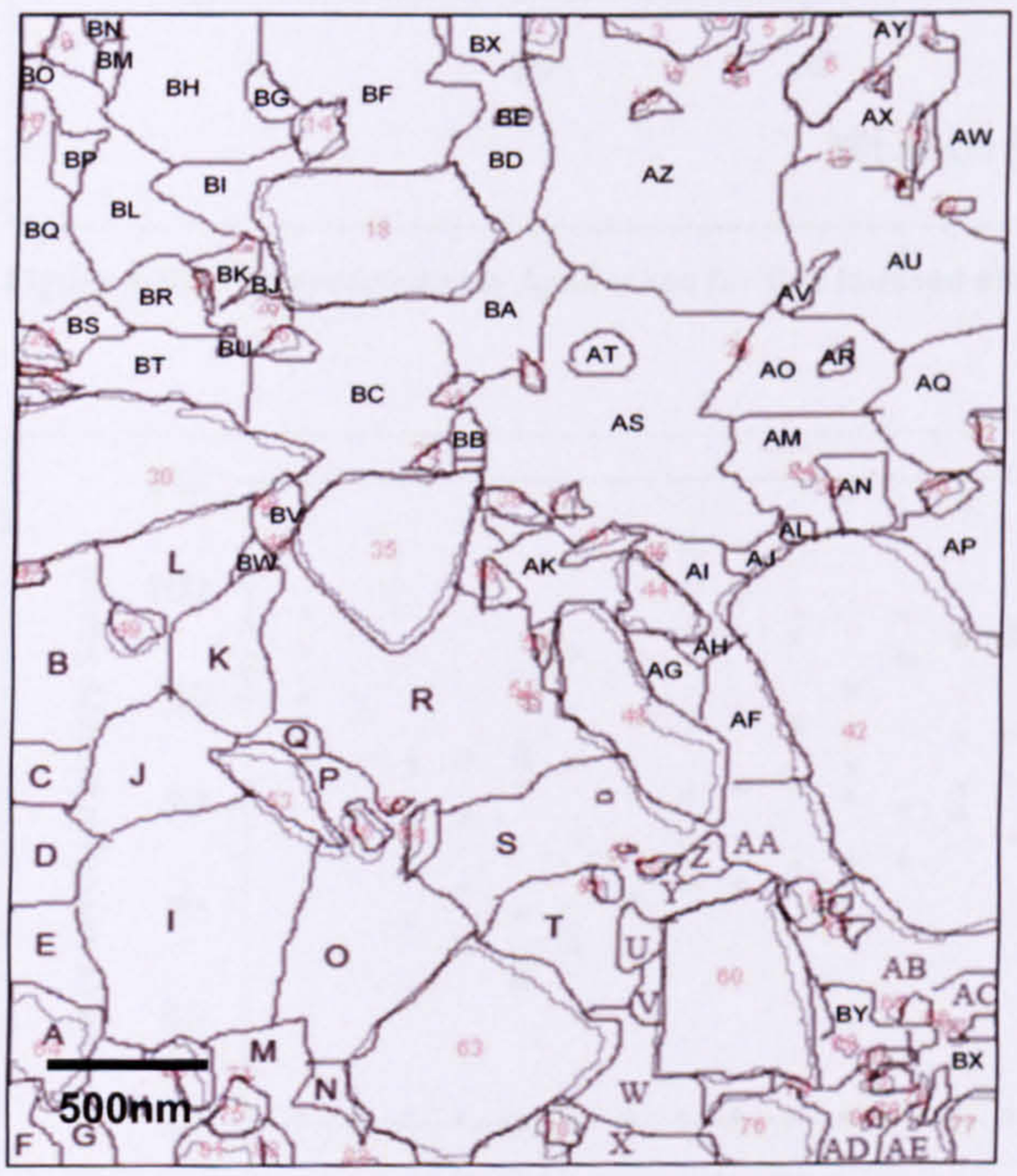


Figure 4.37 - Indexing of microstructure

The grey level for each SiC particle is then measured and plotted against tilt angle to permit the subsequent "image normalising" process, as shown in Figure 4.36. The grey levels of the aluminium grains can then be overlaid on the chart (Figure 4.38). The crystalline nature of the matrix alloy is now clearly apparent due to the presence of peaks and troughs in the curves.

Finally, the grey levels can be corrected to account for the gradual brightening of the image during the tilting process. The normalised curves achieved in Figure 4.39 offer a more accurate indication as to the degree of ion channelling occurring during the tilting process.

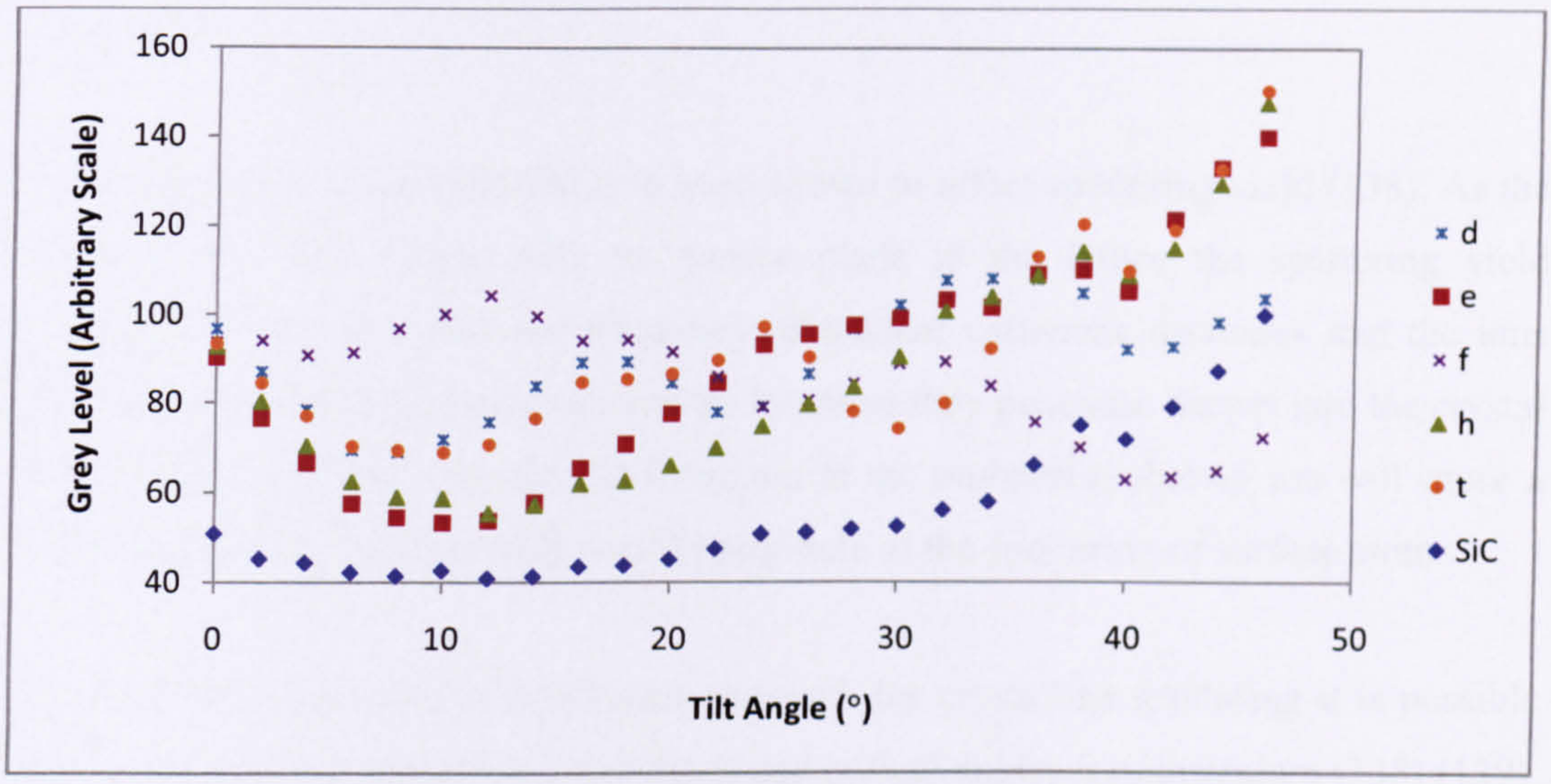


Figure 4.38 - Uncorrected grey level maps for five indexed aluminium grains

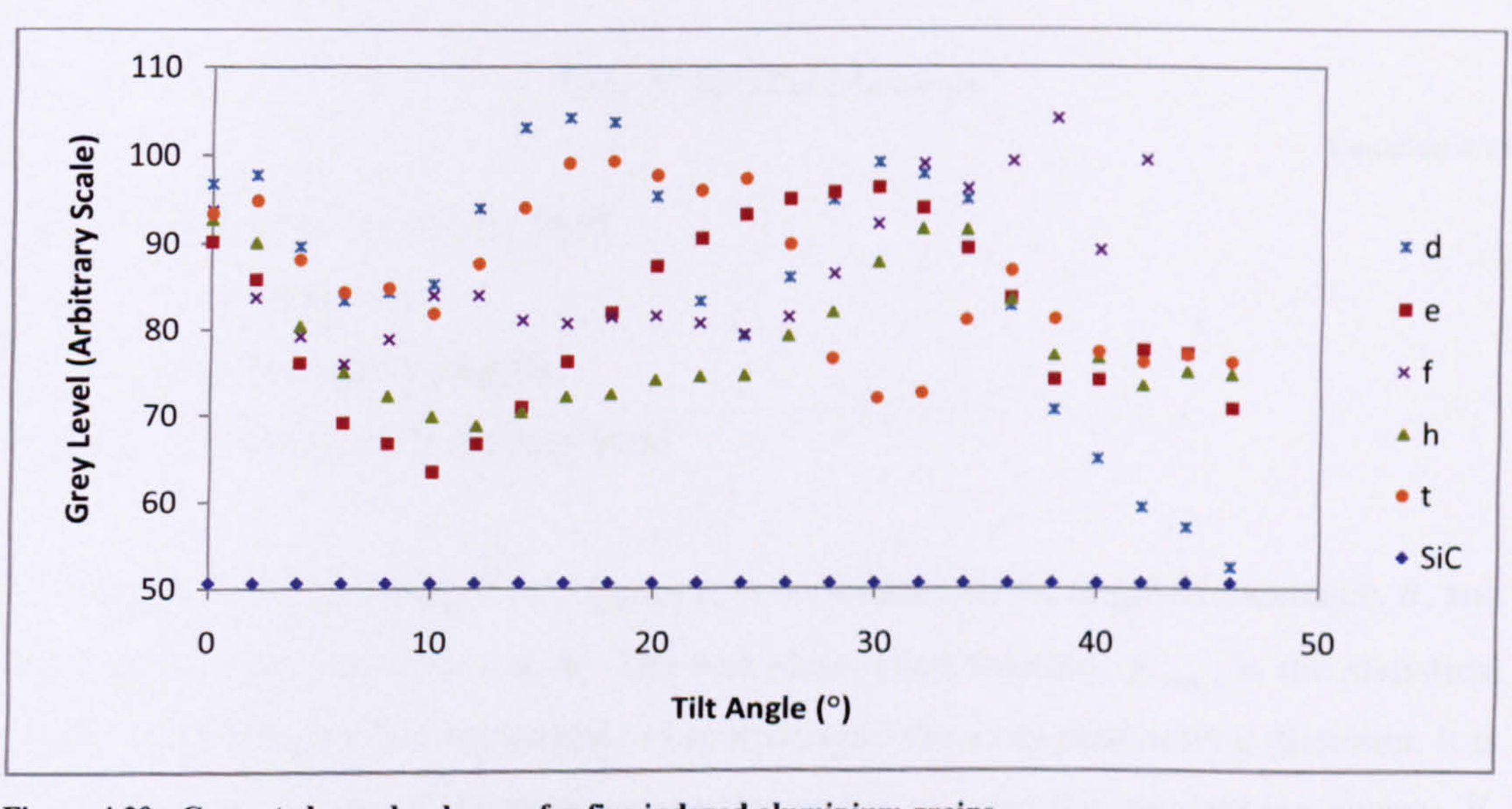


Figure 4.39 - Corrected grey level maps for five indexed aluminium grains

The next stage was to determine the theoretical ion channelling efficiency of the grain structure based on theoretical calculations to take into account the crystallographic characteristics of the material. If successful, the experimental data could be compared with the theoretical values and grain orientation data could be quantified.

The ion channelling phenomenon in polycrystalline specimens has been widely reported and is well understood (136) (137). Ion channelling occurs because the yield of secondary electrons varies with crystallographic orientation. If a specific grain is aligned with an atomic plane parallel to the incident beam, channelling will be effective and the grain will appear dark due to the relatively low levels of secondary electrons emitted.

Crystallographic orientation has also been shown to affect sputtering yield (138). As the incident ion beam aligns with an atomic plane in the lattice the sputtering yield decreases. This is because the frequency of nuclear collisions decreases and the ions predominantly undergo electronic energy losses as they penetrate deeper into the crystal lattice. The net effect is an overall reduction in the probability that an ion will cause a collision cascade, which in turn would contribute to the sputtering of surface atoms.

By using the Lindhard-Onderdelinden approach for crystalline sputtering it is possible predict the primary channelling directions and critical angles for aluminium (138) (139). This model was developed and refined by Palmer et al. (140).

$$Y_{uvw} = \eta_{hkl} \chi_{uvw} Y_{amorph}$$

Equation 4.11

Y_{uvw} – Channelled sputtering yield

η_{hkl} – Fitting parameter

χ_{uvw} – Non-channelled fraction

Y_{amorph} – Amorphous sputtering yield

The amorphous sputtering yield, Y_{amorph}, is dependent on the angle of incidence, θ, and the energy of the incident ion, E. The non-channelled fraction, χ_{uvw}, is the statistical fraction of the beam that contributes to sputtering in the axial channelling direction. It is dependent on the critical channelling angular width, ψ_c, and the incident ion energy, E. It is possible to assume the fitting parameter, η_{hkl}, as unity. The non-channelling fraction at normal incidence, χ^0_{uvw}, can be calculated using the Thomas-Fermi potential for the ion-atom interaction.

$$\chi^0_{uvw} = \pi N t^{3/2}_{uvw} \left[\frac{3A^2 Z_1 Z_2 \left(\frac{e^2}{4\pi\varepsilon_0} \right)}{E} \right]^{1/2}$$

Equation 4.12

The distance between neighbouring atomic positions along the direction $[uvw]$ is t_{uvw}. Charge, e, is 1.6 x 10^{-19}C and the permittivity constant, ε_0 is 8.85 x $10^{-12}C^2/N*m^2$. The non-channelled fraction is also dependent on the atomic number, Z_1, and energy, E, of the incident beam as well as the atomic density, N, and the atomic number, Z_2, of the material under analysis. The Thomas-Fermi screening length, A, can be derived in the following manner.

$$A = \frac{\left(\frac{9\pi^2}{128} \right)^{1/3} \times a_0}{\left(Z_1^{2/3} Z_2^{2/3} \right)^{1/2}}$$

Equation 4.13

The Bohr radius, a_0, required for the calculation of the Thomas-Fermi screening length, can be calculated as follows:

$$a_0 = \frac{\hbar^2}{m_e \frac{e^2}{4\pi\varepsilon_0}} = 0.529177\ \text{Å}$$

Equation 4.14

The channelling directions can now be calculated for an incident ion beam of given energy. Finally, the angular width, ψ_c, of the channelling directions can be calculated:

$$\psi_c = \left[\frac{A^2 Z_1 Z_2 \left(\frac{e^2}{4\pi\varepsilon_0} \right)}{E t^3_{uvw}} \right]^{\frac{1}{4}}$$

Equation 4.15

$$E < E_1 = \frac{2 Z_1 Z_2 \left(\frac{e^2}{4\pi\varepsilon_0} \right) t_{uvw}}{A^2}$$

Equation 4.16

Equation 4.15 is valid providing the energy of the incident ions is less than E_1, which is the upper limit for Lindhard's low energy approximation. This limit has been calculated for a 30 keV Ga^+ ion beam into aluminium as ~2.3 MeV, using Equation 4.16.

Where the incident ion beam is directly channelled through the lattice the non-channelled fraction, χ^0_{uvw}, reaches a minimum. As the tilt angle deviates from normal incidence, the non-channelled fraction increases towards unity as the statistical likelihood for channelling decreases.

The polar angle resolved non-channelled fraction, χ_{uvw}, can be calculated as follows:

$$\chi_{uvw} = \frac{\chi^0_{uvw}}{1-(1-\chi^0_{uvw})\left(\frac{\psi}{f\psi_c}\right)^2}$$

Equation 4.17

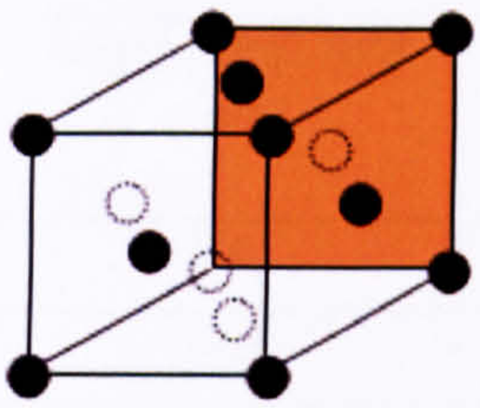
where ψ is the the polar angle from normal incidence along a channelling direction $[uvw]$ and the fitting parameter, f, is included to improve the relationship between the model and the experimental data.

In the literature it has been established that F.C.C. materials demonstrate a fibre texture during the extrusion process, which combines the <111> and <100> textures parallel to the fibre axis (130). For this reason it was decided that a [100] axis would be used as a reference in order to generate a series of ion channelling directions, as this particular direction was likely to demonstrate a significant ion channelling response for metallographic samples prepared perpendicular to the extrusion axis. For each channelling direction, the relative angle from the [100] axis (ϕ), was determined by applying the scalar product technique, as follows:

$$\vec{A}.\vec{B} = AB\cos\phi$$

Equation 4.18

Vector A represents the [100] direction and vector B describes the ion channelling direction. For each of these directions, the non channelled fraction could be determined by application of Equation 4.18. The following schematic, Figure 4.40, illustrates how the ion beam interacts with the lattice as it is tilted through the (100) plane.



(100) Plane

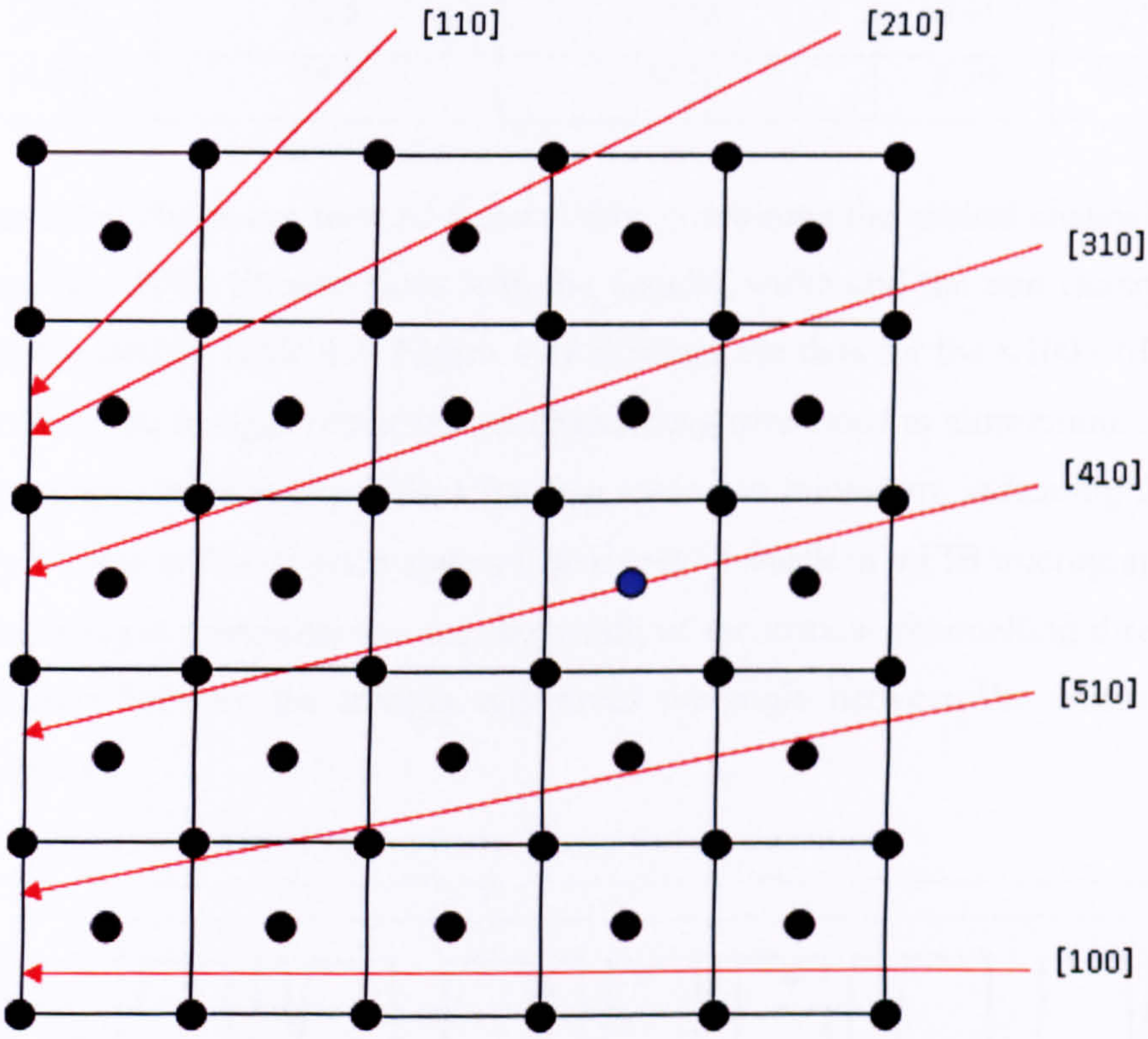


Figure 4.40 - Critical channelling directions in the (100) plane

As shown, depending on the incident angle, the ion beam is impeded to a lesser or greater extent by the relative spacing between atoms perpendicular to the direction of the beam. The relative atomic spacing for a given direction therefore has a bearing on both the sputtering yield and the angular width of a channelling direction. In this particular example, it can be seen that the [410] direction will not permit ion channelling as there is a direct collision with an atom (highlighted in blue). The non channelled fraction, χ_0, for this direction will therefore be unity.

The calculated critical channelling directions and their associated angular widths and non channelled fractions are shown in Table 4.8, below.

Table 4.8 - Angular Width of Critical Channelling Direction, ψ_c, and Non Channelled Fraction, χ_0, <100> axis

Direction	Angle from [100] (ϕ)	30 keV Ga+ into Cu t_{uvw}/a	t_{uvw} (nm)	ψ_c	χ_0
[100]	0.0	1.00	0.41	6.05	0.23
[510]	11.3	2.55	1.03	3.00	0.94
[310]	18.4	1.58	0.64	4.29	0.46
[210]	26.6	2.24	0.91	3.31	0.78
[110]	45.0	0.71	0.29	7.85	0.14

Theoretical charts can now be generated by combining the critical channelling tilt angle along the <100> tilt directions with the angular width and the non channelled fraction data obtained in Table 4.8. Figure 4.41 displays the data for the <100> tilt direction. In this chart, the troughs represent ion channelling directions in aluminium. At the base of each trough, the non channelled fraction reaches a minimum, indicating that sputtering rates are low and so a grain appears dark grey or black in a FIB micrograph. The width of the troughs represents the angular width of the critical channelling direction and the separation between the troughs represents the angle between the critical channelling directions.

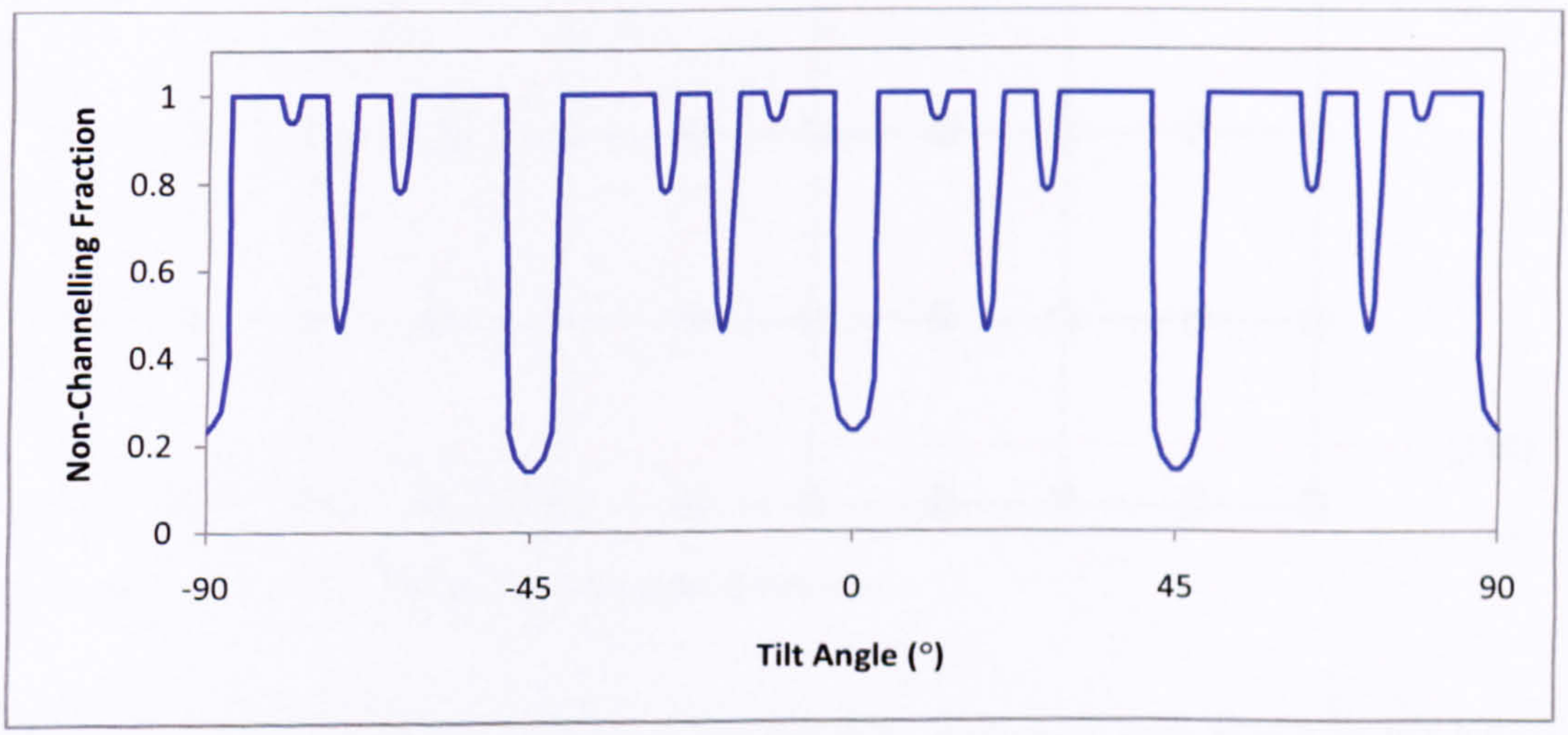


Figure 4.41 - The dependence of non-channelling fraction on tilt angle along the <100> tilt directions

The same technique can also be applied to the <110> tilt axis in order to determine critical channelling directions and associated angular widths and non channelled fractions. Again, the schematic in Figure 4.42 is provided to illustrate the path of the ion

beam through the lattice and the relative inter-atomic spacing for any given direction in the lattice.

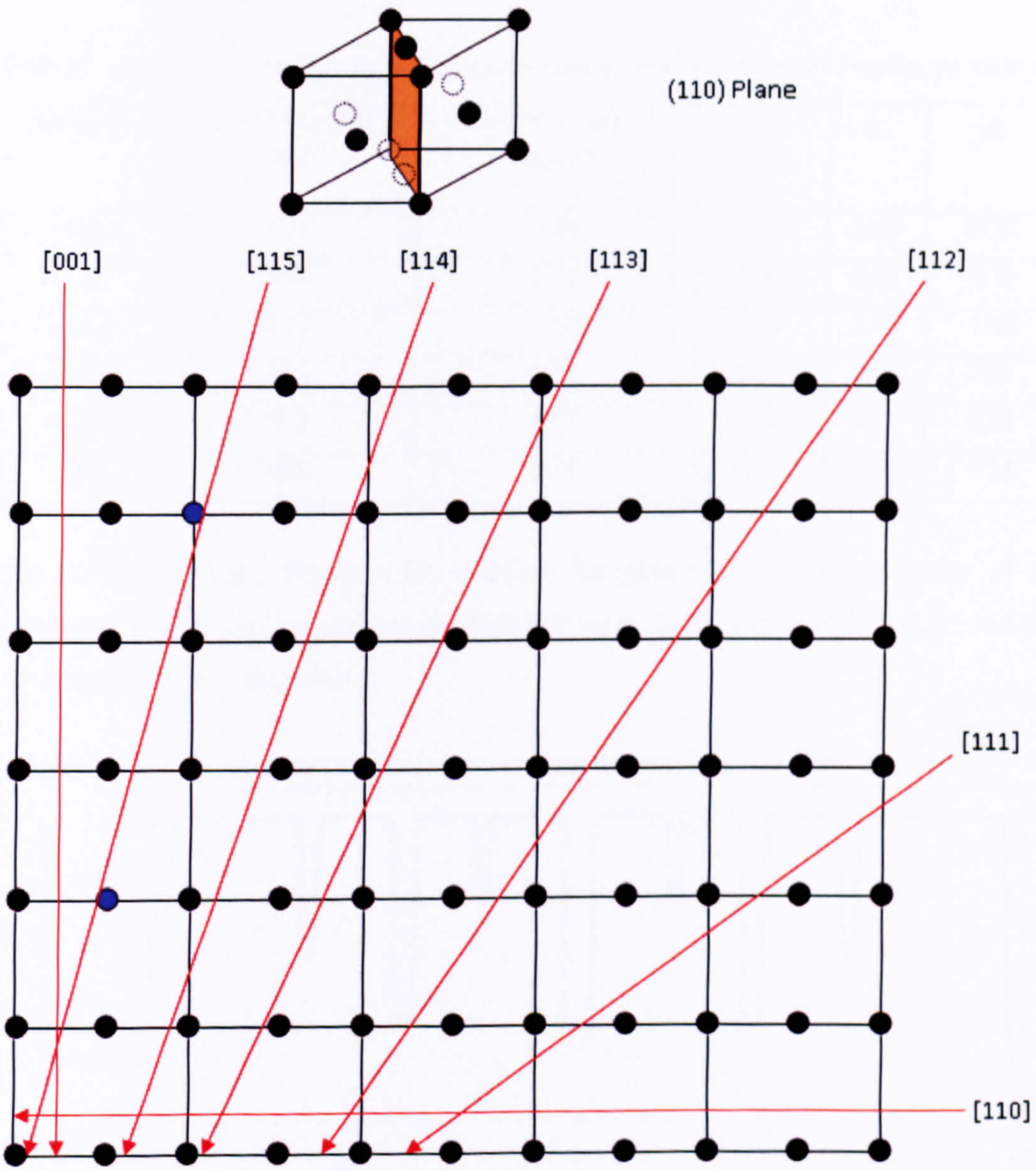


Figure 4.42 - Critical channelling directions in the (110) plane

For this orientation the [115] path is restricted by collisions with atoms in the lattice (indicated in blue) so the sputtering yield is relatively high and the non channelled fraction is unity. The schematic suggests that the non channelled fraction is likely to be highest for the [110] direction, where the relative separation between neighbouring atoms is greatest. This hypothesis is confirmed by the calculated theoretical data in Table 4.9, which shows a minimum non channelled fraction value, χ_0, of 0.14 for the

[110] direction. As the beam is tilted, the angle, ϕ, relative to the [001] direction increases and a range of non channelled fractions are observed, depending on the direction-specific inter-atomic spacing.

Table 4.9 - Angular Width of Critical Channelling Direction, ψ_c, and Non Channelled Fraction, χ_0, <110> axis

Direction	Angle from [001] (ϕ)	30 keV Ga+ into Cu t_{uvw}/a	t_{uvw} (nm)	ψ_c	χ_0
[001]	0.0	1.00	0.41	6.05	0.23
[114]	19.5	2.12	0.86	3.44	0.72
[113]	25.2	3.32	1.34	2.46	1.40
[112]	35.3	1.22	0.50	5.20	0.31
[111]	54.7	1.73	0.70	4.01	0.53
[110]	90.0	0.71	0.29	7.85	0.14

The following chart, Figure 4.43, displays the data for the <110> family of tilt directions. Significant troughs are predicted to occur at tilt angles of 0°, 35.5° and 90° relative to the [001] direction.

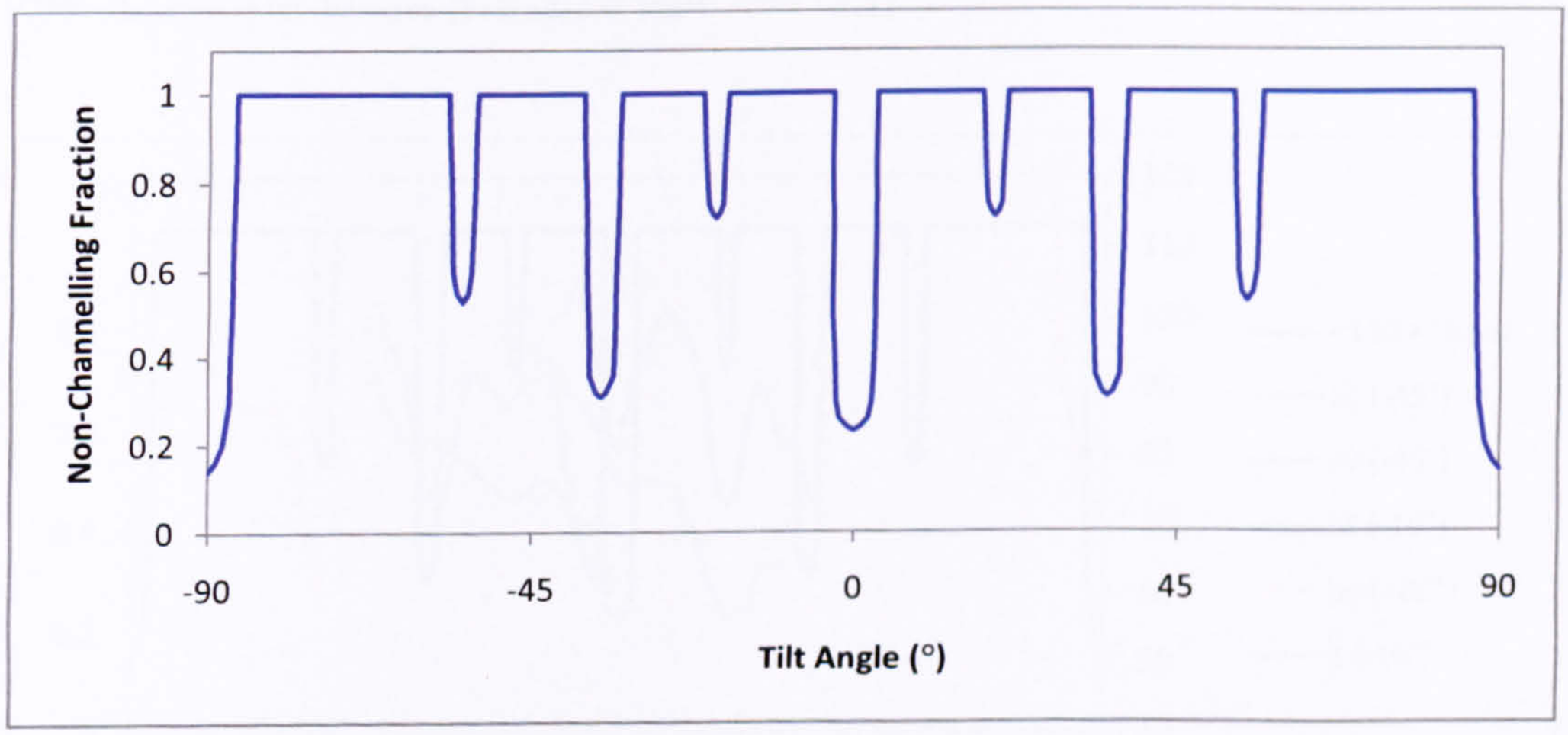


Figure 4.43 - The dependence of non-channelling fraction on tilt angle along the <110> tilt directions

It is now possible to compare the charts in Figure 4.41 and Figure 4.43 to the grey level data obtained for the indexed grains in an attempt to find a match and identify specific grain orientations. Figure 4.44 and Figure 4.45 show a correlation between several grains indexed on the FIB microscope for a specimen extruded at 550°C, imaged in a perpendicular sense to the extrusion direction. The legends in both charts indicate which

grains each individual curve corresponds to, as indexed in Figure 4.37. The theoretical baseline curves are for the <100> and <110> tilt axes, respectively. In general, the critical channelling directions are consistent with the model, although the angular widths of the critical channelling directions and trough depths are not consistent. This could be due to current limitations in the technique as well as microstructural discrepancies from the theoretical model assumptions.

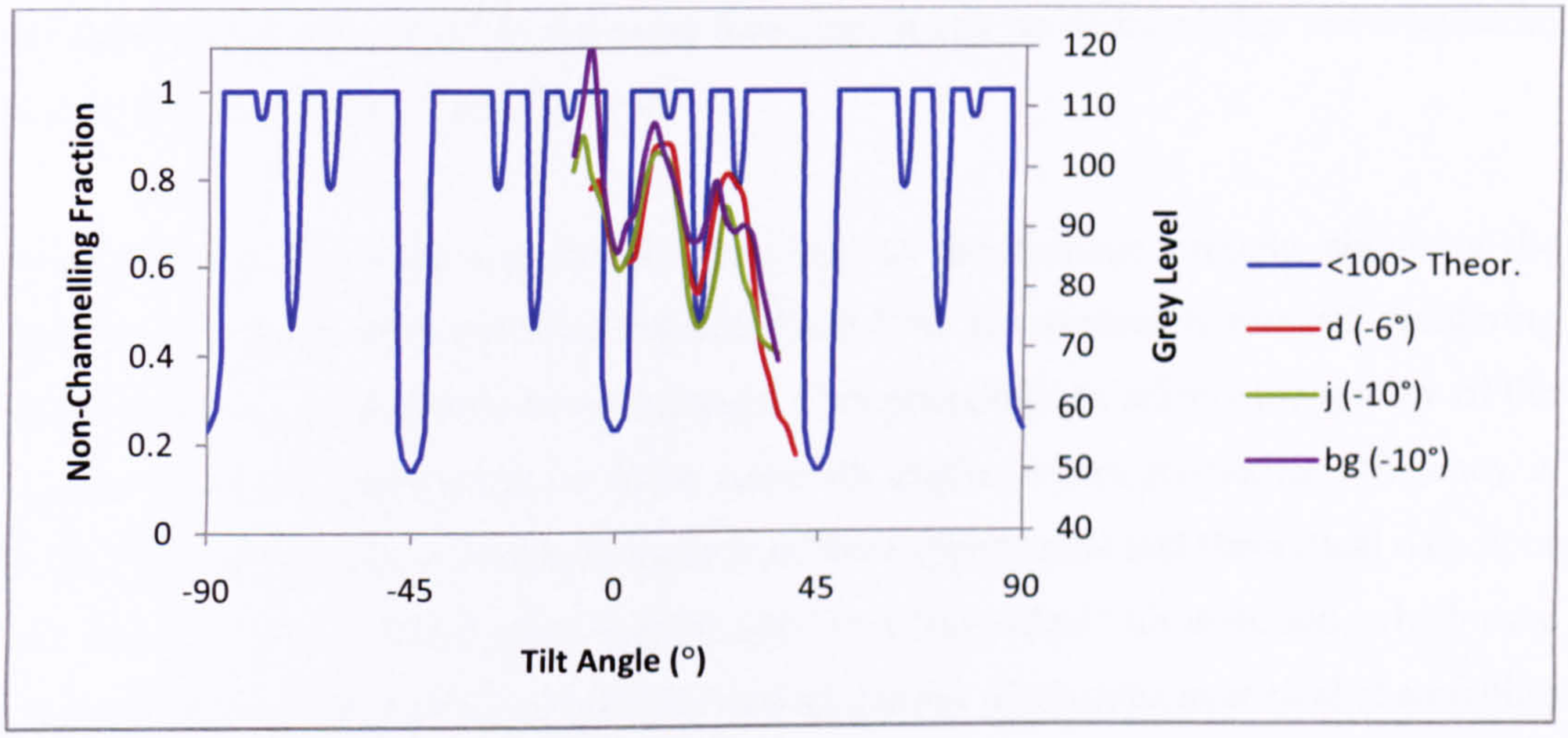


Figure 4.44 - Normalised grey level versus incident ion beam angle for a series of grains of AMC225xe, cf. <100> theoretical tilt direction (Extruded at 550°C / 20:1 / E-T)

Figure 4.45 - Normalised grey level versus incident ion beam angle for a series of grains of AMC225xe, cf. <110> theoretical tilt direction (Extruded at 550°C / 20:1 / E-T)

A positive match was identified if a dataset for an individual grain achieved the following criteria. At least three troughs in the grey level variation plot showed agreement within 2° of corresponding troughs on the theoretical curves.

The legend in Figure 4.44 shows the angle through which an individual grain has been rotated in order to satisfy the model, based on the above criteria. It can be seen that grain "d" was rotated by 6° to satisfy the model. This would indicated that the [001] direction was approximately 6° off the imaging direction, which in this case is also the direction of extrusion. Additionally, "j" and "bg" were rotated by 10°, which means their [001] directions were orientated at 10° to the direction of extrusion. Finally, since all three grains were tilted in the same direction, it can be deduced that the orientation discrepancy between "j" and "d" is 4°.

Limitations in the technique mainly arise due to the damage brought about by the repetitive imaging of the area of interest. Each time the surface is imaged, sputtering damage occurs, even at low beam currents. This phenomenon affects the quality of the images produced, particularly at more acute tilt angles where sputtering efficiency is retarded. Additionally, manual comparison of the experimental and theoretical data does not cater for the fact that a grain may be tilted in a "non-ideal" tilt direction, which may prevent satisfactory correlation with theoretical curves. Variations in critical channelling angles may be due to the fact that data points were recorded at 2° increments, so the resolution is not sufficient to define the more subtle features of the curves.

With respect to microstructural discrepancies, the model is based on a defect free aluminium lattice, whereas the material under study is significantly different in many respects. For example, the presence of alloying elements in solid solution, intermetallics, semi-coherent strengthening precipitates, residual stress and dislocations structures will each have varying degrees of influence of the ion channelling efficiency.

The problems associated with the accuracy of the theoretical model can be partially overcome by producing a three dimensional model, by means of a stereographic projection based upon the axial channelling direction data and the angular widths of the channelling directions. This would necessitate the indexing of all of the tilt directions for a defect-free grain of aluminium.

By drawing straight lines across the stereographic projection and comparing to the peaks and troughs in the experimental data obtained during grain indexing it will be possible to determine the specific orientation of an individual grain. The main barrier to

achieving this goal is the potential for "multiple matches" for a specific grain. It is postulated that this problem can be avoided by indexing grains in at least two different tilt directions, for example in perpendicular planes. This should offer clarification as to the specific grain orientation.

Despite the somewhat limited scope of the current technique it was still possible to ascertain a significant amount of grain orientation data as well as relative grain orientation information for AMC225xe extruded at the three different temperatures. This analysis was carried out on three samples for each extrusion condition in the extrusion-transverse direction. Many grains that were oriented in an ion channelling direction at normal beam incidence were identified based on their associated ion channelling directions as the beam was tilted. This was achieved by comparison with the relative locations of the channelling troughs for the theoretical <100> and <110> tilt directions. A positive match was taken to be an indexed grain that showed a channelling direction discrepancy with the theoretical data of less than 6°. This allowance was made due to the difficulty in controlling the precise milling angle, relative to the extrusion direction, during the specimen preparation stages. Where a positive match was identified, the off-axis angle was calculated based on the angle through which the grain was rotated in order to satisfy the model. The data from samples for each extrusion condition is summarised in Table 4.10.

By applying this technique it was possible to identify the grain orientation for approximately 50% of the grain/subgrains that were observed in each micrograph.

Table 4.10 – Grain orientation data for extrusion-transverse direction extracted from FIB micrographs

	350°C		450°C		550°C	
Tilt Axis	<100>	<110>	<100>	<110>	<100>	<110>
Total no. of grains available for indexing	371		341		266	
Grain/Subgrains showing positive match	102	131	76	90	68	65
Channelling Direction	Relative Abundance					
[110]	12%	10%	11%	4%	8%	14%
[001]	18%	7%	23%	7%	**34%**	**11%**
[211]	-	2%	-	5%	-	2%
[310]	3%	-	4%	-	2%	-
[111]	-	**36%**	-	**38%**	-	21%
[411]	-	2%		1%	-	1%
[210]	4%	-	1%	-	2%	-
[510]	7%	-	6%	-	5%	-
[311]	-	-	-	-	-	-

The total number of indexed grains in each tilt axis is displayed on the table, together with the total number of grains observed in the micrographs. It can be seen that the number of grains available for indexing decreased with increasing extrusion temperature due the average grain size increasing within a constant surface area. The values given in the table for each channelling direction and extrusion condition indicate the relative contribution of a specific grain orientation as a percentage of the total number of grains that were able to be positively identified.

None of the individual grains indexed showed a positive match in both the <100> and <110> tilt axes, so the figures for a specific orientation for a given extrusion condition can be combined from both columns if they each contain data. For example, the table indicates that of the grains that could be indexed for the material extruded at 350°C (~63% of the total number of grains observed in the micrographs), approximately 25% were orientated in the [001] lattice direction, relative to the extrusion axis. Additionally, 36% of the grains were orientated in the [111] direction.

The table suggests that following extrusion at 350°C and 450°C, the predominant grain orientation is [111] at 36% and 38% relative abundance, respectively. At 550°C, the relative contribution of the [100] direction increases to 45% at the expense of the [111] direction, which shows a relative abundance of just 21%. This data is in broad agreement with the macro texture data obtained through XRD analysis.

The most attractive feature of the current FIB microstructural analysis technique is to determine specific and relative grain orientations within a selected area of the microstructure. This will contribute to the understanding of the influence of SiC particles on the substructure during processing. Selected examples have been included to permit general comments on the microtextural details of AMC225xe and the likely influence of extrusion temperature variation on such features.

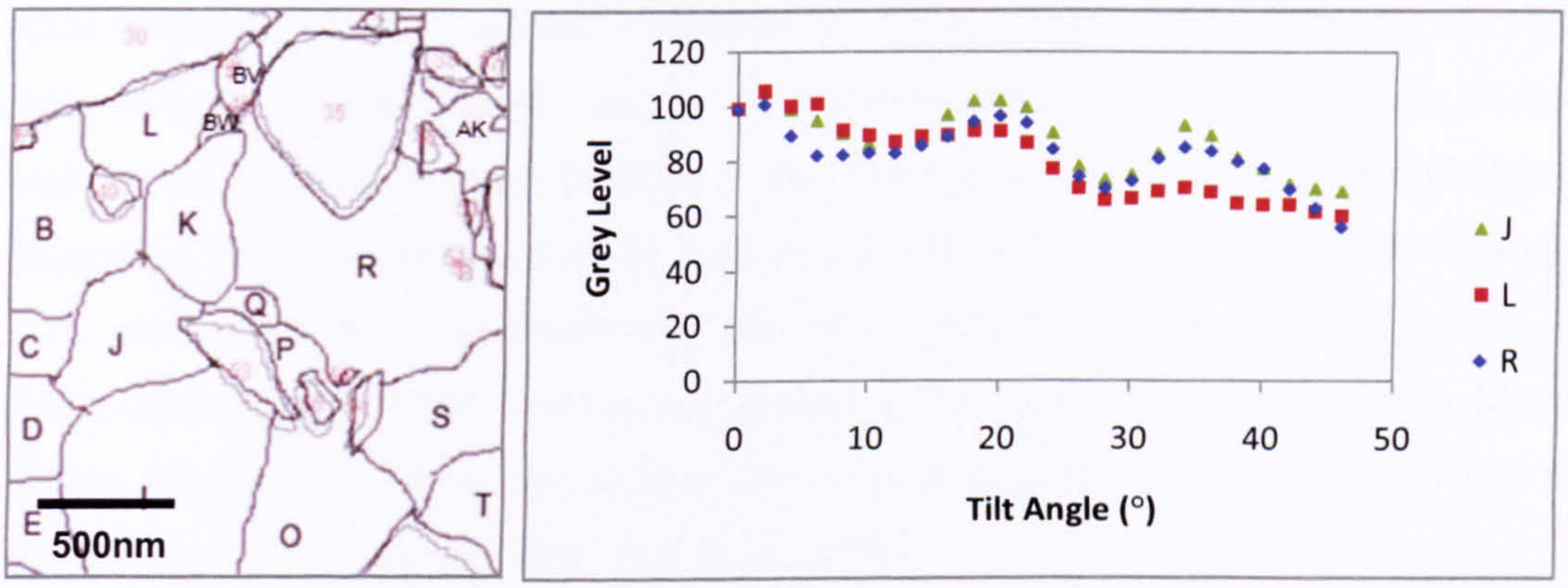


Figure 4.46 - AMC225xe indexed grains and corresponding FIB tilt data (Extruded at 550°C / 20:1 / E-T)

Figure 4.46 shows grain boundaries and SiC particles in a small region of the microstructure of AMC225xe extruded at 550°C. Grains are designated by letters and SiC particles by numbers. The corresponding chart shows the variation in grey level with tilt angle of three of the non-neighbouring grains found in the microstructure. As can be seen, all three grains show similar channelling angles and channelling widths, indicating that they are identically orientated grains within the microstructure. By comparison with the theoretical curves in Figure 4.44 and Figure 4.45 it can be seen that these grains are in fact orientated in the <100> direction.

Figure 4.47 shows the grey level comparison for two neighbouring indexed grains. As can be seen in the chart, the grains are out of phase by approximately 2°, which confirms that the grain boundary separating them is of the low angle type.

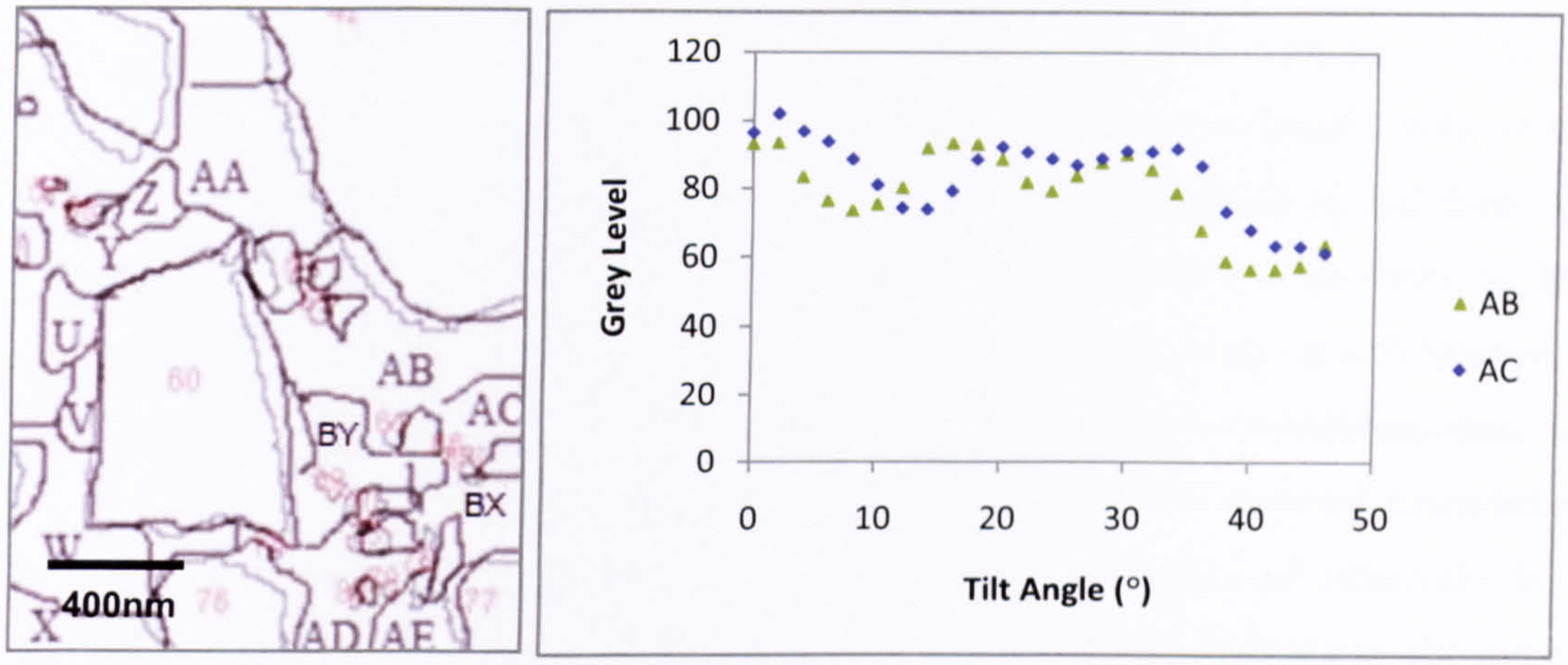


Figure 4.47 - AMC225xe indexed grains and corresponding FIB tilt data (Extruded at 550°C / 20:1 / E-T)

In general, low angle grain boundaries were not widely observed within the microstructure of the material extruded at 550°C, even within regions of high reinforcement interparticulate spacing. Of the indexed microstructural regions in this sample, the majority of grain boundaries were discovered to be of the high angle type, indicating that a subgrain structure was not developed during secondary processing. This observation was consistent with the TEM analysis (Section 4.8: Focussed Ion Beam Milling as a TEM Specimen Preparation Technique for an Aluminium Metal Matrix Composite), which also showed the presence of high angle grain boundaries in the material at extruded at 550°C (see Figure 4.50).

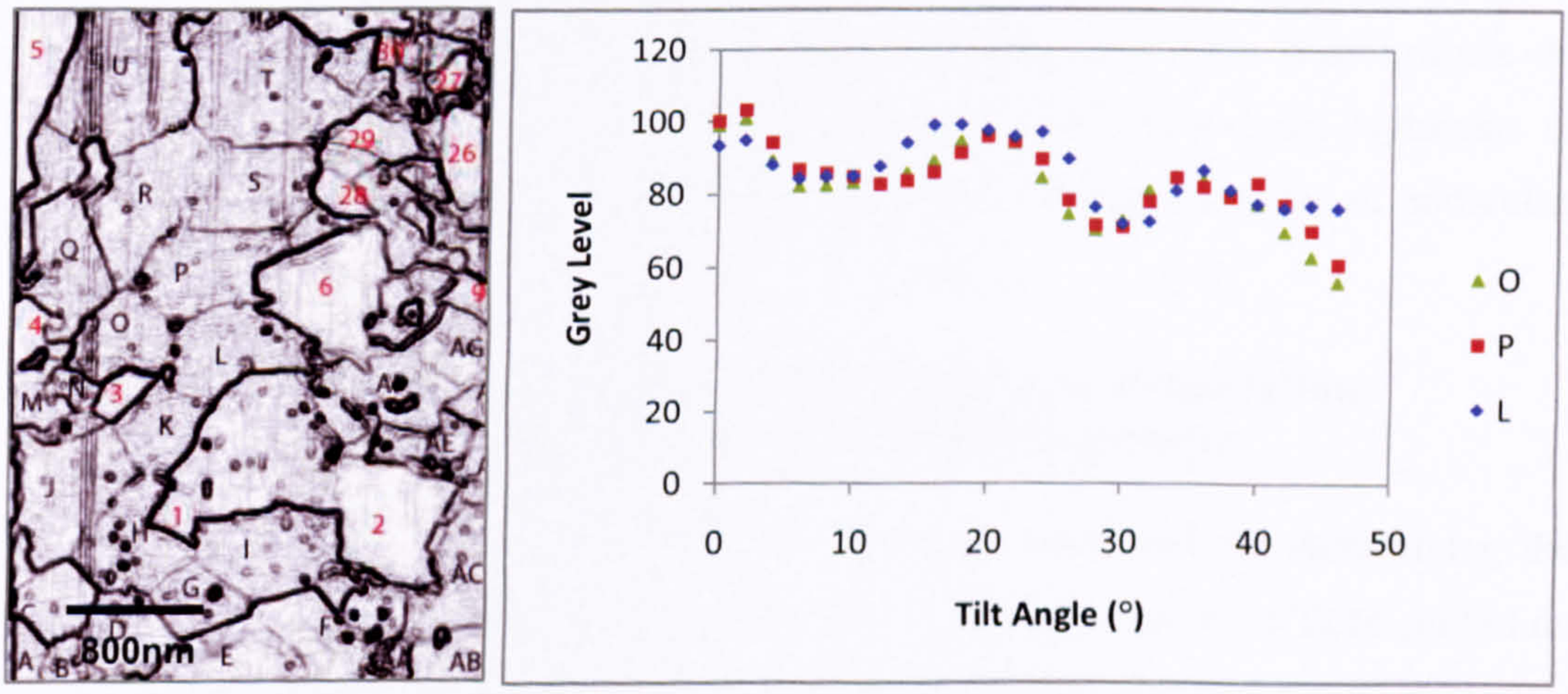


Figure 4.48 – AMC225xe indexed grains and corresponding FIB tilt data (Extruded at 350°C / 20:1 / E-T)

Figure 4.48 shows the grey level data for three adjacent grains in a sample of material extruded at 350°C. Interestingly, the channelling directions appear to be at approximately the same tilt angles for all three of the indexed grains, with minor differences in the angular widths. In this case the logical conclusion is that these are neighbouring subgrains. The grain boundary angles between each grain must be less than 2° as the tilt angle increment of 2° was not subtle enough to detect a difference in the orientation of the grains. In general, there were more subgrain boundaries observed in the material extruded at 350°C and 450°C compared to the material extruded at 550°C. Subgrain structures were particularly evident in regions of relatively high reinforcement interparticulate spacings. These observations add credence to the notion that a reduction in temperature during thermomechanical work promotes the development of a substructure and such recovery processes are less likely to occur at 550°C. For the material extruded at 350°C and 450°C, although low angle grain boundaries were observed in regions of relatively low particle reinforcement density, high angle grain boundaries were seen in regions within close proximity to the SiC particles. This may be as a result of subgrain rotation due to relaxation of deformation induced primary dislocation structures. This finding is consistent with the literature (111).

Overall, the FIB grain indexing process has proven to be a highly useful analysis tool for the microstructural characteristation of the MMC. Not only has the existence of a prevalent fibre texture detected during XRD analysis been confirmed but also, the existence of low angle grain boundaries has been identified. This demonstrates the method as a very sensitive technique for analysing microtextures and highlights its potential as an alternative method to EBSD for grain structure analysis of particulate reinforced MMCs.

4.8 Focussed Ion Beam Milling as a TEM Specimen Preparation Technique for an Aluminium Metal Matrix Composite

Transmission electron microscopy (TEM) is a widely used tool for determining the crystallographic and chemical nature of materials. A general scarcity of TEM studies on metal matrix composites can be attributed to the difficulties associated with preparing an electron transparent specimen. The required specimen thickness for electron transparency is typically less than 100 nm but is dependent on material density (75).

Several conventional techniques are available for the preparation of TEM specimens. There are, however, certain shortcomings associated such techniques for the preparation of TEM discs from metal matrix composites, most notably the issue of non-uniform thinning. In order to carry out a detailed analysis of the matrix/reinforcement interface by TEM, it is necessary to ensure that both phases are of approximately equal thickness and electron transparent. Conventional techniques such as electropolishing tend to preferentially thin the matrix in preference to the reinforcement due to the softer nature of the matrix. This permits a limited amount of analysis of the matrix but prohibits any detailed study of near-interface and interface regions due to electron blanking and scattering (see Figure 4.49 and Figure 4.50).

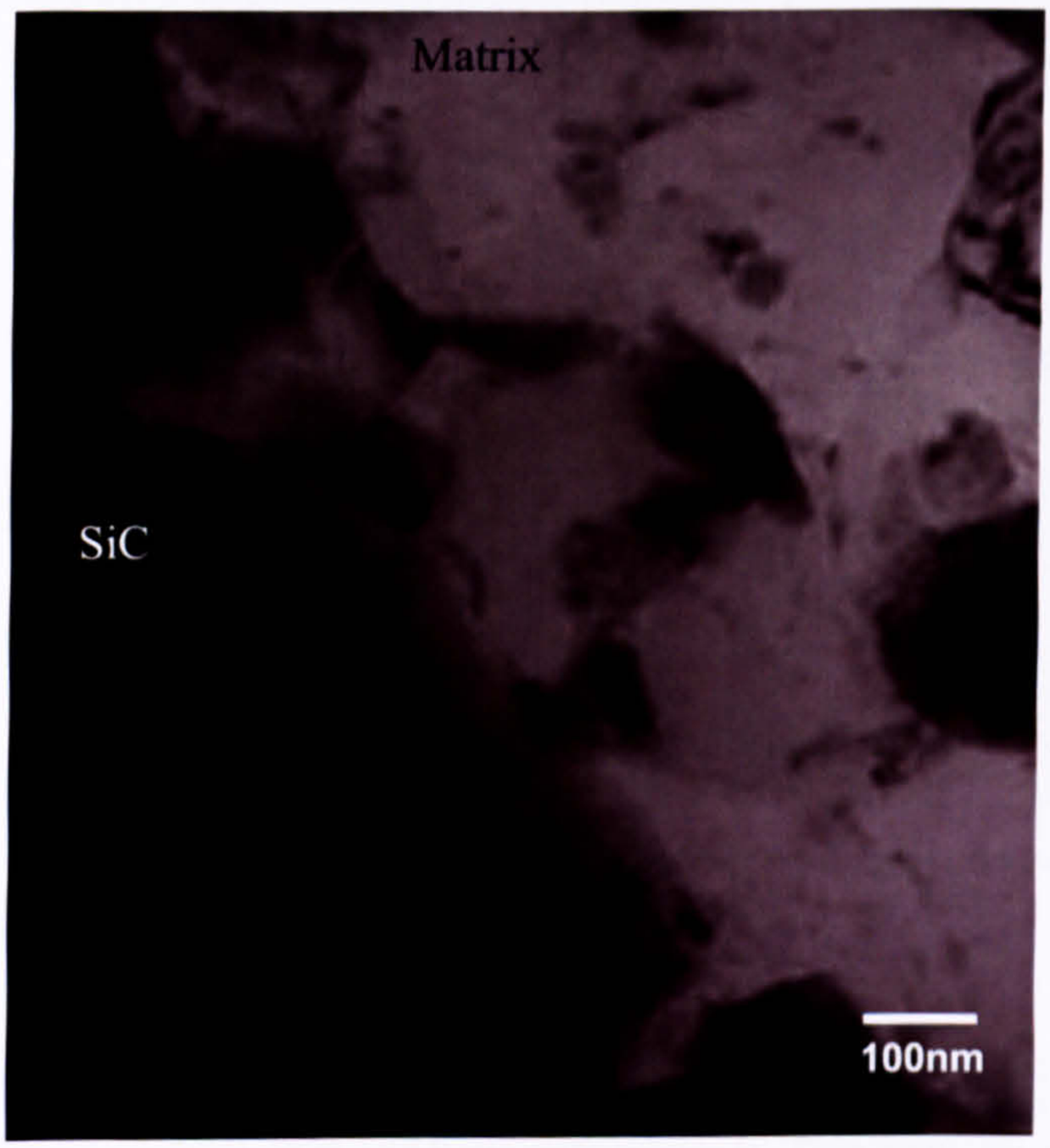


Figure 4.49 - The non-uniform thinning of reinforcement (SiC) and matrix (AA2124), with 'shadowing' effect at matrix/reinforcement interface (extruded at 550°C / E-T / 20:1)

On inspection of specimens prepared by the conventional electropolishing technique it was clear that regions with relatively low reinforcement particle density were well-thinned, but the matrix/reinforcement interfaces were not sufficiently thin for transmission of electrons so a clear image could not be obtained within these regions.

The figure, below, (Figure 4.50) shows a lower magnification bright field image of a "representative" region of the microstructure for a specimen prepared by

electropolishing. Despite not being able to analyse the matrix/reinforcement interfaces, it was possible to obtain selected area diffraction patterns of various grains within the matrix and these data confirmed the existence of high angle grain boundaries. The discovery of high angle grain boundaries in the material extruded at 550°C is consistent with the microtexture analysis performed in Section 4.7: Microtexture Analysis by Focussed Ion Beam Microscopy, where the majority of grain boundaries were determined to be of the high angle type, both in close proximity to SiC particles and within regions of relatively low reinforcement density.

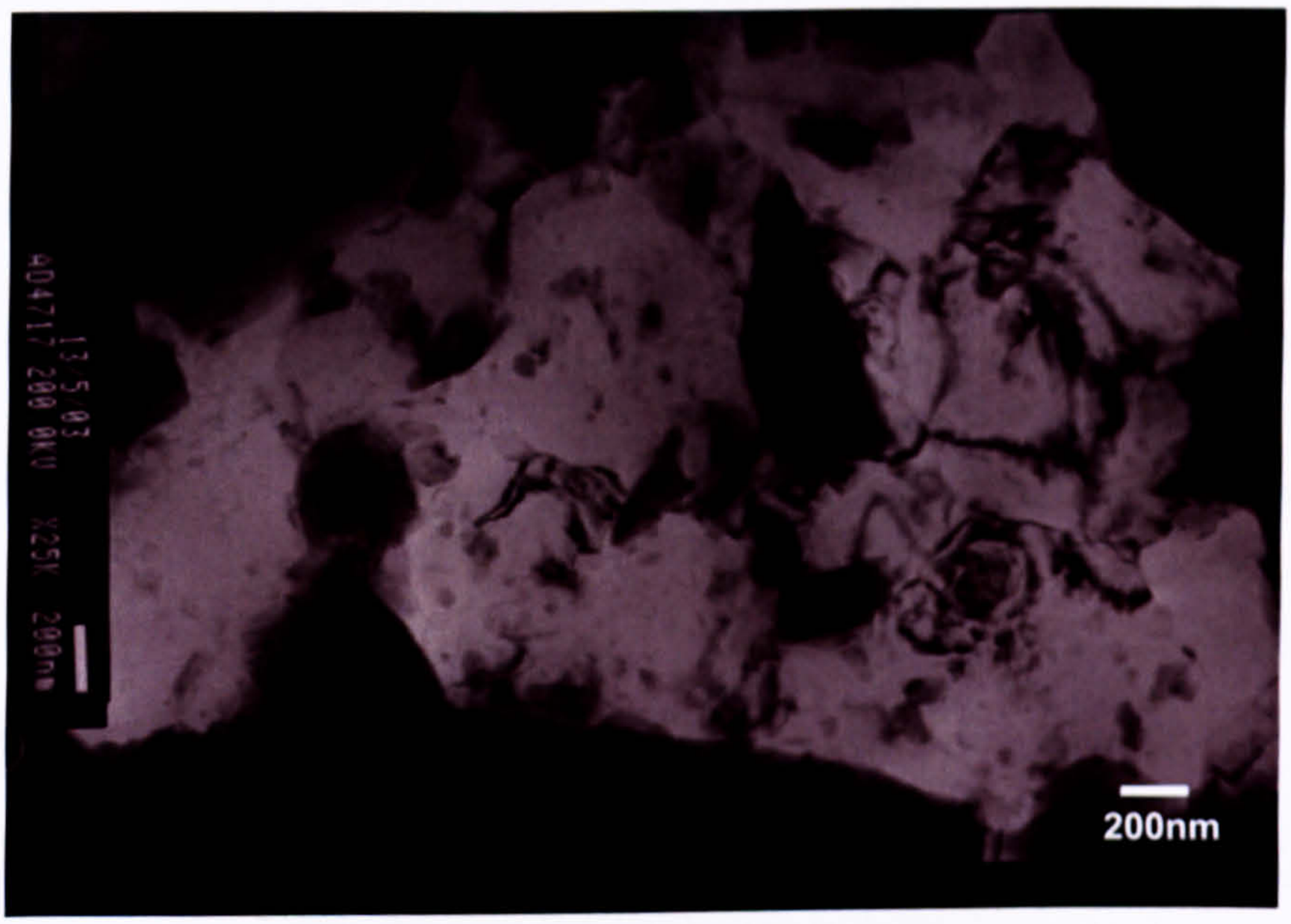


Figure 4.50 - Bright field image of "representative" region of microstructure showing high angle grain boundaries (extruded at 550°C / E-T / 20:1)

Based on the limitations associated with the conventional specimen preparation techniques it was deemed necessary to establish an alternative preparation technique that would permit site-specific TEM analysis of the MMC, including matrix/reinforcement interface studies.

Several previous studies have involved taking an electropolished disc and subjecting both surfaces to a low energy / low angle ion beam in order to remove the protrusions from the reinforcement phases. This technique has offered a degree of success, even for MMC specimens, but significantly increases the overall time taken to prepare a uniformly thinned electron transparent specimen (10).

Other researchers have taken the approach of using a low energy focussed ion beam to 'mill' an electron transparent section of MMC from bulk material. Typically, this section would be approximately 10 μm x 10 μm and 50 nm thick. After milling, the specimen is lifted out of the bulk material and mounted on a copper grating making it suitable for analysis in the TEM. This technique is known as 'lift-out' (11) (81). By this method, it has been possible to achieve uniformly thin sections. There are however, several disadvantages to this approach. Firstly, prior to removal from the FIB microscope, the thickness of the specimen must be measured using image analysis tools built into the equipment. This is an optical approach and therefore is prone to software and user errors. If the section is too thick it will not be electron transparent and is therefore unsuitable for TEM analysis. Once specimens have been removed from bulk material, it is not possible to carry out further milling by FIB. Additionally, the lift-out technique carries inherent risk as it involves contact with a needle in order to transfer the slide to the copper grating. It is therefore possible to induce mechanical damage on the specimen, which may significantly alter the appearance of the microstructure in the TEM. The main advantage of the approach is that it permits uniform thinning in a selective area. It is relatively rapid and not labour-intensive as it is possible to set up automated scripts within the software that will allow the majority of the milling process to proceed unattended.

The technique adopted in the current study involved the preparation of an 'H-Bar' specimen from bulk material, which was originally adopted as a technique for TEM specimen preparation in the semiconductor industry (77) (79) (80) (141). In an unpublished report, a method was developed for preparing an H-Bar specimen from an Al-Cu-Mg powder metallurgical alloy (84). This method was chosen as conventional techniques had proven unsuccessful due to the level of porosity observed in the alloy. The study demonstrated how an electron transparent section could be prepared by the FIB milling and polishing of a 3 mm diameter 'half-disk' specimen with an initial thickness of 30 μm. After preparation on the FIB equipment, the disk was mounted on a copper ring to provide extra strength and then inserted into the TEM. If the specimen was found to be non-electron transparent on inspection, it was possible to remove the specimen and continue thinning on the FIB until electron transparency was achieved. This dramatically reduced overall preparation time and increased the chances of achieving a viewable specimen.

For the current study, in the first instance an attempt was made to apply the same technique for preparing electron transparent specimens from the MMC. A Struers Acutom with a diamond wafer saw was used to cut slices approximately 1 mm in thickness. From these slices, 3 mm diameter disks were produced by a spark erosion technique. The disks were ground on 1200 SiC paper to a thickness of approximately 150 μm. The disks were then mounted onto a steel support using thermosetting adhesive. A Gatan Disc Grinder was used to dimple the centres of the disks to a final thickness of approximately 50μm thickness. Finally, a fine wire saw was used to slice through the centre of the specimen, creating two half-disks (Figure 4.51).

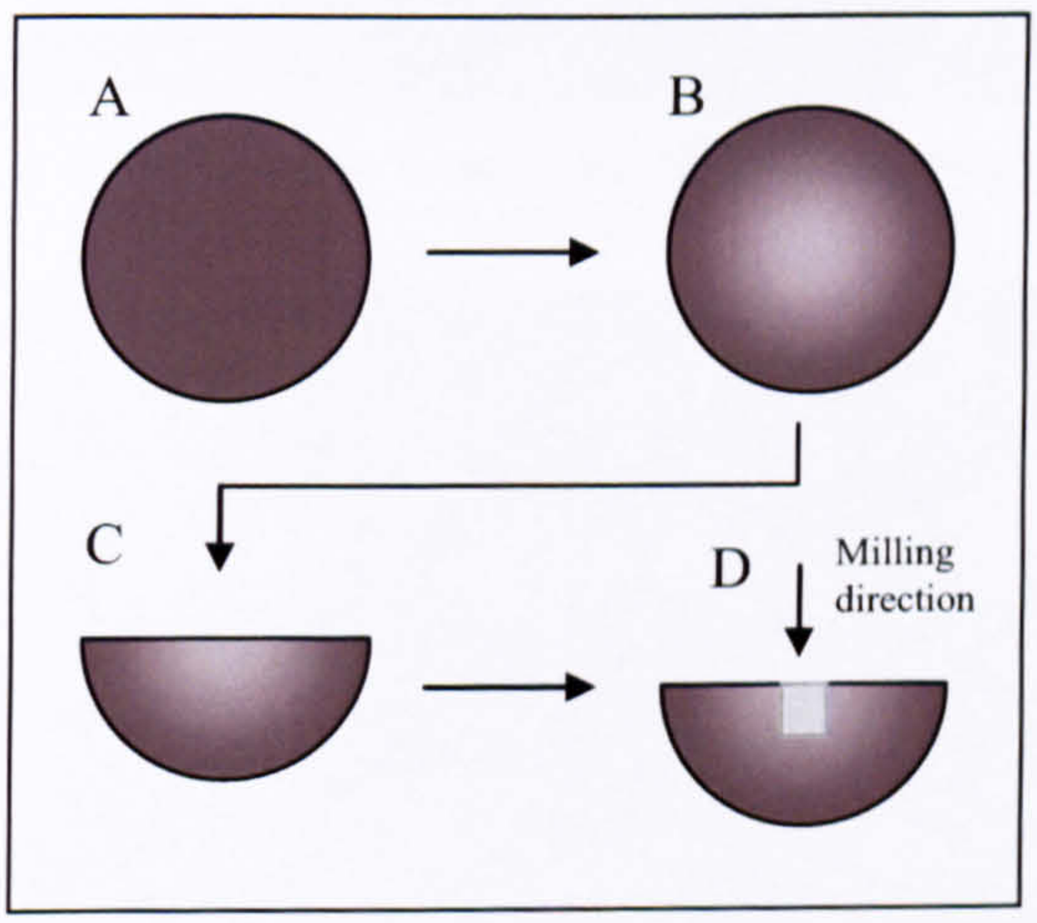


Figure 4.51 - Schematic showing FIB preparation of TEM slides. A – 3mm spark eroded disk; B – dimpling to a 50mm thickness; C – Wire cut to half-disk; D – FIB Milling and final thinning

FIB preparation was carried out on a FEI FIB 200 Workstation with a gallium beam operating at 30 keV. The specimen was mounted in a specimen holder designed to support 3 mm TEM disks. The diameter of the disks was set parallel to the direction of the incident ion beam with the flat cut edge facing upwards. The disk was tilted by 1° in order to ensure a parallel section would be prepared (see Figure 4.52).

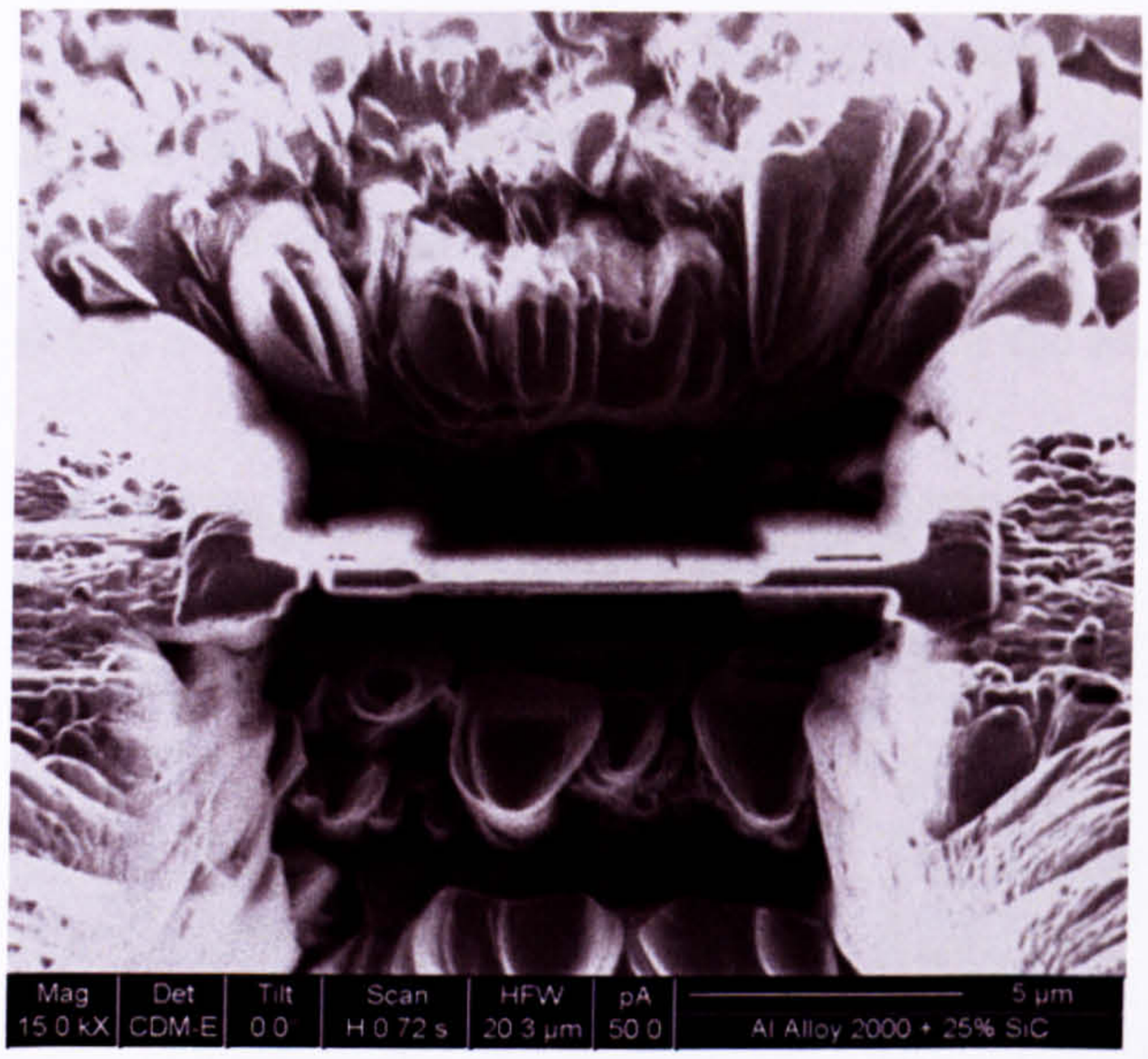


Figure 4.52 - FIB secondary electron image showing prepared thin film and surrounding material

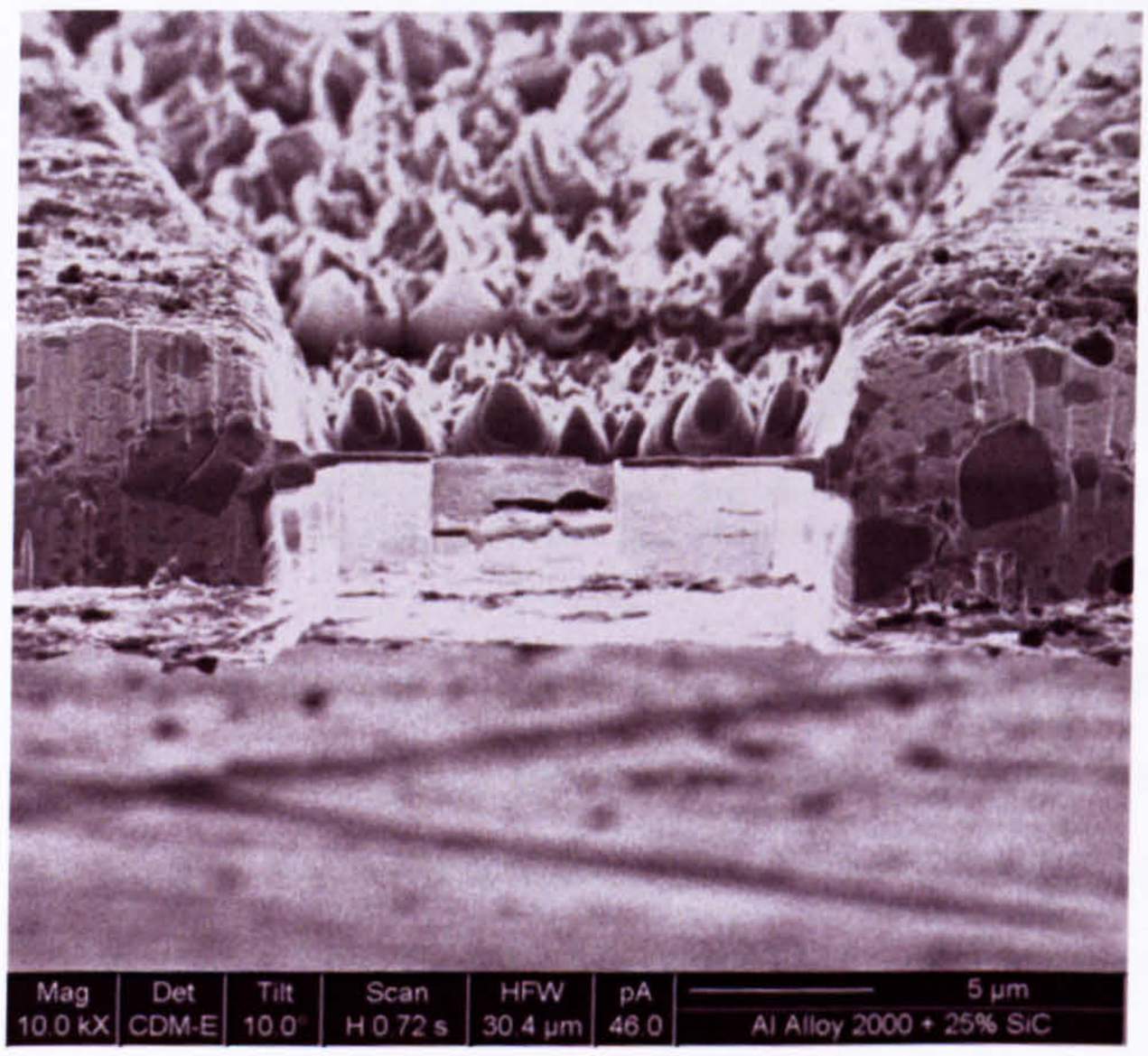


Figure 4.53 - Overhead FIB secondary electron image showing selectively thinned section and hole

Initially, it was necessary to mill the edge at 20,000 pA beam current to reduce the thickness from 50 µm to 5 µm (Figure 4.52 and Figure 4.53). Due to the higher atomic weight of Si and C, this process took up to two hours, significantly longer than the mill time for an aluminium alloy in the previous study. The thinned edge was then coated with a 2 µm thick layer of platinum in order to protect it from ion beam damage during subsequent milling and polishing operations. The layer served an additional purpose of limiting the level of gallium implantation in the specimen during polishing. The beam current was reduced to 12,000 pA and a 25 µm section was thinned from both sides to a

1 μm thickness. At 500 pA a 15 μm section was polished to a final thickness of approximately 50 nm. When approaching final thickness the foils would occasionally buckle due to residual stress relaxation within the thin section. In order to relieve the stress, a thin cut was made down one side of the section (Region "A" - Figure 4.54).

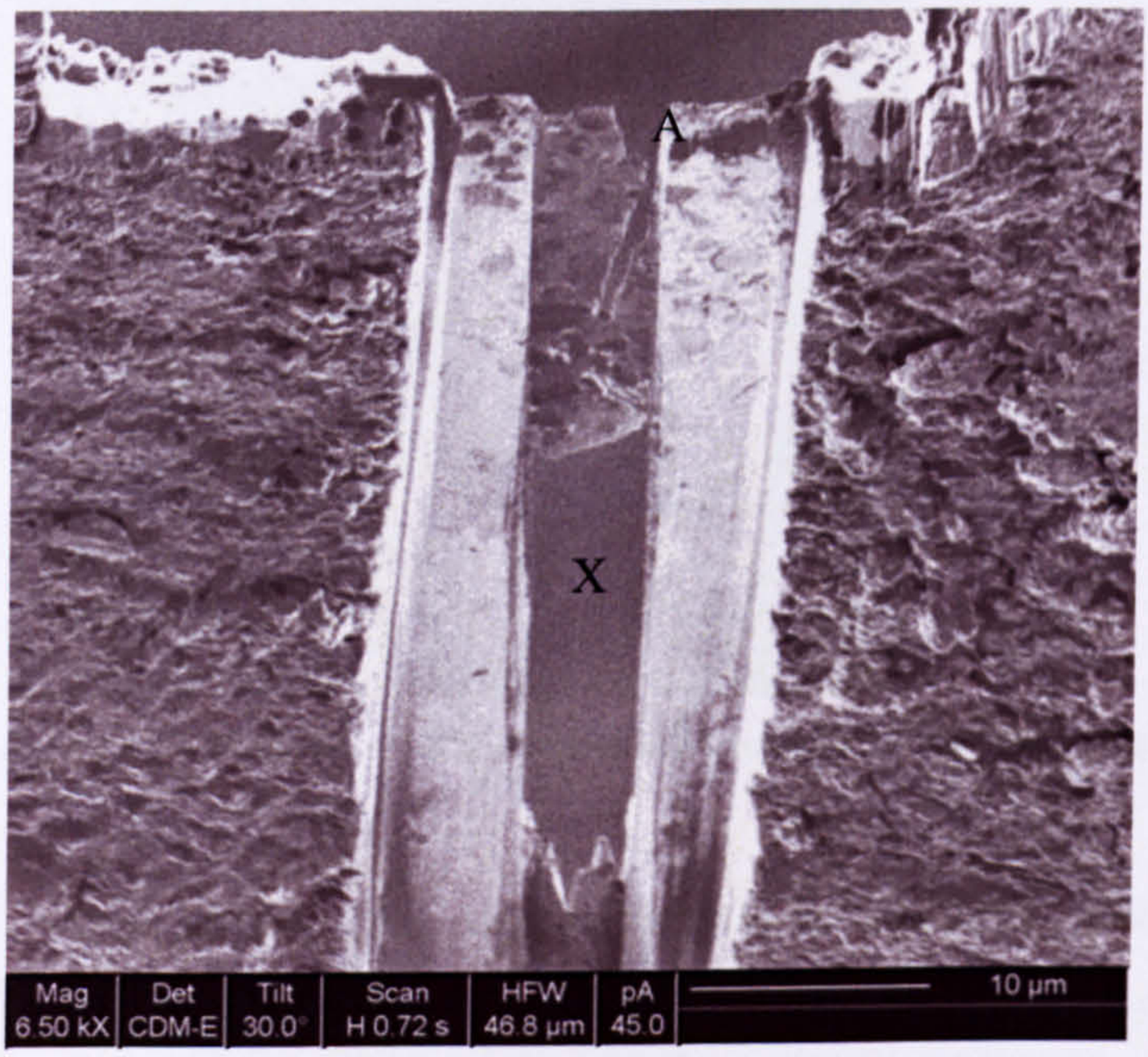


Figure 4.54 - FIB SE image of TEM foil showing damage from prior polishing operation. 'X' indicates the region where a hole has developed due to over-thinning

Following thinning, exposure to the ion beam was limited as much as possible to reduce the effect of Gallium induced damage. Milling involves the sputtering of sub-surface and surface atoms and ions by the Ga beam and prolonged exposure will lead to gallium impregnation and mechanical damage in areas where the material is relatively thin.

Transmission Electron Microscopy was carried out on a JEOL 2000FX microscope operating at 200 kV. When observed in the TEM, the first thin foil was found to contain a very high dislocation density and a mottled appearance, preventing a meaningful analysis of the microstructure. This was attributed to damage induced by cutting the thin disk with a wire saw following dimpling and prior to FIB milling and polishing. Figure 4.55 demonstrates the distorted appearance of the matrix and label "A" indicates a region containing a high density of dislocations.

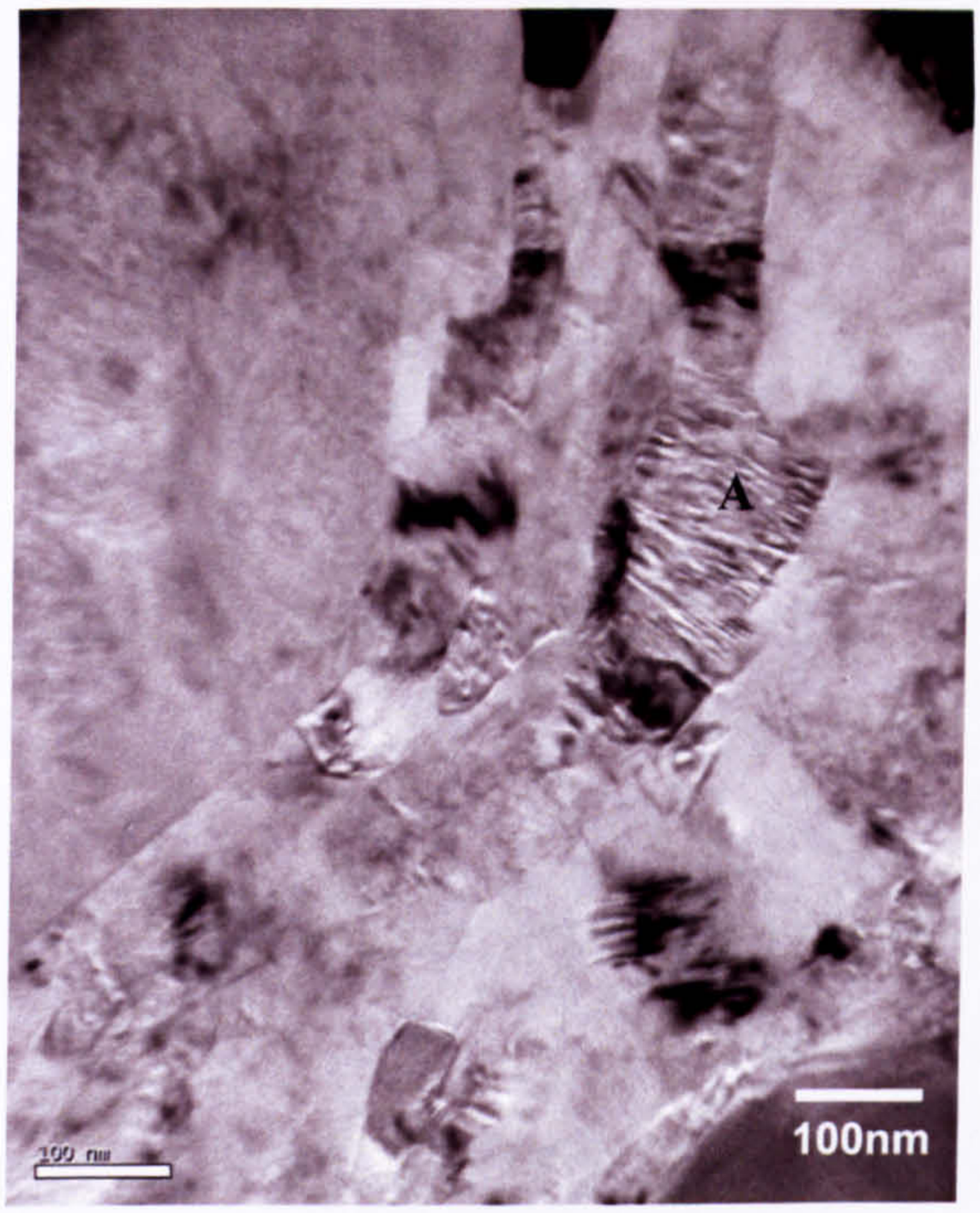


Figure 4.55 - Brightfield TEM image of FIB prepared specimen showing dislocation structure (A)

Gallium impregnation was believed to be evident at grain boundaries, as shown in the following micrograph (Figure 4.56). This supposition is also supported in the literature and proven by EDS analysis of an aluminium specimen prepared by a similar technique, as demonstrated in Figure 4.57.

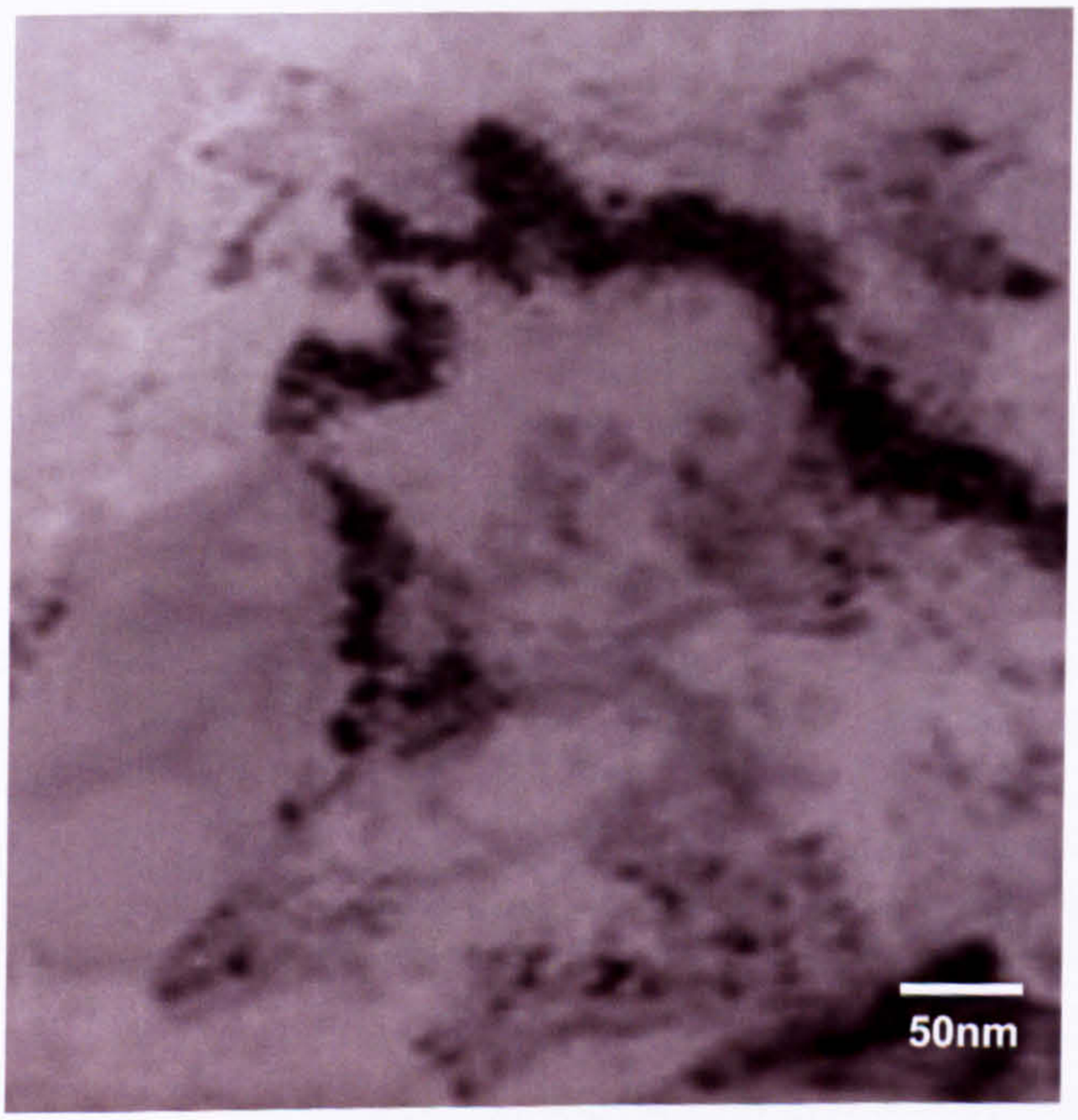


Figure 4.56 - Brightfield TEM image of FIB prepared specimen showing gallium impregnation along grain boundary

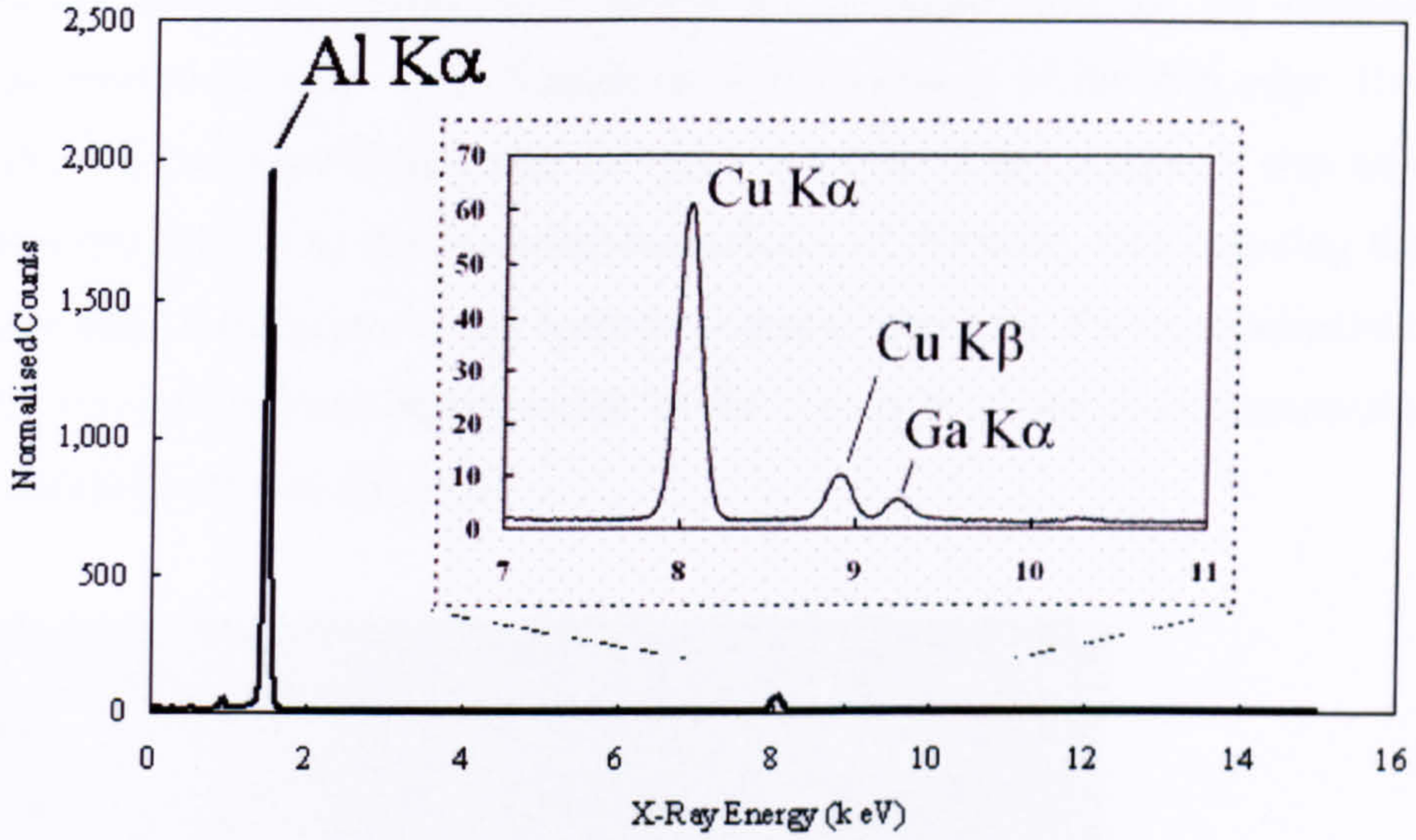


Figure 4.57 - Presence of Ga peak in EDS analysis of FIB-prepared specimen

In order to try and better preserve the thin edge and to reduce the propensity towards mechanical damage, a decision was taken to make a modification to the specimen preparation process. Rather than dimple to a 50 μm final thickness, the specimen was dimpled until a hole appeared in the centre of the disc, leaving an MMC hoop. This hoop was then cut into two halves on the wire saw and finally mounted in the FIB, as illustrated in the following schematic (Figure 4.58).

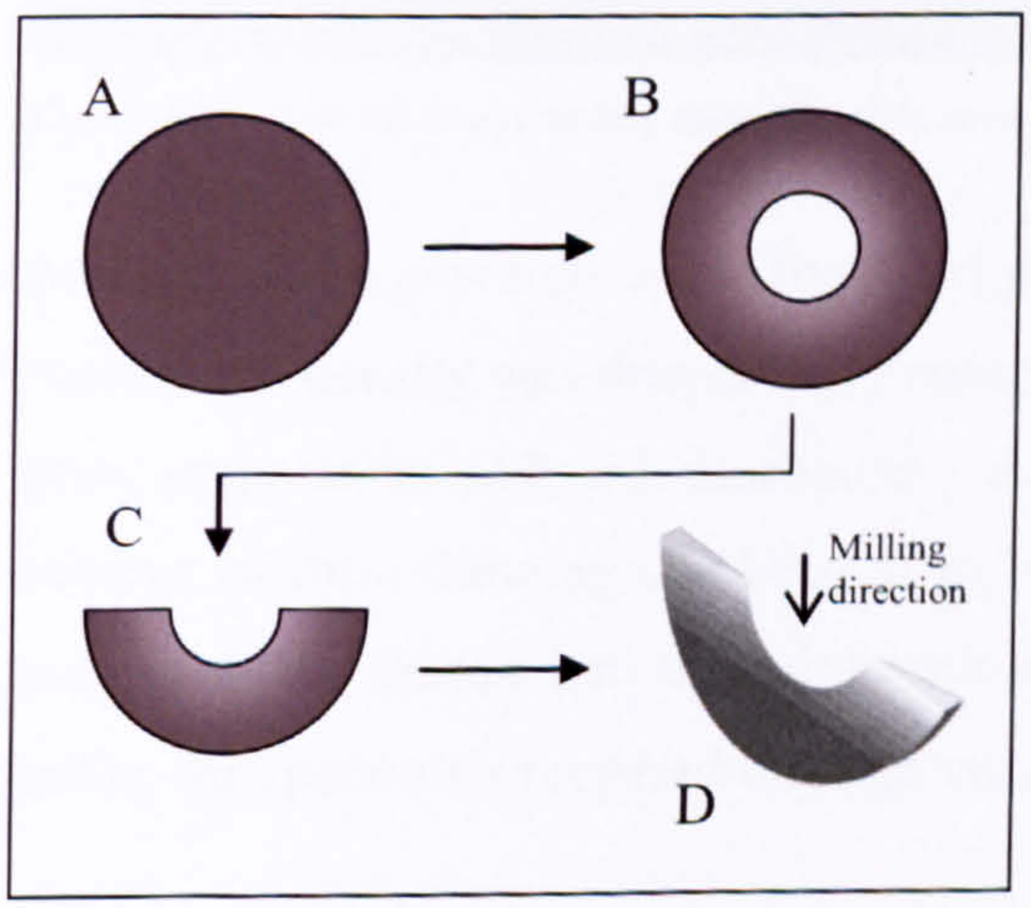


Figure 4.58 - Schematic showing modified FIB preparation of TEM slides. A – 3mm spark eroded disk; B – dimpling to a hole; C – Wire cut to crescent; D – FIB Milling and final thinning

FIB imaging showed that by dimpling to this extent, a very fine edge was preserved on the inner circumference of the hoop. This edge was approximately 5 μm thick and had

been protected from significant mechanical damage by the support of the steel stub during dimpling. Figure 4.59 shows an overhead view of the dimpled area on a specimen and offers an indication as to the integrity of the thin edge. Evidence of the wire cut can also be seen on the left hand side of the image. It was now possible to proceed directly to the final finishing stages of thinning, thus reducing the preparation time from three hours to one hour for a single specimen. This also assisted in decreasing the level of gallium impregnation in the specimen as the overall exposure time to the gallium beam was reduced.

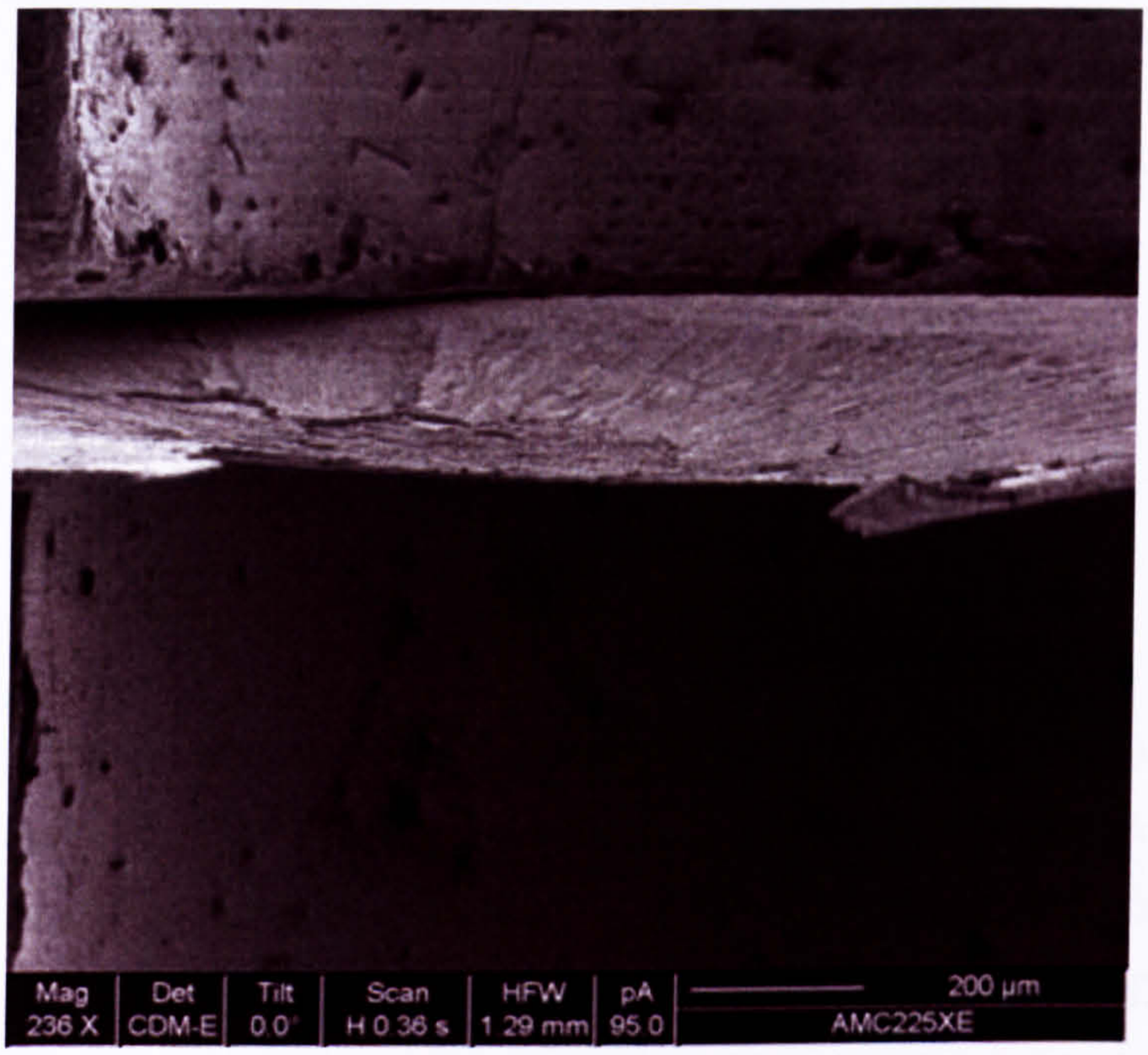


Figure 4.59 - FIB SE image at low magnification showing 'side-on' view of dimpled 3mm disc

Analysis of the new thin foil in the TEM proved that the technique had been successful. Dislocation density was dramatically reduced and the microstructure appeared to be free from preparation induced mechanical damage. The capability of the technique to achieve uniform thinning can be seen in Figure 4.60, which shows how a hole crosses over from the matrix into the reinforcement. The interfacial region is clearly defined, unlike the specimens prepared through via an electropolishing route.

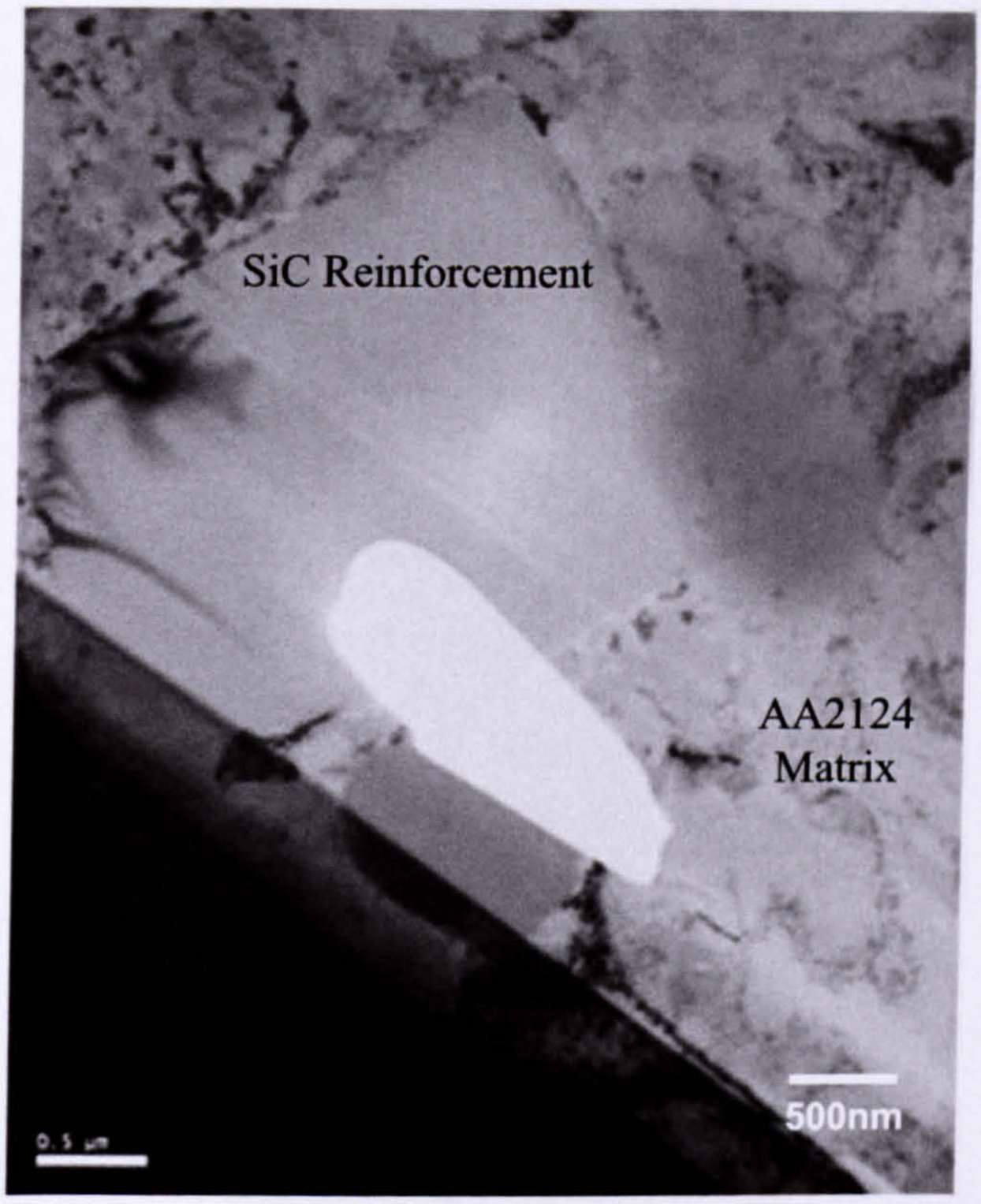


Figure 4.60 - Brightfield TEM image of hole crossing Al/SiC matrix

Although the level of mechanical damage in the specimen had been significantly reduced, there was still evidence of a degree of gallium contamination in the specimen. Previous studies have shown that gallium ion beam damage can be restricted by limiting the viewing of the specimen after polishing is complete (142). Additionally, is possible to 'clean up' the surface of the thin foil by applying a very low angle ion beam after FIB preparation. The existence of an amorphised layer could be seen when trying to analyse SADPs close the periphery of the holes. It was discovered that when the beam was moved within 100 nm of this periphery, a SADP could not be observed within the matrix region. It is believed that this is due to the amorphisation effect of the ion beam. A previous study demonstrates the presence of an amorphised layer due to the effect of the ion beam on the surface of a FIB polished section (85). This layer was found to be approximately 10 nm in depth, with the thickness depending on the atomic mass of the material. In the current study, it is believed that in the region where a SADP could not be observed, the thickness of the material was less than 20 nm. Effectively, the two amorphised layers from each side of the foil have converged and so the electron beam is randomly scattered. In regions where the foil is greater than 20 nm in thickness, the

electron beam is diffracted by the non-amorphised material at the centre of the specimen and thus a SADP is observed.

5 Conclusions

An increase in temperature for both forging and extrusion processes led to a reduction in the proof stress, ultimate tensile strength, and elastic modulus of the metal matrix composite. An increase in extrusion ratio and therefore plastic strain during deformation gave rise to a small increase in proof stress, elastic modulus and strain to failure.

Microstructural analysis by Focussed Ion Beam (FIB) microscopy provided a novel and highly effective technique for determining grain sizes and grain aspect ratios for representative regions of the microstructure. It was discovered that grain size increased with increasing processing temperature but was relatively unaffected by increasing deformation strain. The reduction in proof stress associated with increasing fabrication temperature was partially attributed to this increase in grain size, as predicted by the Hall-Petch relationship.

Although some grain elongation in the extrusion direction was evident in the material extruded at 550°C, the aspect ratio of grains indexed in samples for the other extrusion conditions showed minimal deviation from unity. This confirmed the significant role of the SiC reinforcement particles and oxide dispersoids in constraining the grain boundaries during thermomechanical deformation.

A dispersoid phase which appeared bright during FIB microscopy was identified as being Al_2MgO_4 (spinel) by SIMS analysis, which indicated the presence of magnesium and oxygen. The phase made up approximately 1 volume percent of the microstructure and calculations determined that it created a drag force sufficient to inhibit grain boundary migration by Zener pinning.

Both high angle and low angle grain boundaries were discovered in the microstructure for the material extruded at 350°C and 450°C, signifying the development of a subgrain structure during thermomechanical processing. In close proximity to the SiC particles, the majority of grain boundaries were of the high angle type, indicating a relaxation of deformation induced primary dislocation structures within these regions. For an extrusion temperature of 550°C, fewer low angle grain boundaries were observed during FIB micro texture analysis, suggesting that recovery processes were retarded at this temperature and grain coarsening was the primary grain evolution phenomenon.

A limited amount of recrystallisation was observed in the material extruded at 550°C. The recrystallised grains were not apparent at the matrix/reinforcement interfaces, as predicted in the literature by a process of particle stimulated recrystallisation, but instead could be observed in regions of relatively low reinforcement content, forming at grain boundaries. It was clear that the spinel phase was acting to inhibit the movement of the recrystallisation front, thus preventing the formation of a fully recrystallised grain structure.

Macro texture analysis by X-Ray Diffraction (XRD) revealed a weak <111> fibre texture in the material extruded at 350°C and 450°C, which was thought to contribute to the increase in proof stress for the material extruded under these conditions. This texture is the typical fibre texture in the extrusion direction for a material with a Face Centred Cubic crystal structure. The material extruded at 550°C showed no such texture and this was thought to be primarily due to the contribution of recrystallisation in generating mis-orientated grains.

It was not possible to perform electron backscatter diffraction on the MMC due to difficulties associated with preparing a flat polished surface and the shadowing effect of the SiC particles. Instead, an alternative technique for determining localised relative grain orientations in close proximity to reinforcement particles was developed using FIB microscopy. Polished specimens were tilted through 2° increments from the normal direction and the ion channelling efficiency was calculated at each angle by measuring the secondary electron yield. The variation in this value with tilt angle gave an indication as to the orientation of a specific grain. High angle grain boundaries were detected in the grains surrounding the SiC particles for all extrusion conditions and the grain orientations showed some correlation with the texture analysis carried out by XRD.

Previous studies reported that the coarsening of intermetallic phases, such as AlSiMn and Mg_2Si was a likely contributory factor to a reduction in strength of the MMC. The current study showed that this was not the case because tensile testing completed on heat treated material pre-soaked at the three extrusion temperatures gave almost identical proof stress values for all conditions. It was therefore concluded that a

thermomechanical effect controlled the microstructural evolution and subsequent mechanical properties of the MMC.

Conventional techniques for preparing thin films for Transmission Electron Microscopy were found to be unsuitable for the analysis of the matrix/reinforcement interface due to uneven thinning of the soft matrix and the hard reinforcement phases. A technique was developed for preparing site-specific electron transparent films for analysis in the TEM by FIB milling and polishing. Severe mechanical damage of specimens was avoided by dimpling a hole through the centre of a 3 mm disc. The inside edge of the hole was found to be approximately 5 μm thick and free from significant mechanical damage. This edge was thinned to a final thickness of 50 nm by FIB milling and polishing and transferred to the TEM. Uniform thinning was confirmed as both the matrix and reinforcement were found to be electron transparent. Some gallium ion deposition was evident as well as surface amorphisation, but it was possible to take selected area diffraction patterns (SADPs) from the matrix to determine grain orientation.

6 Further Work

In order to gain a better understanding of the stress dependence of strain rate, strain rate jump tests may be carried out. This would further enhance the understanding of the strain rate sensitivity of the material as well as providing information on the influence of strain rate history.

To more accurately determine the extent of dynamic recrystallisation within the MMC and substructural development and transformation, FIB preparation and microscopy could be carried out on compression samples at a range of strains, strain rates and temperatures.

Analysis of the microstructure of a failed tensile specimen in the proximity of a fracture surface would allow the determination of the exact nature of the failure mechanism, which could help to assist in designing the MMC for enhanced ductility and fracture toughness.

In order to develop the technique of grain indexing by FIB microscopy, a specimen of a monolithic aluminium alloy could be polished by conventional techniques or FIB milling and polishing. A specific region of microstructure could then be analysed by Electron Backscatter Diffraction (EBSD). Subsequently, the sample could be transferred to the FIB microscope and the same area would be analysed by using the tilt procedure and measuring grey levels to determine the ion channelling response. The EBSD data and the grey level data could then be correlated so that individual grain orientations could be determined by both techniques. This would increase overall the confidence in the FIB method and promote it as a viable alternative to EBSD for MMCs and other materials, which are difficult to analyse by the conventional method. In addition, the procedure of analysing the tilt response in two different directions could be validated.

The use of MathWorks™ or alternative computational software to automate the FIB grain indexing procedure must be considered for this approach to be widely adopted. The grey level variation of an individual grain within an image stack could be automatically monitored and compared against a database of theoretical ion channelling directions in order to rapidly determine the orientation of multiple grains in a single image. A colour spectrum technique for plotting the grain orientation data on a micrograph could also be developed.

The influence of the presence of oxide particles on preventing grain boundary migration could be further analysed by preparing a monolithic alloy with a range of oxygen contents. This would increase the understanding of the influence of both volume fraction and particle size on the pinning efficiency and confirm the accuracy of the existing models from the literature.

The process of preparing electron transparent slides for TEM analysis by FIB milling and polishing could be further refined. Firstly, a script could be written to automate the milling and polishing process allowing for unattended specimen preparation. Secondly, a final polish using a low angle / low energy ion beam could help to reduce gallium contamination and complete final thinning stages. This could be carried out on a Precision Ion Polishing System (PIPS) at incident angles of less than 1°.

High resolution interface analysis could be carried out on specimens produced in such a manner. The use of Electron Energy Loss Spectroscopy (EELS) is now widely established in TEM and provides an exciting technique to determine the exact chemical nature of the matrix/reinforcement interface in an MMC.

TEM analysis of the bright white spots identified during FIB microscopy could assist in determining their identity as Al_2MgO_4 (spinel).

7 References

1. *Critical issue in the extrusion of particle reinforced metal matrix composites.* **Davies, C. H. J.** s.l. : Trans Tech. Publications, 1995, Key Engineering Materials, Vols. 104-107, pp. 447-458.

2. *Extrudability of PM 2124/SiCp aluminium matrix composite.* **Lieblich, M., et al.** 1997, J. Mater. Sci. Lett., Vol. 16, pp. 726-728.

3. *Particle redistribution and matrix microstructure evolution during hot extrusion of cast SiCp reinforced alloy matrix composite.* **Dutta, B., Samajdar, I. and Surappa, K.** 1998, Mater. Sci. Technol., Vol. 14, pp. 36-46.

4. *Extrusion characteristics of aluminium alloy/SiCp metal matrix composites.* **Goswami, R. K., et al.** 1999, Mater Sci. Technol, Vol. 15, pp. 443-449.

5. *Superplasticity in a silicon carbide whisker reinforced aluminium alloy.* **Wu, M. Y. and Sherby, O. D.** 1984, Scripta Metall, Vol. 18, pp. 773-776.

6. **Huang, C.Y. and Daehn, G.S.** Superplastic forming of metal matrix composites by thermal and pressure cycling processes. [book auth.] A. K. Gosh and T. R. Bieler. *Superplasticity and Superplastic Forming.* Warrendale : The Minerals, Metals and Materials Society, 1995.

7. *Internal stresses superplasticity in metal matrix composites.* **Derby, B.** 1985, Scripta Metall, Vol. 19, pp. 703-707.

8. *The mechanism of thermal cycling enhanced deformation in whisker-reinforced composites.* **Daehn, G. S. and Oyama, T.** 1998, Scripta Metall, Vol. 22, pp. 1097-1102.

9. *Hot formability of an Al2009/SiCw composite sheet.* **Chan, K. C., Tong, G. Q. and Gao, L.** 1998, J Mater Process Technol, Vol. 74, pp. 142-148.

10. *Near-interface microstructure in a SiC/Al composite.* **Evans, R. D. and Boyd, J. D.** 2003, Scripta Mater, Vol. 49, pp. 59-63.

11. *Novel scheme for the preparation of transmission electron microscopy specimens with a focussed ion beam.* **Overwijk, M. H. F., van den Heuvel, F. C. and Bulle-Lieuwma, C. W. T.** 1993, Nucl. Instrum. Methods, Vol. 80/81, pp. 1324-1327.

12. **Prewett, P. D. and Mair, G. L. R.** *Focussed ion beams from liquid metal ion sources.* Taunton : Research Studies Press Ltd., 1991.

13. *Focused Ion beam XeF2 etching of materials for phaseshift masks.* **Harriott, L.R.** 6, 1993, J.Vac. Sci. Technol. B, Vol. 11, pp. 2200–2203.

14. *Applications of focussed ion beam microscopy to materials science specimens.* **Phaneuf, M. W.** 1999, Micron, Vol. 30, pp. 277-288.

15. *Microstructure and strengthening of Al-Li-Cu-Mg alloys and MMC's: II. Modelling of yield strength.* **Starink, M. J.** 14, 1998, Acta Mater., Vol. 47, pp. 3855-3868.

16. **Vedani, M.** 1994, Mat Sci Tech, Vol. 10, pp. 132-140.

17. **Nutt, S. and Carpenter, R.** 1985, Mat Sci Eng, Vol. A75, pp. 169-177.

18. **Sun, J. and Greenfield, I.** London : Elsevier Applied Science, 1987. Sixth Int Conf on Composite Materials.

19. **Dieter, G.** *Mechanical Metallurgy.* London : McGraw-Hill, 1988.

20. **Davies, C.** 1995, Scripta Metall Mater, Vol. 32, p. 309.

21. **Zhao, D., Tuler, F. and Lloyd, D.** 1994, Acta Metall Mater, Vol. 42, p. 2525.

22. **Lee, J. and Subramanian, K.** 1993, J Mater Sci, Vol. 28, pp. 1578-1584.

23. **Yu, D.** 1994, Scripta Metall Mater, Vol. 30, pp. 927-932.

24. **Jiang, Z. and Liu, Y.** 1984. 3rd International Conference on Aluminium Alloys.

25. **Han, N., Pollard, G. and Stevens, R.** 1992, Mat Sci Tech, Vol. 8, pp. 184-187.

26. **Koike, J., Mabuchi, M. and Higashi, K.** 1995, Acta Metall Mater, Vol. 43, pp. 199-206.

27. **Thomas, M. and King, J.** 1993, Mat Sci Tech, Vol. 9, pp. 742-753.

28. **Basu, A. and Humphreys, F.** Munich : s.n., 1984. 3rd Interntaional Conference on Aluminium Alloys.

29. **Starink, M. J. and Mourik, P.** 1992, Mat Sci Eng, Vol. A156, pp. 183-194.

30. **Clyne, T. W. and Withers, P. J.** An Introduction to Metal Matrix Composites. s.l. : Cambridge University Press., 1995.

31. *The effect of reinforcement shape on recrystallisation in MMC's.* **Shahani, R. A. and Clyne, T. W.** Denmark : s.n., 1991, MMC's - Processing, Microstructure and Properties.

32. *The measurement of local rotations in the electron microscope.* **Chapman, P. F. and Stobbs, W. M.** 1969, Phil. Mag., pp. 1015-1030.

33. *Influence of extrusion temperature on the microstructure and the texture of 6061Al-15vol.% SiC PM composites.* **Borrego, A.** 2002, Comp. Sci. Tech., Vol. 62, pp. 731-742.

34. **Ltd., AMC.** AMC225xe Datasheet. *AMC.* [Online] 2007. [Cited: 17 01 2007.] http://amc-mmc.com/225xe_data.htm.

35. **Zheng, W., Baoliang, Z. and Yanwen, Y.** 1994, Scripta Metall Mater, Vol. 30, pp. 1367-1372.

36. **Hee, Y.K. and Soon, H. H.** 1994, Scripta Metall Mater, Vol. 30, pp. 297-302.

37. **Jing, B.** Munich : s.n., 1984. 3rd International Conference on Aluminium Alloys.

38. **Badini, C., Marino, F. and Verne, E.** 1995, Mat Sci Eng, Vol. A191, pp. 185-191.

39. *Numerical prediction of the development of particle stress in the forging of aluminium metal matrix composites.* **Roberts, S. M., et al.** 1996, J. Mater. Process. Technol., Vol. 60, pp. 711-718.

40. *The influence of temperature on microstructural damage during uniaxial compression of aluminium matrix composites.* **Barnes, S. J., et al.** 1995, Scripta Metall. Mater, Vol. 33, pp. 323-329.

41. **Arsenault, R. and Zhou, X.** 1993, Scripta Metall Mater, Vol. 28, pp. 875-878.

42. **Vogelsang, M., Arsenault, R. and Fisher, R.** 1987, Met Trans, Vol. A17, pp. 379-389.

43. **Shibata, M. and Taya, T.** 1992, Acta Metall Mater, Vol. 40, pp. 3141-4148.

44. **Sun, Z.** 1992, Acta Metall Mater, Vol. 40, pp. 2961-2966.

45. **Taya, M. and Mori, T.** 1987, Acta Metall Mater, Vol. 35, pp. 155-162.

46. **Taya, M, Lulay, K and Lloyd, D.** 1991, Acta Metall Mater, Vol. 39, pp. 73-87.

47. **Hong, S. and Gray, G.** 1992, Acta Metall Mater, Vol. 40, pp. 3299-3315.

48. **Srivatsan, T., Lanning, D. and Soni, K.** 1993, J Mater Sci, Vol. 28, pp. 3205-3213.

49. **Thomas, M. and King, J.** 1994, Scripta Metall Mater, Vol. 31, pp. 209-214.

50. **Papazian, J.** 1988, Met Trans, Vol. A19, pp. 2945-2593.

51. **Tatsuo, S. and Takahasi, T.** 1983, Trans Jap Inst Met, Vol. 24, pp. 386-395.

52. **Gupta, A., Gaunt, P. and Chaturvedi, M.** 1987, Philosophical Magazine, pp. 375-387.

53. **Dyos, K.** Department of Materials, Imperial College of Science, Technology and Medicine. London : s.n., 1996. p. 42, PhD Thesis.

54. **Silcock, J.** 1960, J Inst Met, Vol. 89, pp. 203-210.

55. **Dutta, I. and Haper, C.** Munich : s.n., 1984. 3rd International Conference on Aluminium Alloys.

56. **Ryum, N.** Engineering materials advisory service, pp. 1511-1545.

57. **Hadianfard, M., Yiu-Wing, M. and Healy, J.** 1993, J Mater Sc, Vol. 28, pp. 3665-3669.

58. **Ning, X.** 1993, J Mater Sci Lett, Vol. 12, pp. 1644-1647.

59. **Vermaut, P. and Ruterana, P.** 1995, J Micr, Vol. 177, pp. 387-398.

60. **Styles, C.** Munich : s.n., 1984. 3rd international conference on aluminium alloys.

61. **Schmidt, U., Unger, R. and Gerloff, R.** 1995, J Mater Sci, Vol. 30, pp. 3265-3273.

62. **Youdelis, W. and Fang, W.** 1994, J Mater Sci, Vol. 30, pp. 2269-2276.

63. **Dutta, I., Harper, C. and Dutta, G.** 1994, Met Mat Trans, Vol. A25, pp. 1591-1602.

64. **Kuo-Chan, C. and Cheun-Guang, C.** 1995, Met Mat Trans, Vol. A26, pp. 1035-1043.

65. **Friend, C. and Luxton, S.** 1988, J Mater Sc, pp. 3173-3180.

66. **Friend, C.** pp. 309-315.

67. **Hunt, E., Pitcher, P and Gregson, P.** Amsterdam : s.n., 1990. Proc Int Conf Advanced Al and Mg alloys.

68. **Bhanu Prasad, V.** J Mater Sci.

69. **Shakeshaff, A.** 1995, J Mater Sci, Vol. 30, pp. 2269-2276.

70. **Zhang, D. and Cantor, B.** 1991. 2nd European Conference on advanced materials and processes.

71. **Abis, S. and Donizelli, G.** 1998, J Mater Sci Lett, Vol. 7, pp. 51-52.

72. **Karov, J. and Youdelis, W.** 1986, Mat Sci Tech, Vol. 2, pp. 1138-1188.

73. **Fujii, T.** Department of Materials, Imperial College of Science, Technology and Medicine. London : s.n., 2003. PhD Thesis.

74. *3D reconstruction and characterization of polycrystalline microstructures using a FIB–SEM system.* **Groeber, M. A., et al.** 2006, Materials Characterization, Vol. 57, pp. 259–273.

75. **Williams, D. B. and Carter, C. B.** *Transmission Electron Microscopy: Basics.* New York : Plenum Press, 1996. Vol. 1.

76. *A review of focused ion beam milling techniques for TEM specimen preparation.* **Giannuzzi, L. A. and Stevie, F. A.** 1999, Micron , Vol. 30, pp. 197–204.

77. *Cross-sectopnal transmission electron microscopy of precisely selected regions from semiconductor devices.* **Kirk, E. C. G., Williams, D. A. and Ahmed, H.** 1989, Inst. Phy. Ser., Vol. 100, pp. 501-506.

78. *Cross-sectional TEM specimen preparation of semiconductor devices by focussed ion beam etching.* **Mark, K.** [ed.] R. Anderson. Pittsburgh : MRS, 1990. Materials Research Society Symposium Proceedings. Vol. 199, pp. 271-280.

79. *Fabrication of planar and cross-sectional TEM specimens using a focussed ion beam.* **Young, R. J., et al.** [ed.] R. Anderson. Pittsburgh : MRS, 1990. Materials Research Society Symposium Proceedings. Vol. 199, pp. 205-216.

80. *FIBX-TEM-Focussed ion beam milling for TEM sample preparation.* **Basile, D. P., et al.** [ed.] R. Anderson, R. Tracy and B. Bravman. Pittsburgh : MRS, 1992. Materials Research Society Symposium Proceedings. Vol. 254, pp. 23-41.

81. **Gianuzzi, L. A., et al.** 1998.

82. *TEM observation of micrometer-sized Ni powder particles thinned by FIB cutting technique.* **Kitano, Y., et al.** 1995, J. Electron Microsc., Vol. 44, pp. 410-413.

83. *FIB/HVEM observation of the configuration of cracks and the defect structure near the cracks.* **Saka, H. and Abe, S.** 1997, Jap. Soc. Electron Microsc, Vol. 1, pp. 45-57.

84. **McPhee, W. A. G., et al.** *A Transmission Electron Microcope Sample Preparation Technique for Sintered Alloys.* University of Queensland. 2004. Unpublished Work.

85. *Surface damage formation during ion-beam thinning of samples for transmission electron microscopy.* **McCaffrey, J. P., Phaneuf, M. W. and Madsen, L. D.** 2001, Ultramicroscopy, Vol. 87, pp. 97–104.

86. **Albarede, P. H. and Lezec, H. J.** Transmission electron microscopy of focused ion beam induced damage at 50 keV in Si. [ed.] H. A. Calderon Benavides and M. J. Yacaman. *Electron Microscopy.* 1998.

87. **Schuhrke, T., et al.** 1992, Ultramicroscopy, Vol. 41, p. 429.

88. **Dingley, D. J. and Randle, V.** 1992, Journal of Materials Science, Vol. 27, p. 4545.

89. *TEM investigation of FIB induced damages in preparation of metal material TEM specimens by FIB.* **Jinshan, Y., et al.** 2006, Materials Letters, Vol. 60, pp. 206-209.

90. **Barna, A., Pecz, B. and Menyhard, M.** 1998, Ultramicroscopy, Vol. 70, p. 161.

91. *Specific Site Cross-Sectional Sample Preparation using Focussed Ion Beam for Transmission Electron Microscopy.* **Schraub, D. M. and Rai, R. S.** 1-2, 1998, Prog. Crystal Growth and Charact., Vol. 36, pp. 99-122.

92. **International, ASTM.** *Standard Test Methods for Determining Average Grain Size, Designation: E 112 – 96.* 2006. Standard.

93. **Rasband, Wayne.** ImageJ Homepgae. *ImageJ.* [Online] National Institue of Health. http://rsb.info.nih.gov/ij/index.html.

94. **Silk, J. R.** *The Elevated Temperature Mechanical Properties of an Aluminium MMC.* 2001. AMC Ltd. Internal Report.

95. —. *Mechanical Properties and Microstructure of a High Temperature Aluminium Alloy.* s.l. : Unpublished Work, 2002. AMC Ltd. Internal Report.

96. **Haidary, J. T., Petch, N. J. and Rios, E. R. d. L.** 1983, Philos. Mag., Vol. 47, p. 870.

97. **Hull, D. and Bacon, D. J.** *Introduction to Dislocations.* 4th Edition. s.l. : Butterworth-Heinemann, 2001.

98. **Forrest, P. G.** *Fatigue of Metals.* London : Pergamon Press, 1962.

99. **Johnston, W. G. and Stein, D. F.** 1963, Acta. Metall., Vol. 11, pp. 317-318.

100. *Effect of strain rate on tensile ductility for a series of dispersion-strengthened aluminium-based alloys.* **Skinner, D. J., Zedalis, M. S. and Gilman, P. S. A,** 1989, Mater. Sci. Eng., Vol. 119, pp. 81-86.

101. **Lubahn, J. D. and Felgar, R. P.** 1961, Plasticity and creep of metals, p. 411.

102. **Mitra, S.** 1996, Metal. And Met. Trans., Vol. A 27A, p. 3913.

103. *Precipitation and dissolution kinetics in Al–Cu–Mg–Fe–Ni alloy 2618 and Al–alumina particle metal matrix composite.* **Oguocha, I. N. A. and Yannacopoulos, S.** 1997, Mater Sci Eng, Vol. A, p. 231.

104. *Dislocation generation due to Differences between Coefficients of Thermal Expansion.* **Arsenault, R. J. and Shi, N.** 1986, Mat. Sci. & Eng., Vol. 81, pp. 175-187.

105. *Deformation and Annealing Mechanisms in Discontinuously Reinforced Metal Matrix Composites.* **Humphreys, F. J.** [ed.] S. I. Andersen, H. Lilholt and O. B. Ped. Roskilde : s.n., 1988. Mechanical and Physical Behaviour of Metallic and Ceramic Composites, 9th Ris Int. Symp.

106. **Miller, W. S. and Humphreys, F. J.** Strengthening Mechanisms in Metal Matrix Composites. [book auth.] P. K. Liaw and M. N. Gungor. *Fundamental Relationships Between Microstructure and Mechanical Properties of Metal-Matrix Composites.* Warrendale : TMS, 1990, pp. 517-541.

107. **McQueen, H. J. and Jonas, J. J.** [ed.] R. J. Arsenault. New York : Academic Press, 1975. Treatise on materials science. Vol. 6, p. 393.

108. *Aspects of Particle Fracture in Particulate Reinforced MMCs.* **Lloyd, D.** 1991, Acta Met. Et Mat., Vol. 39, pp. 59-72.

109. **Frost, H. J. and Ashby, M. F.** *Deformation mechanism maps, the plasticity and creep of metals and ceramics.* London : Pergamon Press, 1982.

110. **Raj, R. A.** 1981, Metall Trans A, Vol. 12, p. 1089.

111. *Recrystallisation Microstructure in Cold-Rolled Aluminium Composites Reinforced by Silicon Carbide Whiskers.* **Liu, Y. L., Hansen, N. and Jensen, D. J.** 1989, Metall. Trans., Vol. 20A, pp. 1743-1753.

112. *Recrstallization Mechanisms in Two-Phase Alloys.* **Humphreys, F. J.** 1979, Metal Sci, Vol. 13, pp. 136-145.

113. *Recristallisation Acceleree at Retardee dans les Produits Renforces par des Dispersions.* **Hansen, N.** 1975, Mem. Sci. Rev. Metall., Vol. 72, pp. 189-203.

114. *Effect of consolidation temperature on mechanical properties of rapidly solidified Al-7Mg-1Zr alloy.* **Dashwood, R. J. and Sheppard, T.** 1993, Mat. Sci. & Tech., Vol. 9, p. 683.

115. *Microstructural Development During Thermomechanical Processing of Particulate Metal Matrix Composites.* **Humphreys, F. J., Miller, W. S. and Djazeb, M. R.** 1990, Mater. Sci. Tech, Vol. 6, pp. 1157-1166.

116. **Shahani, R. A.** *Microstructural Development During Thermomechanical Processing of Aluminium-Based Composites.* Univ. Of Cambridge. 1991. PhD Thesis.

117. *Near-interface microstructure in a SiC/Al composite.* **Evans, R.D. and Boyd, J. D.** 2003, Scripta Mater., Vol. 49, pp. 59-63.

118. **Lloyd, D.J. and Jin, I.** Metal Matrix Composites. *Comprehensive Composite Materials Vol. 3.* Amsterdam : Elsevier, 2000, pp. 1-21.

119. **Lloyd, D. J.** 1994, Int. Mater. Rev., Vol. 39, pp. 1-23.

120. **Prader, P. and Degisher, P.** Paris : s.n., 1999. Proceeding of the 12th Internat. Conf. On Composite Materials.

121. *Kinetics of the Growth of Spinel, MgAl2O4, on Alumina Particulate in Aluminium Alloys Containing Magnesium.* **McLeod, A.D. and Gabryel, C.M.** 1992, Metallur. Trans. A, Vol. 23A, pp. 1279-1283.

122. *Squeeze casting silicon carbide particulate reinforced magnesium matrix composite.* **Lo, J., et al.** [ed.] Hui. 1996. Proceedings of the Third Interntational Conference on Composite Engineering. pp. 533-542.

123. **Chater, R. J.** *Analysis of bright spots in FIB SEI for Al-B4C MMC.* s.l. : Unpublished Work, 2007. Unpublished Work.

124. —. *SIMS analysis of white spot regions for oxygen.* s.l. : Unpublished Work, 2007.

125. *Current issues in recrystallization: a review.* **Doherty, R. D.** 1997, Materials Science and Engineering, Vol. A238, pp. 219-274.

126. *Misorientation effects on discontinuous precipitation in Al-Ag-Ca.* **Hirth, S and Gottstein, G.** 1998, Acta Materialia, Vol. 46, pp. 3975-3984.

127. **Lin, J. P., Lei, C. T. and An, X. Y.** 1992, Scripta Metall Mater, Vol. 26, p. 1869.

128. **Humphreys, F. J. and Hatherly, M.** *Recrystallization and related annealing phenomena.* s.l. : Elsevier Science Ltd., 1995.

129. *Current issues in recrystallization: a review.* **Doherty, R. D., et al.** 1997, Mater Sci Eng A, Vol. 238, pp. 219–274.

130. *Rolling textures in f.c.c. and b.c.c. metals.* **Dillamore, I. L. and Roberts, W. T.** 1964, Acta Metallurgica, Vol. 12, pp. 281-293.

131. *Hot Extrusion of Al-SiC. Texture and Microstructure, in Metal Matrix Composites – Processing, Microstructure and Properties.* **Jensen, D. J., Liu, Y. L. and Hansen, N.** Roskilde : s.n., 1991. 12th Ris. Int. Symp. pp. 417-422.

132. **Wassermann, G. and Grewen, J.** *Texturen metallischer Werkstoffe.* Berlin : Springer-Verlg, 1962.

133. *Contrast mechanisms in focused ion beam imaging.* **Olson, T. K., Lee, R. G. and Morgan, J. C.** 1992. Proc ISTFA. Vol. 92, pp. 373-382.

134. *Objective comparison of scanning ion and scanning electron microscope images.* **Ishitani, T. and Tsuboi, H.** 1996, Scanning, Vol. 19, pp. 489–497.

135. *Ion channeling effects in scanning ion microscopy with a 60 keV Ga + probe.* **Levi-Setti, R., Fox, T. and Lam, K.** Nucl. Instrum. Methods : s.n., 1983, Vol. 205, pp. 299–309.

136. **Franklin, R. E., et al.** 1988, J. Mater. Sci. Lett., Vol. 7, p. 39.

137. **Kola, R. R., Celler, G. K. and Harriott, L. R.** 1993. Mater. Res. Soc. Symp. Proc. Vol. 279, p. 693 .

138. **Lindhard, J.** 1966, Phys. Lett., Vol. 8, p. 189.

139. **Onderdelinden, D.** 1966, Appl. Phys. Lett., Vol. 8, p. 189.

140. **Palmer, W., et al.** 1990, Nucl. Instrum. Methods Phys. Res. B, Vol. 51, p. 34.

141. *Cross-sectional TEM specimen preparation of semiconductor devices by focused ion beam etching.* **Park, K.** [ed.] R. Anderson. Pittsburgh : MRS, 1990. Materials Research Society Symposium Proceedings. pp. 271-280.

142. *TEM investigation of FIB induced damages in preparation of metal material TEM specimens by FIB.* **Yu, J., et al.** 2006, Materials Letters, Vol. 60, pp. 206-209.

143. *Semi-solid forming of commercial SiCp reinforced aluminium alloy powder.* **Fuji, T., Dashwood, R. J. and McShane, H. B.** 2002, Semi-solid processing of alloys and composites.

144. **Thomas, M. and King, J.** J Mater Sci, Vol. 29, pp. 5272-5278.

145. *High resolution structure imaging of octahedral void defects in as-grown Czochralski silicon.* **Bender, H., Vanhellemont, J. and Schmolke, R.** 1997, Japanese Journal of Applied Physics, Vol. Part 2: Letters 36, pp. 1217-1220.

146. *Application of the focused-ionbeam technique for prepared the cross-sectional sample of chemical vapor deposition diamond thin film for high-resolution transmission*

electron microscope observation. **Tarutani, M., Takai, Y. and Shimizu, R.** 1992, Japanese Journal of Applied Physics, Vol. Part 2 31, p. 1305.

147. *Investigation of thin-film transistors using a combination of focused ion beam etching and cross-sectional transmission electron microscopy observation, Thin Solid Films.* **Tsuji, S., et al.** Yokohama : s.n., 1996. Proceedings of the 1995 13th International Vacuum Congress and the 9th International Conference on Solid Surfaces. Vols. 281–282(1-2), pp. 562–567.

148. *Applications of focused ion beam microscopy to materials science specimens.* **Phaneuf, M. W.** 1999 : Pergamon, Micron, Vol. 30, pp. 277-288.